UNIVERSITY OF LEEDS

Linear Spectropolarimetry Of Herbig Ae/Be Stars.

Karim Mahmood Ababakr

School of Physics and Astronomy

University of Leeds

Submitted in accordance with
the requirements for the degree of

Doctor of Philosophy

July 2016

The candidate confirms that the work submitted is his own, except where work which has formed part of jointly authored publications has been included. The contribution of the candidate and the other authors of this work has been explicitly indicated. The candidate confirms that appropriate credit has been given within this thesis where reference has been made to the work of others.

Preface

Within this thesis, some of the chapters contain work presented in the following jointly authored publications:

I. "Linear spectropolarimetry across the optical spectrum of Herbig Ae/Be stars" – **K. M. Ababakr**, R. D. Oudmaijer and J.S. Vink, 2016, MNRAS, 461, 3089.

II. "Spectroscopy and linear spectropolarimetry of the early Herbig Be stars PDS 27 and PDS 37" – **K. M. Ababakr**, J. R. Fairlamb, R. D. Oudmaijer, M. E. van den Ancker, 2015, MNRAS, 452, 2566.

Paper I forms the basis of Chapter 2. The paper details the FORS2 spectropolarimetric observations of 12 HAeBe objects. The work was carried out by the primary author, K. M. Ababakr, and text was also written by the primary author. The co-authors provided comments on various drafts of the paper which were incorporated in the final paper.

Paper II forms the basis of Chapter 3. The paper presents an in-depth study of two particularly interesting HAeBe objects PDS 27

and PDS 37. The spectropolarimetric work presented in these sections of the paper were performed and written by the primary author, K. M. Ababakr. The work on presenting spectroscopic data and obtaining the stellar parameters presented in these sections of the paper were jointly performed and written between the primary author, K. M. Ababakr and the secondary author, J. R. Fairlamb. Other sections of the paper were the sole work of the secondary author, J. R. Fairlamb; as such, with the exception of section 3.4.1.4, these particular sections are not included in this thesis. R. D. Oudmaijer and M. E. van den Ancker obtained the spectroscopic data. R. D. Oudmaijer also provided comments on various drafts of the paper which were incorporated in the final paper.

Acknowledgements

I would like to begin by thanking my supervisor René Oudmaijer, not only for his excellent supervision and guidance but also for continuously encouraging and motivating me throughout my PhD. It has been a great privilege to work with you and I sincerely appreciate all your guidance and support. I would also like to thank Jorick Vink and Willem-Jan de Wit for the many useful discussions and valuable feedback. I am eternally grateful to Ignacio Mendigutia and John Fairlamb for sharing their knowledge and helping me immensely in my study. I would also like to thank the academic staff at the University of Leeds for being friendly and helpful.

A warm thank you goes to Fernando Olguin, Jacob Close and Harrison Steggles for being great office mates and for all your assistance. I would like to thank all my fellow PhD students and the postdoc researchers. Special thanks go to Nichol Cunningham, John Ilee, Katharine Johnston and Luke Maud for making my time enjoyable in Leeds and teaching me British slang.

Last but not least I must thank my parents and my brothers and sisters. I would not be where I am today without your endless encouragement and unconditional support.

Abstract

This thesis presents the results of FORS2 and ISIS spectropolarimetric observations of a total of 28 Herbig Ae/Be stars. The results on the X-shooter spectroscopic observations and PIONIER interferometric observations of two early Herbig Be stars PDS 27 and PDS 37 are also presented. The FORS2 medium resolution spectra cover the entire optical range, and comprise the largest spectropolarimetric wavelength coverage, 4560 Å to 9480 Å, published to date. In this range, the spectra of the targets show numerous spectral lines predominantly in emission including hydrogen recombination lines, Ca II, He I, Fe II, O I and a number of forbidden lines. A change in linear polarisation across the Hα line is detected in most objects. Such a line effect reveals the fact that stellar photons are scattered off free electrons that are not distributed in a spherically symmetric volume, suggesting the presence of small disks around these accreting objects. Thanks to the large wavelength coverage of the FORS2 data, it can be reported that Hα is the spectral line in the optical wavelength range that is most sensitive to revealing deviations from spherical symmetry, and the one most likely to show a line effect across the polarisation in such cases. Few other spectral lines display changes in polarisation across the line. In addition, Hα is the only line which shows an ef-

fect across its absorption component in some sources. A scenario is presented to explain this finding and demonstrate that the detection of the line effect strongly relies on the number of photons scattered into our line of sight. The analysis of spectral lines and photometry shows that PDS 27 and PDS 37 are hot, massive and young in their evolution and may become O-type stars. In addition, these two objects have very active circumstellar environment evidenced by a strong wind, strong polarisation and IR excess. The near infrared interferometric results confirm the spectropolarimetric results of the presence of a circumstellar disk around these two objects and also suggest that the objects have a possible companion. The first spectropolarimetry of Herbig Ae/Be stars across He I line at 1.083 μm is also presented to trace the inner accretion regions of the disk. Due to the fact that the resolution was not sufficient, the data did not show a strong indication of the line effect. Finally, the first statistical spectropolarimetric investigations of a sample of 56 Herbig Ae/Be stars are provided. The results show that the detection rate of the line effect is very high (75 %), implying that most of Herbig Ae/Be stars possess a disk. The statistical results might suggest that Herbig Ae stars form in the same manner as T Tauri stars via magnetospheric accretion while Herbig Be stars could have a different accretion mechanism.

Abbreviations

AMBER	Astronomical Multi-Beam Combiner
BL	Boundary Layer
CTTs	Classical T Tauri stars
DIBs	Diffuse Interstellar Bands
ESO	European Southern Observatory
EW	Equivalent Width
FORS2	FOcal Reducer/low dispersion Spectrograph 2
FWHM	Full Width at Half Maximum
FWZI	Width at Zero Intensity
GMC	Giant Molecular Cloud
HAe	Herbig Ae
HAeBe	Herbig Ae/Be
HBe	Herbig Be
HR	Hertzsprung-Russell
IMF	Initial Mass Function
IR	Infrared
IRAF	Image Reduction and Analysis Facility
ISIS	Intermediate dispersion Spectrograph and Imaging System
ISM	Interstellar Medium
KH	Kelvin-Helmholtz
MA	Magnetospheric Accretion

MYSO	Massive Young Stellar Object
NICS	Near Infrared Camera Spectrometer
NIR	Near Infrared
OPTICON	The Optical Infrared Co-ordination Network
PA	Position Angle
PDS	Pico dos Dias Survey
PIONIER	Precision Integrated-Optics Near-infrared Imaging ExpeRiment
PMS	Pre-Main Sequence
RMS	Red MSX Source
SED	Spectral Energy Distribution
SNR	Signal-to-Noise Ratio
TNG	Telescopio Nazionale Galileo
TSP	Time Series/Polarimetry Package
UT	Unit Telescope
UVB	Ultra-Violet and Blue
UV	Ultra-Violet
VIS	Visible
$V_{\rm LSR}$	Local Standard of Rest Velocity
VLT	Very Large Telescope
VLTI	Very Large Telescope Interferometer
WHT	William Herschel Telescope
YSO	Young Stellar Object
ZAMS	Zero Age Main Sequence

Contents

List of Figures

LIST OF FIGURES

LIST OF FIGURES

List of Tables

LIST OF TABLES

Chapter 1

Introduction

The formation of massive stars, whose masses are >8M$\odot$, is considered as one of the most outstanding questions in astrophysics. These objects play a key role in the chemical evolution of galaxies. They inject the interstellar medium with heavy elements and powerful radiation through winds and supernova explosions, ionise surrounding material and trigger further star formation (Zinnecker & Yorke 2007). Despite their importance, the formation of massive stars is still less well understood than that of lower mass stars, which is widely accepted to be formed via magnetically controlled accretion (Muzerolle *et al.* 1998; Bertout 1989). Massive stars have radiative envelopes and thus they are likely to be non- magnetic. Therefore, the formation mechanism is expected to be different than low mass stars which have convective envelopes. Observationally, the study of the formation of massive stars is challenging as they reside faraway and are deeply embedded in their natal clouds. The optically bright, intermediate mass (2-10$M_{\odot}$) pre-main sequence Herbig Ae/Be (HAeBe) stars can help in this respect as they bridge the gap between the low mass T Tauri stars and massive stars.

It is believed that the forming mechanism switches from magnetically controlled accretion through the disk to the as yet unknown mechanism in the mass range occupied by HAeBe stars. The aim of this chapter is to provide an overview of our current understanding of star formation and its challenges. In particular, I will focus on the areas that are closely related to this thesis. I will start with discussing the environment where the star formation takes place in Section 1.1. In Section 1.2 I present the classical formation mechanism of low mass stars. An overview of massive star formation is presented in Section 1.3. A summary of HAeBe stars is provided in Section 1.4. Section 1.4 presents the main observational technique used in this thesis. Finally, the thesis is briefly introduced in Section 1.5.

1.1 Sites of Star Formation

The coldest, 10-20 K, and densest regions of the interstellar medium, where the gas is in the form of mostly molecular hydrogen H_2, are thought to be the ideal sites for forming stars (Bergin & Tafalla 2007). Fig. 1.1 shows a star forming region in the constellation Aquila, hundreds of new stars are expected to be formed across the region. The two bright regions in the figure are where the clouds are illuminated by newly born stars. The largest molecular clouds are giant molecular clouds (GMCs) which have masses in the range between 10^4 $M_\odot$ to 10^5 $M_\odot$, sizes of $\sim$ 50 parsec, and an average density of the order of $\sim$ 200 H_2 per cm^3 (Blitz 1993). The upper limit to their mass can be as high as 6 $\times 10^6$ $M_\odot$ (Williams & McKee 1997). At this temperature range, the dense molecular clouds are not transparent at optical wavelengths due to the dust extinction,

they can thus only be observed at infrared and radio wavelengths. H_2 is the most abundant element in the GMCs, but it is difficult to detect at these cool temperatures as it is a symmetric molecule and lacks a dipole moment. Instead, the second most abundant molecule, carbon-monoxide CO, is often used to trace H_2 molecules as it can be excited at these cool temperatures as it possesses many rotational lines. Molecular clouds are not homogeneous over the whole clouds but are highly fragmented and contain smaller clumpy structures (Blitz & Williams 1999; Williams *et al.* 2000). The clumps have masses of thousands of solar masses, sizes of several parsecs and densities of the order of $10^3 - 10^4$ H_2 per cm^3. In turn, within the clumps there are smaller substructure cores with masses of order of $0.5 - 5$ $M_\odot$, sizes of order of ~ 0.1 parsec and densities of the order of $10^4 - 10^5$ H_2 per cm^3 (Larson 2003; Bergin & Tafalla 2007). The temperature of the gas in clumps and cores is typically similar to the original molecular clouds. It is believed that the clumps are the site of forming clusters while single stars form from the cores. The initial conditions of star formation depend on the properties of the molecular clouds. Essentially, the stars form after the molecular cloud collapses when the gravity overcomes the thermal pressure. In general, the formation of stars is divided into two main categories: Low mass star formation which is fairly well understood and high mass star formation which is still unsolved.

1.2 Low Mass Star Formation

As discussed in the earlier section, stars form from the dense core of molecular clouds when it collapses under its own gravity. Shu *et al.* (1987) proposed a simple classical model to describe the collapse of a molecular cloud. It should be stressed

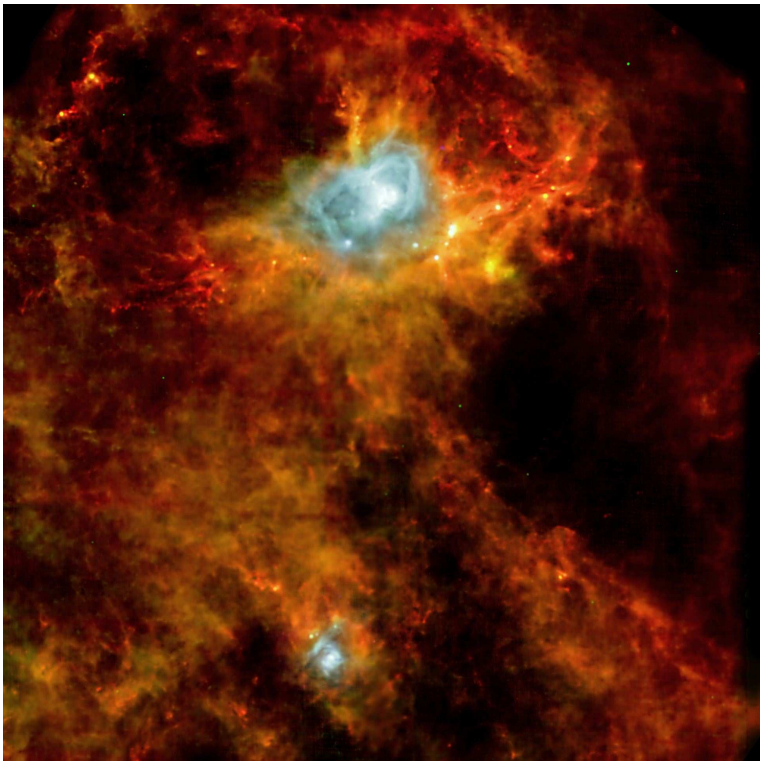

Figure 1.1: The figure shows a 3-colour composite PACS/SPIRE of the Aquila region. The red, green and blue are SPIRE 500 μm, PACS 160 μm and PACS 70 μm respectively. The figure is taken from André *et al.* (2010).

that this model only considers that the cloud is thermally supported. This is an over simplified scenario as it is believed that the clouds are also supported by magnetic fields, rotation and turbulence, however, it still gives a good overall picture of the process. The minimum mass required for an isothermal sphere which is only thermally supported to collapse is characterised by the Jeans mass according to the following equation.

$$\mathrm{M_J} = \left(\frac{5k_bT}{\mathrm{G}\mu m_H}\right)^{\frac{3}{2}} \left(\frac{3}{4\pi\rho}\right)^{\frac{1}{2}} \tag{1.1}$$

Where M_J is the Jeans mass, k_b the Boltzmann constant, T the thermal tem-

perature, G the gravitational constant, ρ the density, m_H is the mass of hydrogen and μ is mean mass per particle. Thus, the Jeans mass is positively related to the temperature of the cloud while it is inversely related to the density of the cloud. First, the core will collapse at free fall time from inside to outside to form a protostellar object as the inner regions are denser than the outer regions (Shu 1977; Larson 1969). At the beginning of the collapse, the density increases while the temperature remains constant. This is because at this stage the core is still optically thin and efficiently radiates the heat away from the core. Consequently, the Jeans mass decreases allowing even further fragmentation. When the core becomes opaque to the radiation as the density keeps increasing, the radiation will be trapped causing the temperature to increase. At this point the thermal pressure halts the collapse and a hydrostatic core will be formed with a radius of $\sim$ 5 au and a mass around 0.05 $M_\odot$ (Masunaga *et al.* 1998). The hydrogen molecule begins to dissociate when the temperature of the core reaches $\sim$ 2000 K which leads to a second collapse (Masunaga & Inutsuka 2000). The second hydrostatic core will form following the dissociation of hydrogen molecule when the temperature reaches 10000 K at $\rho \sim 0.1$ g cm^{-3} (Masunaga & Inutsuka 2000). Essentially, the hydrostatic core at this stage is the final collapsed protostar. Following this, the accretion stage starts when the material accretes onto the protostar at free-fall time scales results in the protostar rapidly growing. Eventually the protostar evolves to become an optically visible pre-main sequence star as a T Tauri star.

As mentioned earlier this is a simplistic picture of star formation, the role of the magnetic field and rotation of the core are not considered. However, the effects of them are believed to be crucial in structuring the geometry of the accreted

material onto the star. The conservation of angular momentum due to rotation leads to the formation of a disk around the protostar, with the star accreting mass from the infalling material via this disk. The excess angular momentum can also be removed by bipolar jets and outflows. Eventually, the outflows and collimated jets will disrupt the natal clouds and reveal the star with the disk.

Observationally, based on the spectral energy distribution (SED), the evolutionary stages of young stellar objects (YSOs) have been classified into four classes. Lada (1987) proposed three classes (I,II and III), later an extra class (class 0) was introduced by Andre *et al.* (1993), all the classes are shown in Fig. 1.2. Lada (1987) classified class (I,II and III) based on the spectral index α of the slope of their SED.

$$\alpha = \frac{\mathrm{d}\log\lambda F_\lambda}{\mathrm{d}\log\lambda} \tag{1.2}$$

According to the proposed classification, the class 0 objects represent the early stage of star formation, where the protostar is totally obscured by its dusty envelope at infrared wavelengths and its SED shape is very similar to a black body peaking at mm wavelengths. Class I objects have a wider SED than a black body, which indicates that a large amount of IR radiation comes from circumstellar dust around the protostar. The outflows from the poles dissipate the circumstellar envelopes. The class I objects have a spectral index of $0 < \alpha \leq 3$. Class II objects also have a wider SED than a black body with IR excess but less circumstellar dust emission than class I. The SED of class II objects is characterised as a T Tauri pre-main sequence star, having a spectral index of $-2 < \alpha \leq 0$. The final evolutionary stage, class III objects are optically visible and have a similar SED to a black body

with a weak IR excess, indicating a small amount of circumstellar dust around the object. The SED of class III has a spectral index of $-3 < \alpha \leq -2$ and represents the photospheres of very evolved stars near or on the main sequence. At this stage, the outflows have dissipated most of the circumstellar envelopes and therefore it is believed young stars evolve from class 0 with a large amount of circumstellar dust to class III with very little circumstellar dust in its envelope.

1.3 High Mass Star Formation

Unlike low mass stars, the formation of massive stars is one of the most outstanding problems in astrophysics. The main difference between low mass stars formation and high mass stars formation is that massive stars evolve fast. In fact the Kelvin-Helmholtz (t_{KH}) timescale (given in equation 1.3) is shorter than the free fall (t_{ff}) timescale (given in equation 1.4).

$$t_{KH} = \frac{G{M_\star}^2}{R_\star L_\star} \tag{1.3}$$

$$t_{ff} = \left(\frac{3\pi}{32G\rho}\right)^{\frac{1}{2}} \tag{1.4}$$

Where $M_\star$, $R_\star$ and $L_\star$ refer to the final mass, radius and luminosity of the formed star, G is the gravitational constant and ρ is the density of collapsed core. For a typical core number density, 10^4 cm^{-3}, t_{ff} is $\sim 4 \times 10^5$yrs. The t_{KH} for a solar mass star is $\sim 3 \times 10^7$yrs which is considerably longer than t_{ff}. Assuming $L_\star = M_\star^{3.3}$ for main sequence stars, we see $t_{KH} \propto M_\star^{-1.3}$ and we find that it becomes shorter than t_{ff} for stars with masses $\geq 10M_\odot$. Therefore, massive stars begin

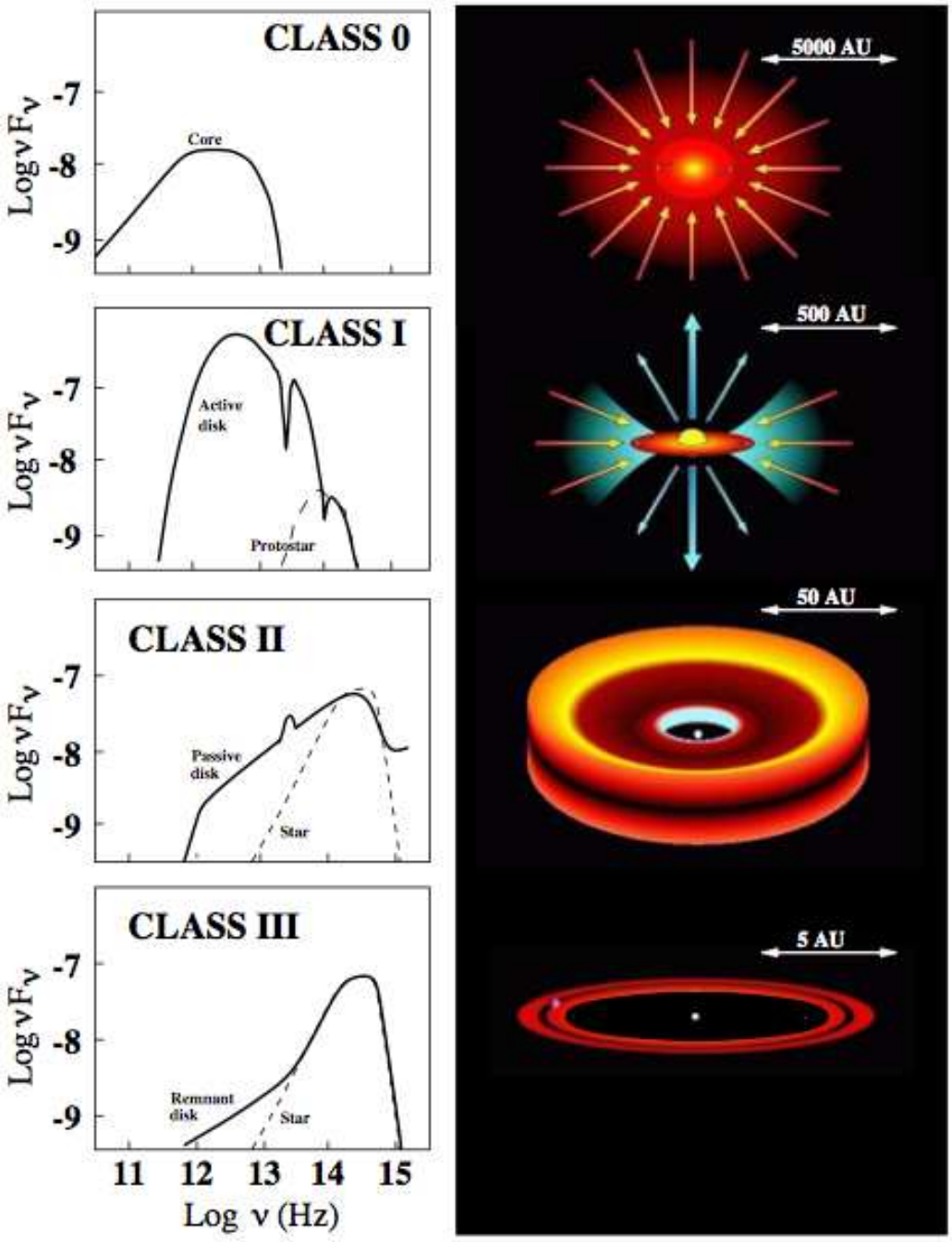

Figure 1.2: Schematic showing the evolution of the circumstellar disk of PMS. The left hand side shows the SEDs of each class while the circumstellar geometry of the corresponding classes is shown on the right hand side. The figure is taken from Isella (2006).

nuclear burning and reach the zero-age main sequence (ZAMS) still embedded in their natal cloud and are still experiencing accretion. This makes the pre-main sequence phase invisible. Theoretically one of the biggest problems in massive star formation is the radiation pressure. In fact, the radiation pressure for a massive star (∼15 M⊙) overcomes the gravitational pressure. This could halt the accretion of materials onto the star from a spherically symmetric envelope. In this way stars only up to ∼15 M⊙ can be formed. However, massive stars above ∼100 M⊙ are observed (Crowther *et al.* 2016). In addition, due to the nature of initial mass function (IMF), massive stars are very rare compared to low mass stars (Salpeter 1955). Furthermore, massive stars form in very far and dense regions, where there is high extinction, hence it is very challenging to observe such stars in the optical and infrared.

There are two main theories describing the possible formation of high mass stars which are disk accretion and competitive accretion. Disk accretion is the scaled up of the disk accretion of low mass stars through a monolithic collapse of a high density core within molecular clouds and processing the accretion via a disk. The difficulty is how mass is accumulated as massive stars have very strong radiation. Yorke & Sonnhalter (2002) simulated a model based on this theory, they found that stars of masses 31.6 $M_\odot$, 33.6 $M_\odot$, and 42.9 $M_\odot$ can be formed from non-magnetic, rotating massive molecular clumps of masses 30 $M_\odot$, 60 $M_\odot$, and 120 $M_\odot$ respectively, taking into account the strong radiation from the stars. Stars of masses up to even ∼140 $M_\odot$ can be formed via this model (Kuiper *et al.* 2010). They overcome the radiation problem with the idea that the radiation far from the stars becomes anisotropic and will have less effect on the equatorial disk but it still efficiently escapes via poles through the cavity formed by the outflows.

This model allows massive stars to be formed in isolation.

The alternative scenario to disk accretion is the competitive accretion scenario which has been proposed. It considers that all stars are initially formed as low mass stars and in dense molecular clumps (Bonnell *et al.* 1997). They start to accumulate from unbound gas as there is a significant amount of gas. The rate of accretion depends on the star's mass, star's location and the density of the gas. Therefore in the central region, where the gas is densest and has the lowest velocity dispersion, the accretion is the highest. This allows central stars to accumulate more material than other stars while stars not located at the centre accumulate less due to the lower gas density and higher gas dispersion. The main difference between these two scenarios is that in the disk accretion model, stars can be formed in isolation while in the latter one a cluster is the origin of the formation. Most massive stars are associated with clusters (e.g. (Lada *et al.* 1991) but they also rarely can be formed in isolation (de Wit *et al.* 2004, 2005).

1.4 Herbig Ae/Be Stars

HAeBe stars, the more massive counterparts of T Tauri stars, are optically visible pre-main-sequence (PMS) stars with masses roughly between 2 and 10 $M_{\odot}$. With their intermediate masses, they bridge the gap between low mass stars and high mass stars. This group of stars was first identified by Herbig (1960) in a study of 26 objects, according to the following three distinct criteria. "The star has a spectral type of A or B with emission lines, lies in an obscured region and illuminates a fairly bright nebulosity in its immediate vicinity". Subsequent studies (see e.g. Finkenzeller & Mundt 1984; The *et al.* 1994; Waters & Waelkens 1998;

Malfait *et al.* 1998) adjusted the criteria slightly. The spectral type was extended to include spectral type of F. One of the main criteria that have been added is that these stars possess a significant amount of IR excess due to the dust in the circumstellar environment as seen from their SED. In addition, they do not need to be associated with nebulosity and star forming regions.

Hillenbrand *et al.* (1992), in a study of 47 stars, classified HAeBe stars based on their SEDs into three groups: I, II and III. In Group I stars, the large amount of IR excess seen in their SEDs is interpreted by an optically thick flattened accretion disk which is optically thin in the inner regions around the stars. Group II objects, possess a flat or increasing IR-excess, this is best described by a photosphere surrounded by an envelope of gas and dust. Group III stars, similar to classical Be stars, only show a small amount of IR-excess. The last group objects are best represented by a disk-less intermediate mass star similar to disk-less T Tauri stars.

HAeBe and T Tauri stars are similar in many ways, for example in their emission lines and line polarisation (see e.g. Hamann & Persson 1992; Vink *et al.* 2005a). The main distinctions between the two groups are: HAeBe stars are thought to have a radiative photosphere, therefore unlike T Tauri they are not expected to have a magnetic field. In addition, HAeBe stars evolve more rapidly towards the main sequence.

HAeBe objects not only have some common characteristics with high-mass objects such as clustering (Testi *et al.* 1999) but also have spectropolarimetric characteristics in common with T Tauri stars (Vink *et al.* 2005a). Vink *et al.* (2005a) find similar spectropolarimetric line effects across Hα in HAe stars and T Tauri stars. As the origin of such a line effect is explained by the presence

of emission line from accretion channel or accretion spot, this could suggest that HAeBe stars might also have magnetic fields. Therefore, the study of the formation of HAeBe stars can bring out the differences in the mechanisms of the formation of low- and high-mass stars. In addition, because they are closer and less embedded than massive young stars, HAeBe stars can act as a powerful test bed for the formation of massive stars.

1.5 Circumstellar Disk Polarisation

As mentioned earlier, circumstellar disks are the outcome of the conservation of angular momentum during the initial collapse of the molecular clouds. The circumstellar disk plays a key role in many star formation processes such as the accretion occurring in the inner disk of order of a few au. However, despite its importance, the observation at such small spatial scales is challenging. The conventional direct imaging technique can spatially resolve nearby objects. Nevertheless, its spatial resolution reduces significantly with distance which makes it difficult to study massive stars as they usually reside faraway. In contrast, polarimetry is a robust technique to probe small spatial scale of order of stellar radii of distant objects as it totally independent of distance. Polarimetry is especially useful in studying disk-like structures around stars. Even more complicated structures such as outflows, expansion, accretion and rotation can be studied with sophisticated models. Polarimetry provides information about the presence of asymmetric structures, the asymmetry could be introduced by magnetic fields or particle scattering. The technique could be even more powerful when combined with spectroscopy which adds the wavelength distribution of light to the

polarisation vector. Thus by performing spectropolarimetry (polarimetry with spectroscopy) we can categorise regions and diagnose stellar activities within the circumstellar environment around stars through distinguishing between polarisation from different components of spectral features.

1.5.1 Polarimetry

Most of the observational techniques such as spectroscopy, direct imaging, photometry and interferometry measure the intensity of radiation coming from astronomical objects as a function of wavelength. Although we can learn a lot from these techniques, we miss a very important property of light which is polarisation. Light is an electromagnetic wave, it oscillates with no preferred direction when it is not polarised while the oscillation will be in a certain direction when the light is polarised. Thus by measuring the direction of the preferred oscillation we can measure polarisation which will be unknown otherwise. Polarimetry provides information about the agents breaking the symmetry, this could be caused by the presence of a magnetic field evidenced by the Zeeman effect in the observed spectrum or the scattering of photons by scatterers from the asymmetrical environment. The scatterers could be free electrons or dust grains within the circumstellar environment. Essentially, if we have any aspherical geometry, for instance an axisymmetric disk, we expect a measurable level of polarisation. Most astronomical objects provide some level of polarisation as the presence of an ideal symmetry is very rare. However, most astronomical objects have a very low degree of polarisation of typically a few percent. Detecting such a low polarisation is challenging.

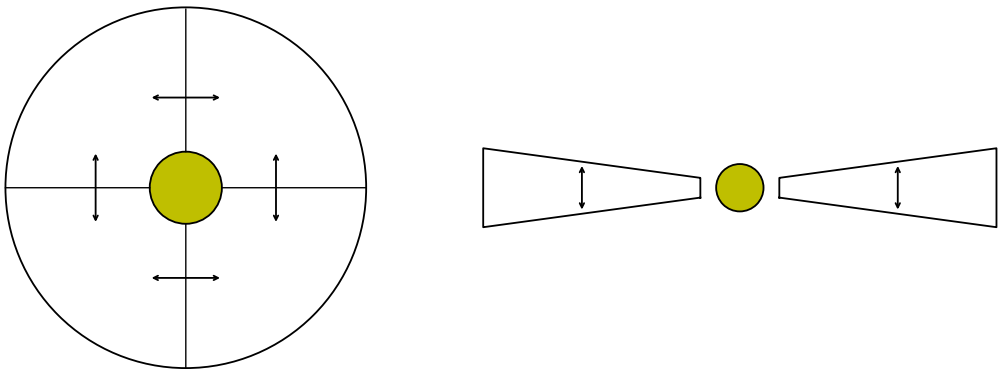

Figure 1.3: Schematic showing how the observed polarisation depends on the geometry of the circumstellar environment. The left image shows a circular geometry where the distribution of material is spherical or the disk is viewed pole-on, the arrows show the direction of polarisation. In such a geometry and orientation, all polarisation vectors cancel each other out resulting in zero net polarisation. The right hand side image shows a circumstellar disk viewed edge-on, in this case there is no cancellation and a net polarisation is detected.

Polarisation is related to the spatial structure of an astronomical object regardless of the distance. Let us assume that the distribution of the circumstellar dust or free electrons in the ionised region close to the star is spherical. As shown in Fig. 1.3 left image, the photons are scattered by electrons or dust grains and the direction of polarisation is perpendicular to the line between photons and the scatterers. The polarisation in the poles cancel out the polarisation in the equatorial regions which leads to zero net polarisation. However, if the distribution of the material is not entirely spherical (for example in the case of clumps) a net polarisation could be observed. In addition, if the system is aspherical but viewed pole-on at inclination angle of 0° (Fig. 1.3 left image), again zero net polarisation is expected for the same reason. However, in the case of a disk viewed edge-on as seen in 1.3 right image, we observe a net polarisation as the

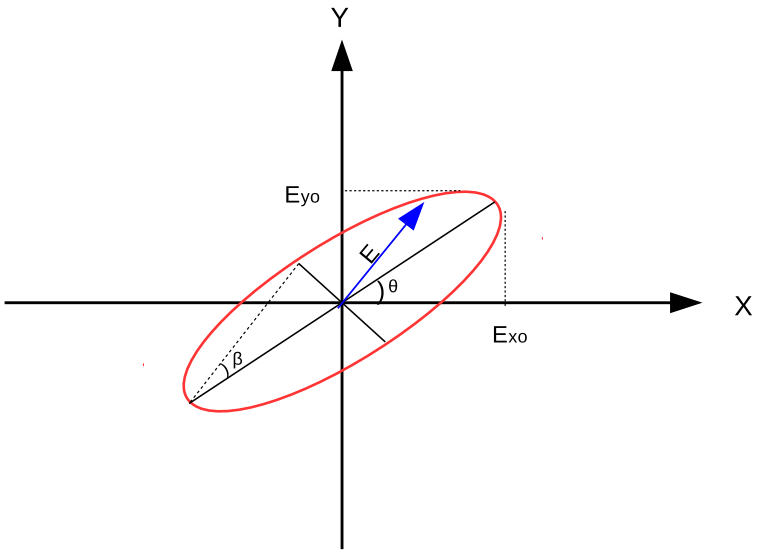

Figure 1.4: The diagram shows the polarisation ellipse. The electric vector E follows an ellipse shape in the x-y plane, the direction of propagation is in z direction. θ is the polarisation angle while the angle β determines the axial ratio of the ellipse.

polarisation is perpendicular to the midplane of the disk and there will not be any cancellation. Therefore, a level of polarisation is expected depending on the degree of inclination and asymmetry of the circumstellar disk.

1.5.2 Stokes Parameters

We now consider the general form of polarisation, elliptical polarisation, to define the Stokes parameters. The elliptical polarisation can be considered to consist of two orthogonal electric fields propagating in the z direction (see Fig. 1.4). The electric fields of the two waves can be written as follows:

$$\begin{aligned} E_x &= E_{xo}\ \cos(\omega t) \\ E_y &= E_{yo}\ \cos(\omega t + \phi) \end{aligned} \tag{1.5}$$

where ω is the angular frequency and ϕ is the phase difference between the two waves. If the phase difference is 0° or 180°, the light is considered to be linearly polarised. If E_{xo} is equal to E_{yo} and the phase difference is 90° or 270° then the light is circularly polarised.

The polarisation state of electromagnetic radiation is fully described by the four Stokes parameters I, Q, U and V (Tinbergen 1996; del Toro Iniesta 2007). These parameters can be described mathematically according to the following equations (for more details on obtaining the equations see Goldstein 2003):

$$\begin{aligned} I &= E_{xo}^2 + E_{yo}^2 \\ Q &= E_{xo}^2 - E_{yo}^2 \\ U &= 2E_{xo}E_{yo}\cos(\phi) \\ V &= 2E_{xo}E_{yo}\sin(\phi) \\ I^2 &= Q^2 + U^2 + V^2 \end{aligned} \tag{1.6}$$

where I is the total intensity, Q and U are the intensities in different orientations: Q is the difference in intensity of the electric field oscillating at 0° and 90° while U is the difference in intensity of the electric field oscillating at 45° and 135°. Both Q and U are necessary to describe the linear polarisation of a source. Finally, V describes the circular polarisation and it is the difference in intensities between the right and left handed circular polarisation.

The degree of polarisation can be measured from the Stokes parameters according to the following equation:

$$P = \frac{I_{pol}}{I} = \frac{\sqrt{Q^2 + U^2 + V^2}}{I} \tag{1.7}$$

Where I_{pol} is the sum of the polarisation component Q, U and V. If P = 0 the light is considered to be unpolarised while if P = 1 then the light is completely polarised. Anything in between 0 and 1 is considered as a partially polarised light. As the degree of polarisation is usually very low, typically a few percent, the Stokes parameters are commonly normalised (divided by the total intensity) to provide the fraction of polarisation in each Stokes parameters. In this thesis the capitals Q,U and V always denote the fractional values. Q, U and V can have positive or negative values, while I is always positive.

The polarisation angle is given by

$$\tan(2\theta) = \frac{E_{xo}E_{yo}\cos(\phi)}{E_{xo}^2 - E_{yo}^2} \tag{1.8}$$

Therefore,

$$\tan(2\theta) = \frac{U}{Q} \tag{1.9}$$

As the polarisation can not be directly measured at the telescope, we need to filter the light coming from a target source to recover the Stokes parameters (see Fig. 1.5). In the case of linear polarisation, Q and U, a rotatable half wave retarder plate is commonly used to control the orientation of polarisation. At least four position angles are required to fully recover the linear Stokes parameters. For circular polarisation, two filters are used to separate the positive (right-handed) and negative (left-handed) circular polarisations. Finally, the Stokes parameters

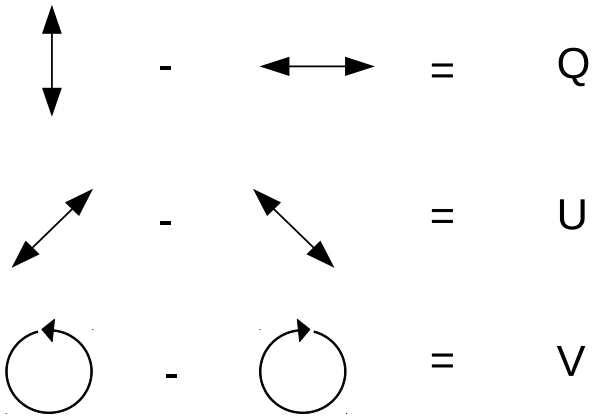

Figure 1.5: The figure shows the filters needed to recover the stokes parameters Q, U and V.

can be recovered according to the following equations:

$$\begin{aligned} I &= I_0 + I_{90} = I_{45} + I_{135} = I_+ + I_- \\ Q &= I_0 - I_{90} \\ U &= I_{45} - I_{135} \\ V &= I_+ - I_- \end{aligned} \tag{1.10}$$

where I_0, I_{90}, I_{45}, I_{135} are the intensities of the electric field oscillating at 0°, 90°, 45° and 135° respectively. I_+ and I_- are the intensities of positive (right-handed) and negative (left-handed) circular polarisations.

The astronomical polarisation is usually presented in a *(Q, U)* diagram where the Stokes Q is plotted against Stokes U (see Fig. 1.6). In the Figure, the length of the vector P represents the amount of polarisation and its direction indicates

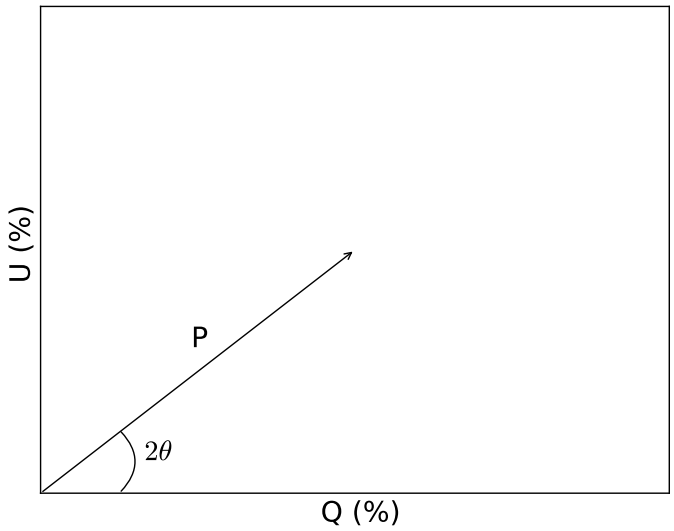

Figure 1.6: Normalised Stokes parameters U is plotted against Q, the length of vector P represents the amplitude of polarisation and its direction represents the direction of the polarisation.

the direction of polarisation. From the Figure:

$$\begin{aligned} Q &= P\ \cos(2\theta) \\ U &= P\ \sin(2\theta) \end{aligned} \tag{1.11}$$

Once you have the linear polarised light, Q and U, and the total intensity I, scattered and direct light, one can measure the percentage of polarisation and polarisation angle according to the following equations:

$$\begin{aligned} P &= \sqrt{Q^2 + U^2} \\ \theta &= \frac{1}{2} \arctan\left(\frac{U}{Q}\right) \end{aligned} \tag{1.12}$$

1.5.3 The Tool of Spectropolarimetry

Spectropolarimetry of stars is capable of revealing the spatial structure of the circumstellar environment. The key point is to understand whether the ionised region around the star is spherically symmetric or not by examining the scattered light from free electrons. In such an ionised region, where the density of free electrons is the highest, the free electrons scatter the continuum radiation coming directly from the stellar photosphere as well as the hydrogen recombination lines from the hot ionised disk. If the geometry of the scattering electrons, the inner disk, is not circular but a flattened structure on the sky, net polarisation will be detected (see Fig. 1.3). However, detecting polarisation towards an object by itself is not enough to confirm the presence of a disk. This is complicated by the presence of polarisation due to the interstellar medium and circumstellar dust further out from the star unless the star is very close to us and has no circumstellar dust. The subtraction of the foreground polarisation from the intrinsic polarisation is challenging. A few methods have been used but they usually do not give accurate measurements.

Here is where the spectral polarimetry comes in. It uses the fact that the hydrogen recombination photons will be less polarised than the continuum photons. This is because unlike the continuum light, emission lines pass through a smaller ionised volume and hence encounter less free electrons. Ultimately, the emission line will be less polarised than the continuum. This behaviour is absent in the case of interstellar medium and circumstellar dust. The interstellar medium has a broad wavelength dependence and the circumstellar dust is located over a much larger area than hydrogen recombination lines. As a consequence, they polarise

continuum and emission photons equally. Therefore, any detection of change in polarisation across the emission lines is directly traced to the presence of a disk regardless of the contribution of the foreground polarisation. Thus, performing polarimetry across a particular spectral feature does not require the knowledge of foreground polarisation as it does not affect the results. In fact, it does only add a constant value to the Stokes parameters Q and U.

The *(Q, U)* diagram is another way to look at the polarisation, we can measure intrinsic polarisation accurately from the slope of the line effect regardless of the contribution of the foreground polarisation. Another advantage of spectropolarimetry is that we can establish the orientation of disk even if it is not resolved. As seen in the Fig.1.3, the polarisation is perpendicular to the circumstellar disk. Thus, the position angle of a circumstellar disk on the sky is $\pm 90^{\circ}$ from the polarisation position angle.

The only downside aspect of spectropolarimetry is that the technique is restricted by the number of observed photons, in fact the technique is a "photon-hungry" method. Therefore the main uncertainty in the observed polarisation is due to photon statistics. This is why it requires a large telescope or a very long integration times compared to other observational techniques. As a rule of thumb:

$$\Delta P(\%) \simeq \frac{100}{\sqrt{N}} \tag{1.13}$$

The typical line effects are of order 0.5% and hence to properly sample the polarization behaviour as a function of wavelength, one needs a polarisation precision of order 0.1%. This requires 10^6 photons, SNR $\sim$ 1000, per resolution

element. It is difficult to achieve such accuracy especially for faint objects. To reduce the uncertainty, the spectra can be rebinned but this comes at the cost of reducing the spectral resolution.

1.5.4 Spectropolarimetric Line Effect

As discussed above the line effect refers to the change in polarisation across spectral features such as Hα line. Mainly there are two types of line effects, depolarisation and intrinsic line polarisation. The line effect is as broad as the emission line in depolarisation while it is narrower in intrinsic line polarisation. There is another sub-type line effect called the McLean effect across the absorption component of the emission line. Fig.1.7 shows a cartoon explaining the situations without a line effect, depolarisation and line polarisation across Hα line. The figure is a combination of triplots (left) and (*Q, U)* diagrams (right). In the triplot, the Stokes I (normal intensity) is shown in the lower panel, the polarisation percentage in the middle, while the position angle (PA) is shown in the upper panel. In the figure, also the Q and U Stokes parameters are plotted against each other beside each triplot.

1.5.4.1 No Line Effect

In the case where the circumstellar environment is circular on the sky. The circular geometry could be due to spherical distribution or the disk is viewed pole-on. As is shown in Fig. 1.7 top images, there is no change in polarisation across the line in the triplot and all the Q and U values in the (*Q, U)* diagram are concentrated in a single dot representing the continuum polarisation. The non-detection of the line effect could be due to the fact that the geometry is

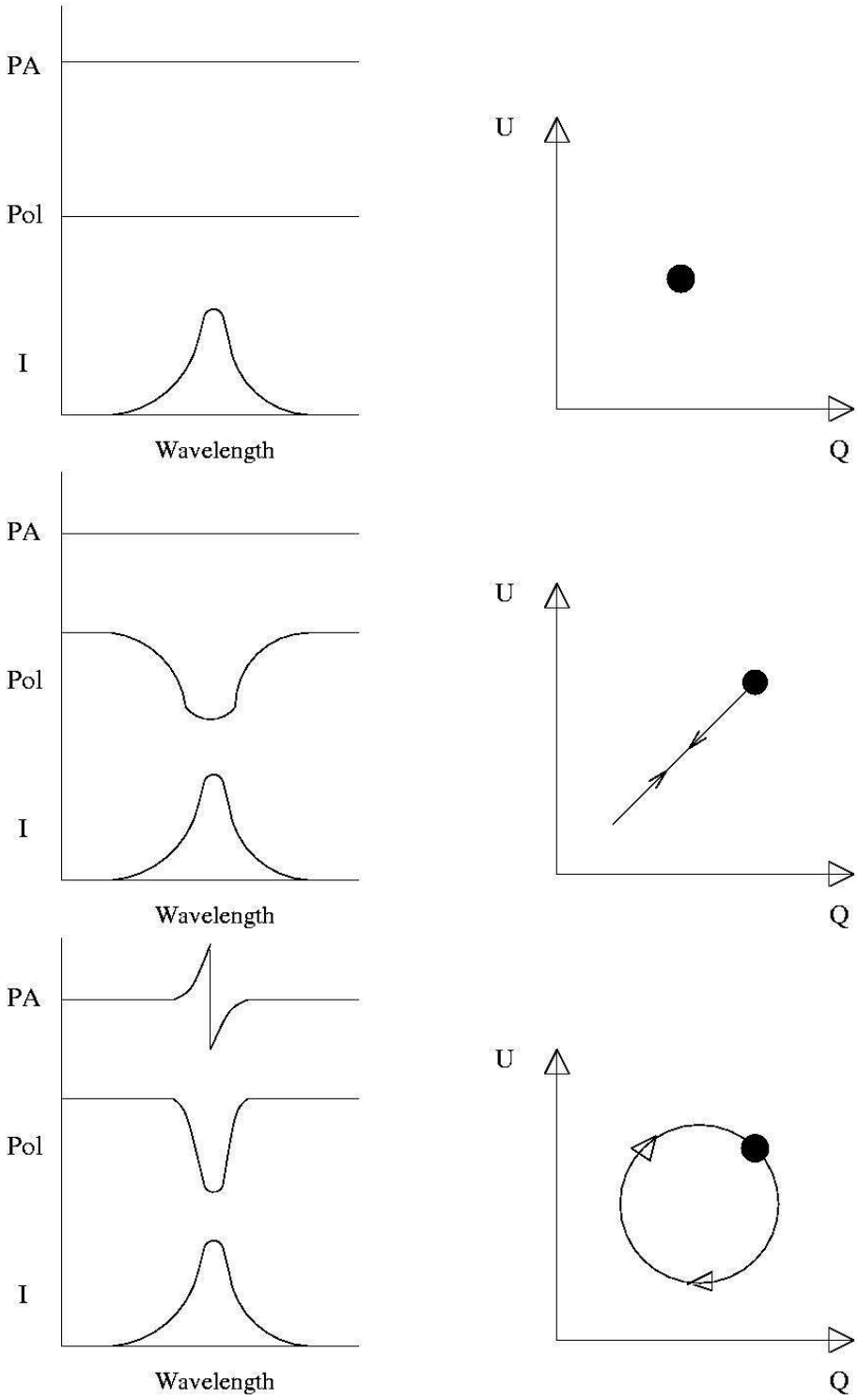

Figure 1.7: Cartoon showing Spectropolarimetry across Hα line in a combination of triplots (left) and (*Q, U)* diagrams (right). In the triplot polarisation spectra the Stokes intensity (I) is shown in the lowest panel, polarisation (%) in the centre, while the position angle (PA) is shown in the upper panel. The Q and U Stokes parameters are plotted against each other beside each triplot. The upper plots show no line effect, the depolarisation line effect is presented in middle plots and finally the bottom plots show the intrinsic line polarisation. The figure is taken from Vink *et al.* (2002).

spherically symmetric, or that the disk is close to face-on.

1.5.4.2 Depolarisation

Depolarisation has been observed in classical Be stars and in massive late HBe stars. Depolarisation line effect is where the drop in polarisation is as broad as the emission line (see Fig 1.7 middle left). In this case it is assumed that a large portion of hydrogen emission lines are formed in an extended ionised region around a star. When the polarisation translates into (*Q, U)* diagram we see a line excursion from the continuum knot towards the line (see Fig 1.7 middle right).

1.5.4.3 Line polarisation

This type of line effect is found towards the less massive and cooler stars than the objects displaying the depolarisation line effect. It has been observed in T Tauri stars and HAe stars by Vink *et al.* (2005a). In this case the line is intrinsically polarised instead of exhibiting a depolarisation. The intrinsic line polarisation is thought to be caused by the effects of magnetospheric accretion, where the material from the disk is funnelled via accretion columns on to the stars, causing a shock to the photosphere. The emission lines coming from this hot spot will be polarised as they scatter off the disk material due to the doppler shift this becomes visible as a line effect (Vink *et al.* 2005b). The line effect is narrower than the emission line compared with depolarisation and a loop is expected to be present in the (*Q, U)* diagram caused by a flip in the polarisation angle (see Fig 1.7 bottom images)

1.5.4.4 McLean effect

The concept of the McLean effect is based on the fact that the the wind material in our line of sight blocks the unscattered light and removes it from the beam. This leads to observation of a strong emission line with a blueshifted absorption component. However, the flux in the absorption does not reach zero because the re-emission process is isotropic; some of the photons will be scattered into our line of sight. If the distribution of the material is aspherical, the observed light across the absorption will be more polarised than the continuum light. In addition to that, some of the photons could get through the wind material without scattering, depending on the density of the wind.

1.5.5 (*Q, U)* diagram

The (*Q, U)* diagram, where the wavelength dependent Stokes U is plotted against Q, is very useful to categorise the wavelength dependent geometry of the circumstellar disk. The magnitude of the line effect and the polarisation angle can be directly measured from the slope of the line effect (see Fig. 1.6). The polarisation angle is very important to establish the disk orientation but careful analysis is required to measure it correctly. The intrinsic polarisation angle is measured from the line to the continuum for depolarisation line effect while the opposite is true for intrinsic line polarisation. The intrinsic angle is measured according to the equation 4.1. For instance the [Q U] value of [1 1] and [-1 -1] result in the same polarisation angle of 22.5° despite each being located in a different quadrant in Fig. 1.8. Thus, the angle for [-1 -1] should be 112.5° (22.5° + 90°) resulting a difference of 90° with [1 1].

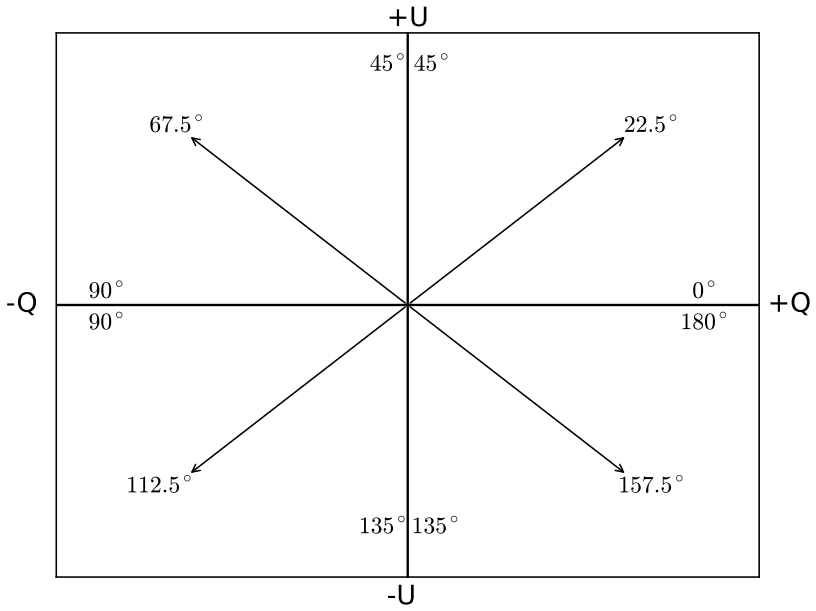

Figure 1.8: Normalised Stokes parameters U is plotted against Q. The polarisation angle is measured by using $\theta = \frac{1}{2}\arctan\left(\frac{U}{Q}\right)$. From the equation it is clear that the angle is indistinguishable between: [+U,+Q] and [-U,-Q]; [+U,-Q] and [-U,+Q] for the same values of Q and U. In fact there should be a 90° difference between each pair.

1.5.6 The Application of Linear Spectropolarimetry

Spectropolarimetry has been used in the 1970s to study the circumstellar environment of Be stars by Clarke & McLean (1974); Poeckert & Marlborough (1976). They found that Be stars are surrounded by an spherically asymmetric envelope. At that time, the disks could not be spatially resolved. It was only in 1994 when Quirrenbach *et al.* (1994) could directly confirm the disk hypothesis by using interferometric observations of a Be star. In the late 1990s and early 2000s Oudmaijer & Drew (1999); Vink *et al.* (2002), expanded the use of the technique to apply to HAeBe objects.

Vink *et al.* (2002) found that 7 out of 12 Herbig Be (HBe) objects have a depolarisation line effect across Hα as found in Be objects. These line effects are as broad in polarisation as the line spectra themselves. This suggests that Hα is formed over an extended volume in the circumstellar medium. However, Vink *et al.* (2002) found a different line effect, line polarisation, across 9 out of 11 Herbig Ae (HAe) objects. They proposed the line itself is intrinsically polarised as probably part of the emission lines from a compact region, where the accretion takes place as explained above. Vink *et al.* (2005a) found that HAe stars have a similar spectropolarimetric signature to T Tauri while HBe stars have a different signature than HAe and T Tauri stars.

1.6 Motivation and Thesis Overview

Unlike low mass stars, the formation of massive stars is poorly understood. Observationally, the main challenge is that they are located faraway and deeply embedded in their natal clouds. The physical properties of HAeBe stars make them a very key class of stars to improve our understanding of such a long-standing puzzle in astrophysics. The circumstellar environment is a key element in many phases of star formation, yet determining its geometry often poses a challenge. One of the most effective way to overcome the observational challenges is to use spectropolarimetry. The technique is unconstrained by distance and very powerful to probe very small spacial scales of order solar radii around stars. In this thesis I represent the results of spectropolarimetric observations of 28 HAeBe objects. The data were obtained with the FORS2 instrument on the VLT in Chile and the ISIS instrument on the WHT in La Palma. The FORS2 medium

resolution spectra cover the entire optical range, and comprise the largest spectropolarimetric wavelength coverage, 4560 Å to 9480 Å, published to date. In addition to spectropolarimetry, other observational tools were used to enhance and further investigate the circumstellar environment of two stars, including near infrared interferometry and optical spectroscopy. This thesis is structured as follows:

- Chapter 2 presents the FORS2 spectropolarimetric observations of 12 HAeBe objects. The observations and the data reduction procedures are discussed. The large wavelength coverage of FORS2 enables us to assess and make a direct comparison between the spectropolarimetric properties of Hα and other emission lines within the same spectrum at the same resolution. This has never been studied in this manner before. All the emission lines are spectropolarimetrically investigated and classified with different volumes within the circumstellar environment.

- Chapter 3 presents an in-depth study of two particularly interesting objects PDS 27 and PDS 37 from the FORS2 sample. The X-shooter spectroscopic data were used to measure their stellar parameters. The X-shooter data are also provide further clues about the nature of the circumstellar environment through analysing the observed spectral lines. The spectrometric and spectroscopic observations are complimented with the high angular resolution of the PIONIER near infrared interferometric data. The observed interferometric visibilities of both objects can be explained with a binary nature of the system.

- Chapter 4 presents the first spectropolarimetry of HAeBe stars across He

I line at 1.083 μm obtained with the NICS instrument on the TNG. The chapter also provides a statistical investigation of the spectropolarimetric line effects in HAeBe stars. In this chapter, the FORS2 sample, 12 objects, are combined with a sample of 17 HAeBe stars observed with the ISIS on the WHT. The sample size is increased to 56 HAeBe objects by adding all the previous spectropolarimetric investigations to draw a better statistics.

- Chapter 5 presents the main conclusions of the thesis and the future studies of the circumstellar disks around young stars.

Chapter 2

Linear Spectropolarimetry Across the Optical Spectrum of Herbig Ae/Be Stars

2.1 Introduction

Despite the important role of massive stars in the evolution of the interstellar medium and unlike their counterpart low mass stars that are thought to be formed via magnetospheric accretion (Muzerolle *et al.* 1998), their accretion mechanism is still open to debate. Observationally, the detection of massive stars is challenging as they reside far away and are deeply embedded in their natal clouds. As an alternative to massive stars, the intermediate mass HAeBe stars are the best candidates to address this issue. They are optically visible and bridge the gap between low and high mass stars. The current view is that HAeBe stars are surrounded by disks through which material continues to accrete onto the star

(e.g. Ilee *et al.* 2014), although the precise scenario is not known (for reviews on the topic, see Grady *et al.* 2015; Kraus 2015; Beltrán & de Wit 2016).

In order to make progress, one needs to study the circumstellar environment through which the material accumulates onto the star via accretion channels. This requires methods capable of probing the matter very close to the star, as this is where the accretion action happens. A key point is the observation of whether the ionised region around the star is spherically symmetric at small scales or not. If it is not, then the possibility that a flattened structure is observed lends support to the disk accretion scenario responsible for the formation of such stars. Studying the circumstellar environment at these small scales is possible through linear spectropolarimetry, measuring the scattering of photons off free electrons in a dense, ionised gas.

The idea of spectropolarimetry is that in the ionised region, free electrons scatter and polarise continuum photons from the central star. If the geometry is not circular on the sky, for example in the case of flattened disk, a net polarisation can be detected. However, emission photons undergo less scattering as they emerge further away from the central star. If the polarisation is measured as a function of wavelength, this difference in scattering will be visible as a change in polarisation across the line, which is often simply referred to as the "line effect". The observed de-polarisation across the Hα line constituted the first evidence that the class of Be stars were surrounded by disks (Clarke & McLean 1974; Poeckert & Marlborough 1976). This was only much later confirmed by direct observations (e.g. Quirrenbach *et al.* 1994 based on image reconstruction of interferometric data; Wheelwright *et al.* 2012 using sub-milliarcsecond precision spectro-astrometry).

Oudmaijer & Drew (1999), Vink *et al.* (2002) and Mottram *et al.* (2007) extended the use of the technique to HAeBe objects. Vink *et al.* (2002) found that 7 out of 12 HBe objects they observed have a depolarisation line effect across Hα, very similar to what was found in Be stars. As the line-effect becomes less pronounced for lower inclinations, and would disappear for a face-on disk, which is circular on the sky, the detection statistic strongly suggests that all HBe stars are surrounded by small disks with sizes of order several stellar radii. In contrast, they found a different line effect for HAe objects, where enhanced *polarisation* across the Hα was found in 9 out of 11 stars. They proposed that the line itself is intrinsically polarised since part of the emission lines originate from a compact region, where the accretion takes place. Vink *et al.* (2005a) found that HAe stars have a similar spectropolarimetric signature as the lower mass T Tauri stars with HBe stars having a different signature.

McLean (1979) reported a different line effect, across the absorption component of the emission line which is often called the McLean effect. The general idea is that the absorption blocks the unscattered light from the beam, and photons originally emitted in different directions are scattered into the line of sight, resulting in enhanced polarisation across the absorption. An alternate hypothesis was provided by Kuhn *et al.* (2007), who proposed the polarisation can be caused by selective absorption due to optical pumping of an anisotropic radiation field. In addition, Kuhn *et al.* (2011) point out that resonant line scattering, which potentially also produces line polarisation, predicts that the lines within the Ca II near-infrared triplet around 8500 Å will be differently polarised from each other. For a recent review on the use of linear spectropolarimetry, see Vink (2015).

In this chapter I aim to expand the existing spectropolarimetric work that was

mostly aimed at Hα by observing other emission lines probing different volumes and conditions than Hα. I present a spectropolarimetric study of a sample of 12 HAeBe objects. The new feature of the current study is the broad wavelength range from 4560 Å to 9480 Å, covering almost the entire optical spectrum. The chapter is organised as follows. In Section 2 I discuss the sample selection criteria, the details of the observations and data reduction. In Section 3 I present the results starting with continuum polarisation and then discussing line spectropolarimetry. The analysis is provided in Section 4. I conclude in Section 5.

2.2 Observations

2.2.1 Source Selection

Twelve objects were selected for this work from the X-shooter project of 91 HAeBe stars (Oudmaijer *et al.* 2011; Fairlamb *et al.* 2015). The main reason for choosing these, was the presence of strong emission lines which allows for a good determination of their spectropolarimetric properties. The targets were originally selected from the HAeBe catalogue of The *et al.* (1994) and candidates of Vieira *et al.* (2003). They are presented in Table 4.1, alongside their spectral type and V magnitudes. The spectral type is taken from Ababakr *et al.* (2015) and Fairlamb *et al.* (2015) while the V magnitude is taken from Vieira *et al.* (2003) and SIMBAD. The results of PDS 27 and PDS 37 have been published elsewhere in a study dedicated to these two objects, but I keep them in here (Ababakr *et al.* 2015 and Chapter 3).

Table 2.1: HAeBe Observations. The V magnitude and spectral type are listed in column 3 & 4. The spectral type is taken from Ababakr *et al.* (2015) and Fairlamb *et al.* (2015) while the V magnitude is taken from Vieira *et al.* (2003) and SIMBAD. The integration times (column 8, 9 & 10) denote the total exposures in V (4560 - 5860 Å), R (5750 - 7310 Å) and Z (7730 - 9480 Å) bands.

Name	Other name	V	Spec. type	Date			Exposure (s)		
				V	R	Z	V	R	Z
PDS 27	DW CMa	13.0	B3	04-02-12	04-02-12	04-02-12	8×340	24×50	16×120
PDS 37	Hen 3-373	13.5	B3	05-02-12	05-02-12	05-02-12	16×340	24×70	16×100
CPD-485215	Hen 3-847	10.6	B6	20-01-12	10-03-12	03-03-12	8×150	32×15	16×90
R Mon	MWC 151	11.8	B8	19-02-12	01-02-12	01-02-12	4×340	12×85	12×80
					12-10-11			12×85	
V380 Ori		10.7	A0	03-01-12	03-01-12	10-11-11	8×60	16×20	12×20
					12-10-11			12×20	
PDS 133	SPH 6	13.1	B6		21-01-12	21-01-12		16×150	8×340
BF Ori		9.7	A2		12-10-11	12-11-11		8×75	8×90
MWC 275	HD 163296	6.9	A1		01-04-12	30-03-12		32×2.5	16×7.5
GU CMa	HD 52721	6.6	B1		07-01-12	07-01-12		24×2	24×5
HD 104237	PDS 61	6.6	A7		16-01-12	16-01-12		40×1	24×5
HD 85567		8.6	B7		30-12-11	08-12-11		8×5	16×30
					30-03-12			8×5	
HD 98922	Hen 3-644	6.8	A0		30-12-11	16-01-12		40×1.5,16×1	24×5

Table 2.2: The seeing and spatial widths of the FORS2 data. The seeing was measured from the astronomical site monitor.

Name	Date			Seeing(")			FWHM(")		
	V	*R*	*Z*	*V*	*R*	*Z*	*V*	*R*	*Z*
PDS 27	04-02-12	04-02-12	04-02-12	1.2	1.2	1.4	1.0	0.9	1.0
PDS 37	05-02-12	05-02-12	05-02-12	1.3	1.1	1.1	0.8	1.0	1.0
CPD-485215	20-01-12	10-03-12	03-03-12	1.9	0.9	1.6	1.6	1.1	1.1
R Mon	19-02-12	01-02-12	01-02-12	1.0	1.1	0.9	1.2	0.9	0.8
		12-10-11			1.6			2.6	
V380 Ori	03-01-12	03-01-12	10-11-11	0.9	0.9	1.0	0.8	0.8	1.0
		12-10-11			1.5			2.8	
PDS 133		21-01-12	21-01-12		2.2	1.5		1.2	0.9
BF Ori		12-10-11	12-11-11		1.5	1.1		3.0	1.3
MWC 275		01-04-12	30-03-12		0.8	1.1		1.2	0.9
GU CMa		07-01-12	07-01-12		1.8	1.6		1.8	1.2
HD 104237		16-01-12	16-01-12		2.2	2.6		2.3	2.0
HD 85567		30-12-11	08-12-11		3	1.9		2.0	1.0
		30-03-12			1.2			1.8	
HD 98922		30-12-11	16-01-12		2.0	2.2		1.2	1.0

2.2.2 Spectropolarimetric Observations

The spectropolarimetric data for our targets were obtained with the FORS2 spectrograph mounted on ESO's VLT in Chile. Three gratings were used with a 4096×2048 pixel CCD to sample the entire optical range. The 1400V grating with central wavelength 5200 Å covered the spectral range from 4560 to 5860 Å and includes Hβ and several Fe II lines. The 1200R grating was used for the spectral range from 5750 to 7310 Å, with central wavelength 6500 Å, and includes notable lines: Hα, [O I] 6300 Å, and He I lines at 5875, 6678 and 7065 Å. Finally, the 1027Z grating covers 7730 – 9480 Å, at central wavelength 8600 Å, and this includes the calcium triplet lines and the hydrogen Paschen series. A 0.5 arcsec slit was used in all cases, which resulted in a spectral resolution of R = 3800, 4800, 4800 in the *V*, *R* and *Z* bands respectively. The dates and the exposure times in each band are given in Table 4.1. The seeing and spatial widths of the

data are summarised in Table 2.2.

FORS2 is equipped with an optical polarimeter in order to analyse the linearly polarised components. The polarisation optics consist of a rotating half-wave plate and a calcite block. The calcite block separates the incoming light into two perpendicularly polarised light beams, the ordinary (O) and extraordinary (E) beam. The half-wave plate is rotated to measure polarisation at four different angles: 0°, 45°, 22.5°, and 67.5°. One complete set of observations consists of four exposures, one at each of the four angles. Several cycles of observation at the above angles were taken for each object to check for the consistency of the polarisation and its features. Polarised and unpolarised standard stars were observed throughout the night. The exposure times for these were much shorter as it was only the continuum values that were of interest.

Spectropolarimetry is a photon-hungry method. Typical line effects are of order 0.5% and to properly sample the polarisation behaviour as a function of wavelength, a polarisation precision of order 0.1% per pixel is therefore required. This corresponds to signal-to-noise ratios of order 1000. Long exposure times were used for faint objects and several short exposure times for objects with strong Hα lines in order to avoid saturation of the CCD.

2.2.3 Data Reduction

The spectropolarimetric data reduction was carried out using GASGANO and FORS pipeline v4.9.18. Two recipes were used: one dedicated to the calibration and the other to extract the science spectrum. The reduction procedure consists of bias subtraction, flat fielding, sky subtraction, extraction and wavelength cal-

ibration of the O and E spectra. The Stokes parameters, obtained from the O and E beams, lead to the percentage of linear polarisation, P, and polarisation angle, θ, according to the following equations:

$$P = \sqrt{Q^2 + U^2} \tag{2.1}$$

$$\theta = \frac{1}{2} \arctan\left(\frac{U}{Q}\right) \tag{2.2}$$

For the analysis purposes, the data were imported into the IRAF (Tody 1993) and POLMAP package (Harries 1996) maintained by Starlink.

FORS2 is mounted on the UT1 Cassegrain focus, resulting in a relatively stable instrumental polarisation. To improve signal-to-noise and the polarisation accuracy, the individual data sets were combined. Four polarised and three zero polarised standard stars were selected from the sample of Fossati *et al.* (2007) for the purpose of polarimetric calibrations. The instrumental polarisation is found to be $\sim$0.16%, from the observation of unpolarised standard stars. The angle offset is found to be 0.5° from the observation of polarised standard stars. In order to clearly visualise the line effect, the change in polarisation across the lines, the polarisation spectra are rebinned to a constant polarisation error per bin. I performed the rebinning of the spectra very carefully to avoid losing the line effect signature. I did not correct the data for the instrumental and interstellar polarisation. Because these two only add a wavelength independent vector to the observed Q and U parameters whereas our main aim in this work is the detection of polarimetric change across the lines. However, as the polarisation is a vector quantity, the interstellar polarisation could flip the polarisation signature across

the line (see e.g. Oudmaijer *et al.* 1998 in HD 87643). Therefore, careful analysis is needed to characterise the line effect.

2.3 Results

2.3.1 The Optical Spectrum

In the optical range from 4560 Å to 9480 Å, the spectra show numerous spectral lines in emission and absorption. The entire spectrum of PDS 27 is presented in Fig. 2.1 to show the range of the observed spectra and the identified spectral lines.

The Hα lines are the strongest with line peak to continuum ratios ranging from ~ 2 to ~ 20. In all targets, Hα is in emission, as shown in Fig. 2.2. The Hα lines exhibit various different profiles. These include pure emission lines, double peaked emission with central absorption through to P Cygni profiles. GU CMa, CPD-485215 and V380 Ori display a pure emission line, R Mon and BF Ori show a double peaked emission line with central absorption. The remaining seven objects display P Cygni profiles, for two of which Hβ data are also available. For both spectra that contain Hβ, the absorption component in Hβ is deeper than in Hα. In addition to Balmer series, weak Paschen lines are also seen in emission for most objects.

The Ca II triplet lines at 8498, 8542 and 8662 Å are observed in all objects apart from GU CMa and CPD-485215. They are all in emission apart from BF Ori where they are in absorption. The line to continuum ratio is in the range 1.5 to 10.5. The Ca II doublet at 8912 and 8927 Å is present in all objects apart from

GU CMa, MWC 275 and CPD-485215. The lines are in emission in all objects apart from HD 104237 and BF Ori where the lines are in absorption.

Three He I lines at 5876, 6678 and 7065 Å are observed in all objects. The lines are in absorption in six objects including PDS 27, PDS 37, R Mon, HD 85567, GU CMa and BF Ori. PDS 133, HD 104237, V380 Ori and HD 98922 have the lines in emission. Inverse P Cygni profiles, weak emission and strong absorption He I lines are detected in the spectra of MWC 275 and CPD-485215 and indicate infalling material.

Several forbidden [Fe II] at 4814, 5158, 5262, 5333, 7155 and 8616 Å lines are observed in the spectra of R Mon and CPD-485215. [S II] at 6716 and 6730 Å is also seen in the spectra of R Mon. In addition, strong [O I] at 6300, 6364 Å is present in the spectra of R Mon, CPD-485215 and PDS 133. However, [O I] lines are either absent or very weak in the spectra of the remainder of the targets. Unlike the cases of R Mon and CPD-485215, the [O I] lines in the spectra of PDS 133 are broad and double peaked which may suggest that the forbidden lines emerge from a rotating disk. This has been suggested before for HAeBe stars (Acke *et al.* 2005), although the broad line could also indicate a disk-wind (see e.g. Ignace & Brimeyer 2006).

In summary, many strong emission lines are observed which allows us to investigate spectropolarimetric line effects which had never been studied before for most of these lines.

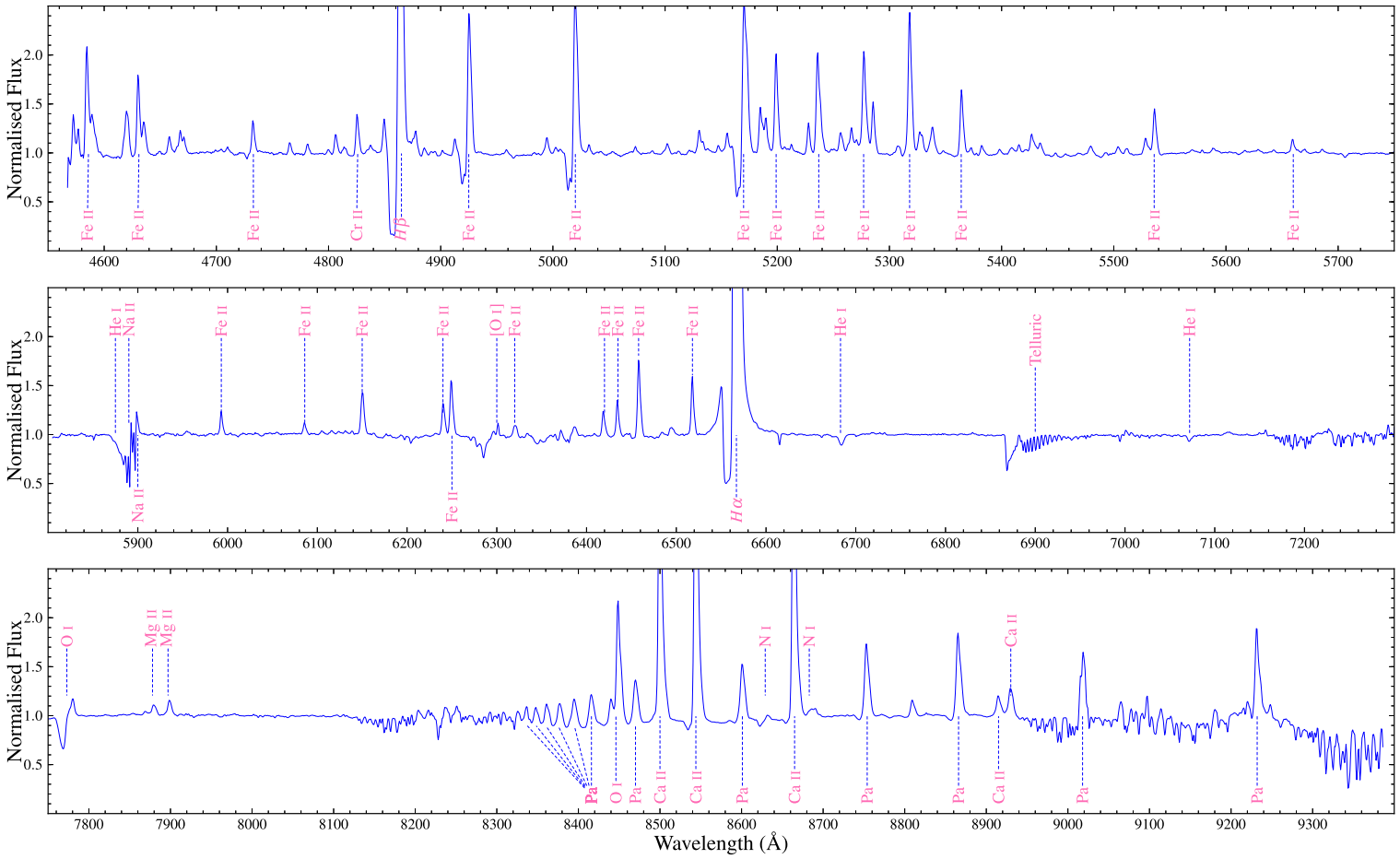

Figure 2.1: Normalised flux versus wavelength (Å) spectra of PDS 27 in the range from 4560 Å to 9480 Å, the observed spectral lines are identified.

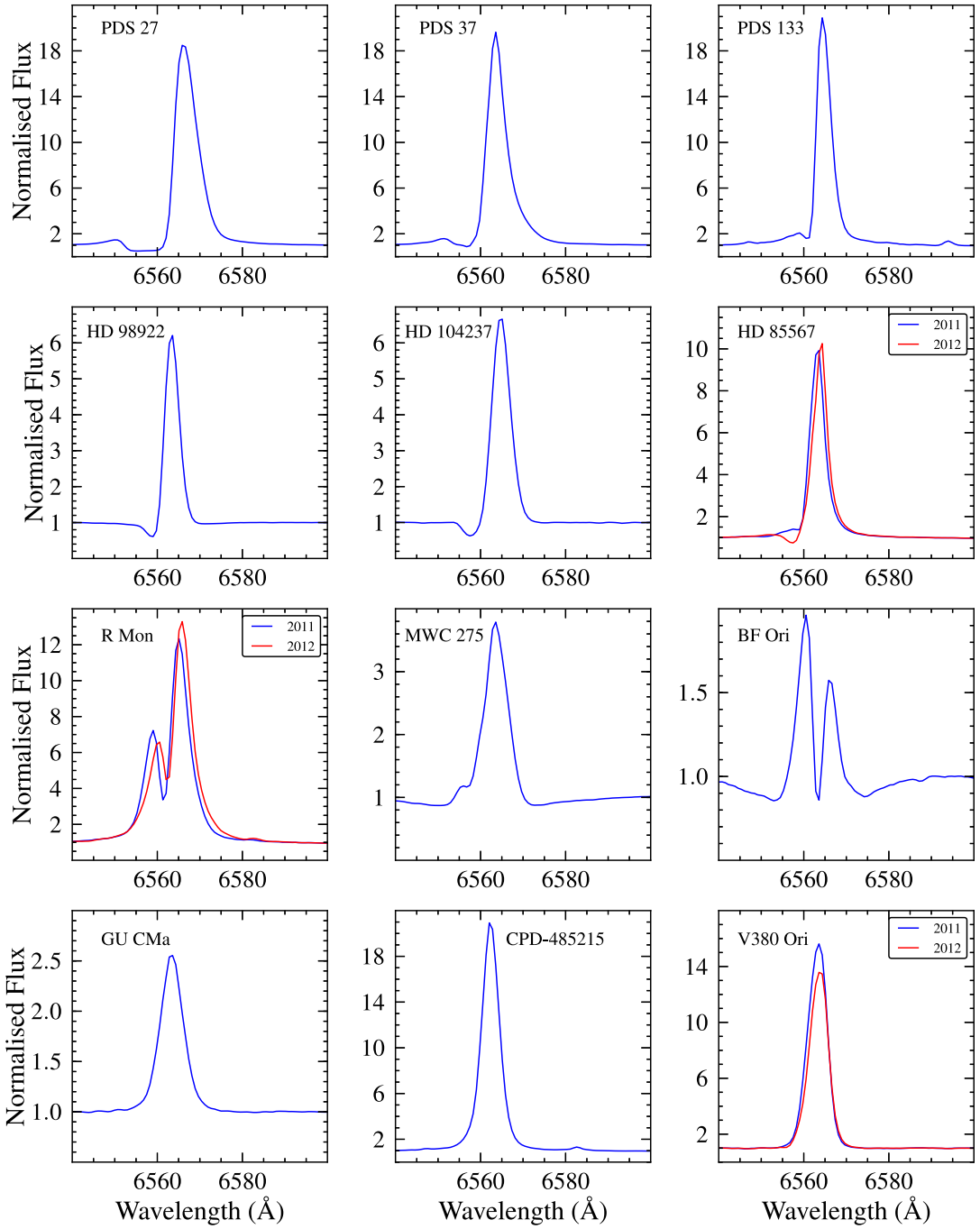

Figure 2.2: The Hα line profiles, the spectra are normalised to one. The spectra of HD 85567, R Mon and V380 Ori are presented for two observation epochs: 2011 (blue solid line) and 2012 (blue solid line).

Table 2.3: The continuum polarisation of the targets measured in the following wavelength regions: B band centred at 4700 Å; V band centred at 5500 Å; R band centred at 7000 Å; I band centred at 9000 Å. The polarisation was measured over a wavelength range of 250 Å either side of the central wavelength, except for the B band where it was 125 Å either side. All the errors are differential, where the instrumental error is ∼0.16% in polarisation and ∼ 0.5° in angle (see text in Section 2.3 for details).

Object	B		V		R		I	
	$P_{cont}(\%)$	θ°_{cont}	$P_{cont}(\%)$	θ°_{cont}	$P_{cont}(\%)$	θ°_{cont}	$P_{cont}(\%)$	θ°_{cont}
PDS 27	8.60 ± 0.03	18.60 ± 0.10	9.00 ± 0.01	18.90 ± 0.01	8.80 ± 0.01	18.40 ± 0.04	7.50 ± 0.01	18.10 ± 0.03
PDS 37	4.70 ± 0.04	130.00 ± 0.30	5.10 ± 0.01	130.80 ± 0.01	5.20 ± 0.01	130.00 ± 0.06	4.40 ± 0.01	133.40 ± 0.05
CPD-485215	1.25 ± 0.01	19.30 ± 0.30	1.30 ± 0.01	15.30 ± 0.06	1.70 ± 0.01	9.50 ± 0.20	1.90 ± 0.01	6.70 ± 0.20
R Mon	11.20 ± 0.04	80.60 ± 0.10	11.20 ± 0.02	80.00 ± 0.05	12.15 ± 0.01	67.70 ± 0.04	12.10 ± 0.01	60.15 ± 0.03
					8.10 ± 0.02	69.40 ± 0.07		
V380 Ori	0.60 ± 0.01	90.80 ± 0.70	0.70 ± 0.01	93.20 ± 0.30	0.70 ± 0.01	98.40 ± 0.06	0.10 ± 0.01	124.00 ± 3.00
V380 Ori					0.70 ± 0.02	95.15 ± 1.00		
PDS 133					2.30 ± 0.04	37.70 ± 0.50	2.10 ± 0.03	38.30 ± 0.05
BF Ori					0.70 ± 0.01	44.00 ± 0.06		
MWC 275					0.70 ± 0.01	1.60 ± 0.20	0.67 ± 0.01	14.84 ± 0.28
GU CMa					1.60 ± 0.01	14.60 ± 0.01	1.40 ± 0.01	14.45 ± 0.09
HD 104237					0.35 ± 0.01	174.60 ± 0.60	0.58 ± 0.01	182.89 ± 0.35
HD 85567					0.38 ± 0.01	133.90 ± 0.60	0.23 ± 0.01	154.02 ± 0.61
					0.26 ± 0.02	134.50 ± 2.10		
HD 98922					0.40 ± 0.01	174.90 ± 0.30	0.58 ± 0.01	177.90 ± 0.30

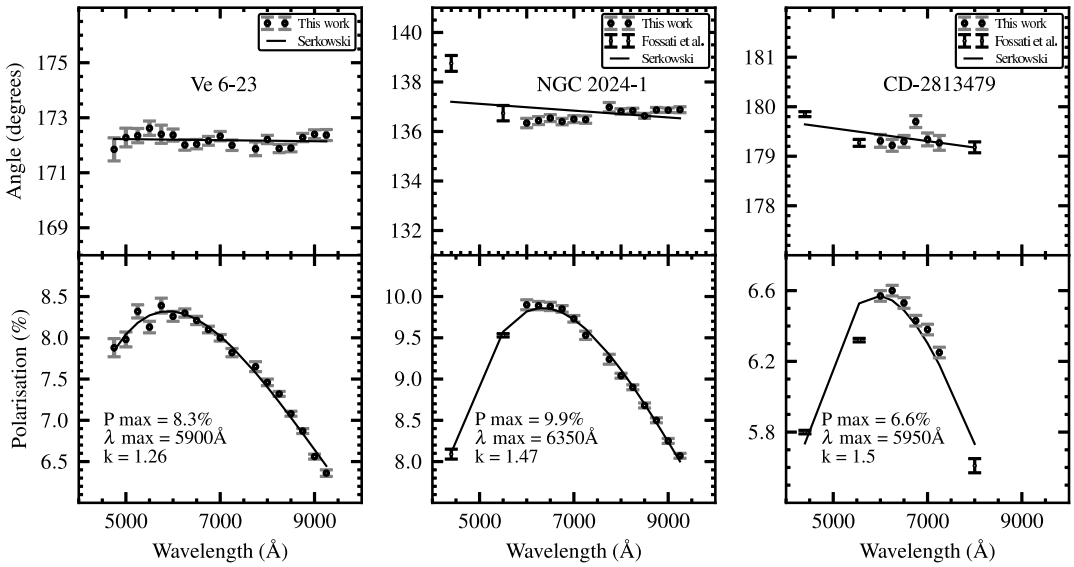

Figure 2.3: The polarisation and polarisation angles as a function of wavelength for the polarised standard stars. The data for this work are presented in black solid circles and were coarsely sampled to improve the error bars. The data in B and V for NGC 2024-1, and in B, V and I (black dots) are taken from Fossati *et al.* (2007). The black lines denote the best-fitting Serkowski law to the data.

2.3.2 Continuum Polarisation

The continuum polarisation is measured for the entire spectrum and the results for the polarimetric standard stars are shown in Fig. 2.3, while those for the HAeBe stars are plotted in Fig. 2.4. The data are rebinned using a coarse sampling of $\sim$ 250 Å per bin, to minimise errors.

Typically, the observed continuum polarisation is a vector addition of the interstellar polarisation and the intrinsic polarisation which is due to scattering of star light by circumstellar dust and free electrons. The interstellar polarisation is caused by dichroic absorption of aligned dust grains. Its wavelength dependence is well understood and explained by Serkowski *et al.* (1975). They found that the

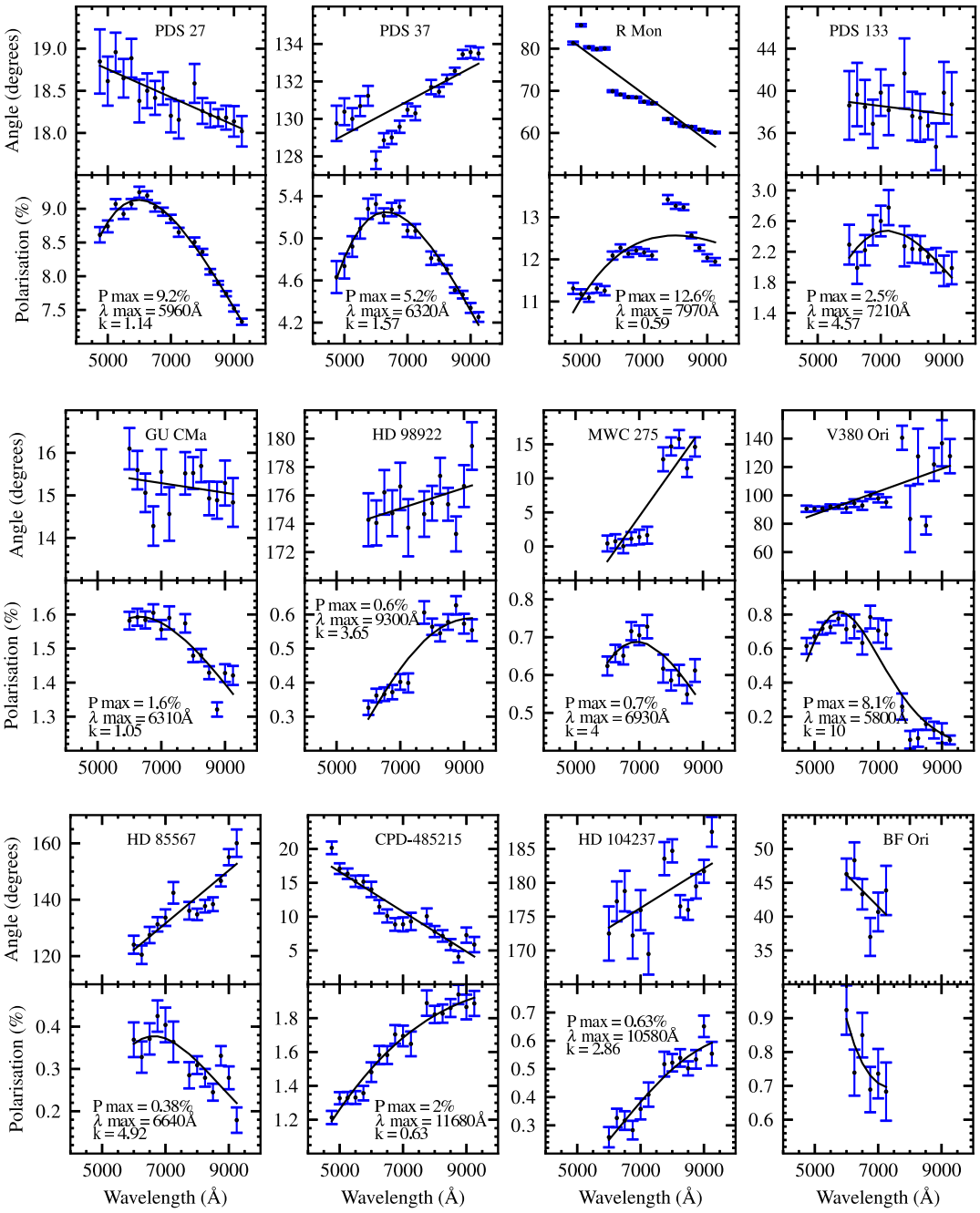

Figure 2.4: As the previous figure, but now for the HAeBe stars. The polarisation is shown in the lower panel while the polarisation angle is shown in the upper panel. The black lines denote the best fitting Serkowski law to the data.

linear polarisation follows an empirical curve according to the following equation:

$$\frac{P(\lambda)}{P_{max}} = \exp\left[- k \ln^2\left(\frac{\lambda_{max}}{\lambda}\right)\right] \tag{2.3}$$

where λ_{max} is the wavelength where the polarisation is at its maximum value, P_{max}, and k is the width of the empirical curve. Typically, the polarisation peaks in the visual band at $\sim$ 5500 Å, but can be in the range of 4500-8000 Å. k was initially taken to be a constant value of $k = 1.15$. However, it has been found that the value of k depends on the value of λ_{max}, and is sensitive to the size distribution of the dust particles (Whittet *et al.* 1992). In order to assess whether the observed polarisation may have an interstellar dust component, I fit the Serkowski law (Equation 3) to our targets and polarised standard stars. λ_{max}, P_{max} and k are taken as a free parameters. The Serkowski law provides - as expected - an excellent fit to the polarised standard stars as shown in Fig. 2.3. The figure also shows that the polarisation angle remains constant over different bands.

The best fit to our targets is provided in Fig. 2.4. The stars generally follow the Serkowski law but not as well as the standard stars. In some objects, the polarisation spectra peak at much longer wavelengths than the V band while, in addition, the polarisation angle changes over different bands in all objects. This overall behaviour would suggest that a fraction of the observed polarisation is due to interstellar dust, but that an intrinsic contribution is present. This is also consistent with the polarisation angle. For all objects, the observed polarisation angle changes over different bands, indicating the presence of intrinsic polarisation. The deviation of the angle ranges from 1° to 30° (see Fig.2.4). The polarised

standards did not show a significant deviation in the observed polarisation angles.

I note that the continuum polarisation and the polarisation angle jump from one setting to another for some objects (see Fig.2.4). This is particularly striking in PDS 37, R Mon and MWC 275. This might be because the objects are extended, and that a slightly different positioning of the slit could result in slightly different polarisation to be measured, which I shall discuss later.

To facilitate comparison with past and future observations, I measured the continuum polarisation at the B, V, R and I bands and the results are summarised in Table 2.3. The linear continuum polarisation ranges from $\sim$0.3 % in the very low polarised star HD 85567 to $\sim$12 % in the highly polarised star R Mon. The data of two epochs are provided for three objects, R Mon, V380 Ori and HD 85567. R Mon shows a strong variability of order of $\sim$4 % in the R band between these two epochs. V380 Ori shows similar polarisation values and HD 85567 shows a little variation. The literature values for the objects are summarised in Table 4.4. The polarised standard stars are consistent with the literature values. The HAeBe stars are broadly consistent with the previous measurements, but there is some variation in the polarisation data.

The polarisation variability in the degree of polarisation and/or polarisation angle is a common phenomenon among HAeBe objects (Grinin 1994; Jain & Bhatt 1995). Its origin is thought to be caused by the intrinsic polarisation over time as the interstellar polarisation is unlikely to be variable over a short period of time.

Table 2.4: Previous measured continuum polarisation. Column 2 gives the band at which the polarisation was measured. Columns 3 and 4 list the measured polarisation percentage and polarisation angle. The references are presented in the last column.

Object	Band	$P_{cont}(\%)$	θ°_{cont}	Ref.
PDS 37	V	3.253 ± 0.104	120.1 ± 1.0	1
CPD-485215	V	0.348 ± 0.035	20.7 ±3.0	1
R Mon	V	12.0 ± 1.2	91 ± 3	2
	U	11.1 ± 0.7	85.7 ± 1.8	3
	B	11.1 ± 0.4	86.6 ± 1.1	3
	V	12.3 ± 0.5	89.4 ± 1.2	3
	R	12.6 ± 0.3	83.5 ± 0.8	3
	I	12.1 ± 0.4	94.5 ± 0.9	3
V380 Ori	V	0.98 ± 0.10	86 ± 3	2
	R	1.26 ± 0.01	96 ± 1	4
	U	0.08 ± 0.16	151 ± 57	3
	B	0.80 ± 0.06	88.8 ± 2.1	3
	V	0.98 ± 0.06	86.2 ± 1.8	3
	R	1.31 ± 0.14	74.4 ± 3.2	3
	I	1.25 ± 0.18	84.9 ± 4.2	3
BF Ori	R	0.6 ± 0.1	58 ± 1	5
	R	0.886 ± 0.017	52.0 ± 0.6	6
	V	0.46 ± 0.01		7
GU CMa	R	1.15 ± 0.01	19 ± 1	4
	R	0.8 ± 0.1	24 ± 1	5
	R	1.726 ± 0.006	27.0 ± 0.1	6
HD 104237	V	0.032 ± 0.063	167.2 ±56.5	1
HD 85567	V	0.478 ± 0.035	105.7 ± 2.0	1
HD 98922	U	0.515 ± 0.087	152.8 ± 5.0	8
	B	0.201 ± 0.070	168.4 ± 14.1	8
	V	0.235 ± 0.051	160.5 ± 6.0	8
MWC 275	V	0.417 ± 0.035	36.0 ± 2.5	1
	V	0.225 ± 0.012	29.8 ± 1.6	8
	R	0.284 ± 0.014	35.5 ± 1.5	8
	I	0.351 ± 0.018	38.3 ± 1.5	8
	V	0.02 ± 0.01		7

References. 1:Rodrigues *et al.* (2009), the errors on the polarisation angle for this reference are calculated from 0.5 × arctan ($\sigma p/P$); 2:Hillenbrand *et al.* (1992); 3:Vrba *et al.* (1979); 4:Oudmaijer & Drew (1999); 5:Wheelwright *et al.* (2011a); 6:Vink *et al.* (2005a); 7:Oudmaijer *et al.* (2001); 8:Yudin & Evans (1998), I calculated the average values for MWC 275, taken on the same day.

2.3.3 Line Spectropolarimetry

Most of the previous spectropolarimetric studies have been performed on the strong Hα emission lines. However, the advantage of this study is that the long spectral coverage allows us to perform linear spectropolarimetry on lines that had never been studied in this manner before. I begin by discussing the results of the strongest hydrogen recombination lines before discussing other lines.

2.3.3.1 Hydrogen Recombination Lines

Spectropolarimetry was performed on all hydrogen lines including Hα, Hβ and the Paschen lines. The spectropolarimetric data around Hα are shown in a so-called "triplot" in the upper half of Fig. 2.5. In this triplot, the Stokes I (normal intensity) is shown in the lower panel, the polarisation percentage in the middle, while the position angle (PA) is shown in the upper panel. The results are also represented in a Stokes (*Q, U)* diagram (bottom) in Fig. 2.5 using the same wavelength range of the triplot spectra, but sometimes with a different binning. Ten out of the twelve objects display a clear line effect across Hα while the remaining two, BF Ori and HD 104237, show a potential line effect. The observed line effects across Hα are of order of $\sim$0.2 % to $\sim$7 % in the case of R Mon. The change in polarisation occurs across the emission lines, the absorption components or the entire line profiles.

The spectropolarimetric properties of Hα for each target are listed in Table 2.5. Columns 3, 4 & 5 list the spectroscopic characterisation of Stokes I, the intensity spectrum. Generally, the lines are stronger in HBe objects than in HAe objects. The final three columns represent the line polarimetric properties, i.e.

the depolarisation, line polarisation and McLean effects as introduced in Sec. 1.

The intrinsic polarisation angle is measured from the slope of the loop of the line in the (*Q, U)* diagram following Wheelwright *et al.* (2011a). From the analysis of the (*Q, U)* diagram, the direction of intrinsic polarisation on the sky can be determined. I have measured the intrinsic polarisation from the slope of the loop across the line in the (*Q, U)* diagram of Fig. 2.5. This gives two different results depending on the type of the line effect. In the case of line depolarisation, the intrinsic angle is measured from the line to continuum while for line polarisation it is measured from continuum to the line resulting in a 90° difference from the former. This 90° difference in polarisation is equivalent to 180° on the sky, for that reason the direction of the vector in the (*Q, U)* diagram is crucial, and this depends on the observed type of polarisation. For the objects displaying the McLean effect, the angle is measured from the continuum to the line.

The data for the next strongest hydrogen recombination line, Hβ, is available for five objects. Two of these, R Mon and CPD-485215, show a clear change in polarisation across this line and the results are presented in Fig. 2.6. The Paschen lines are much weaker than the Balmer series and only R Mon shows a line effect across these lines.

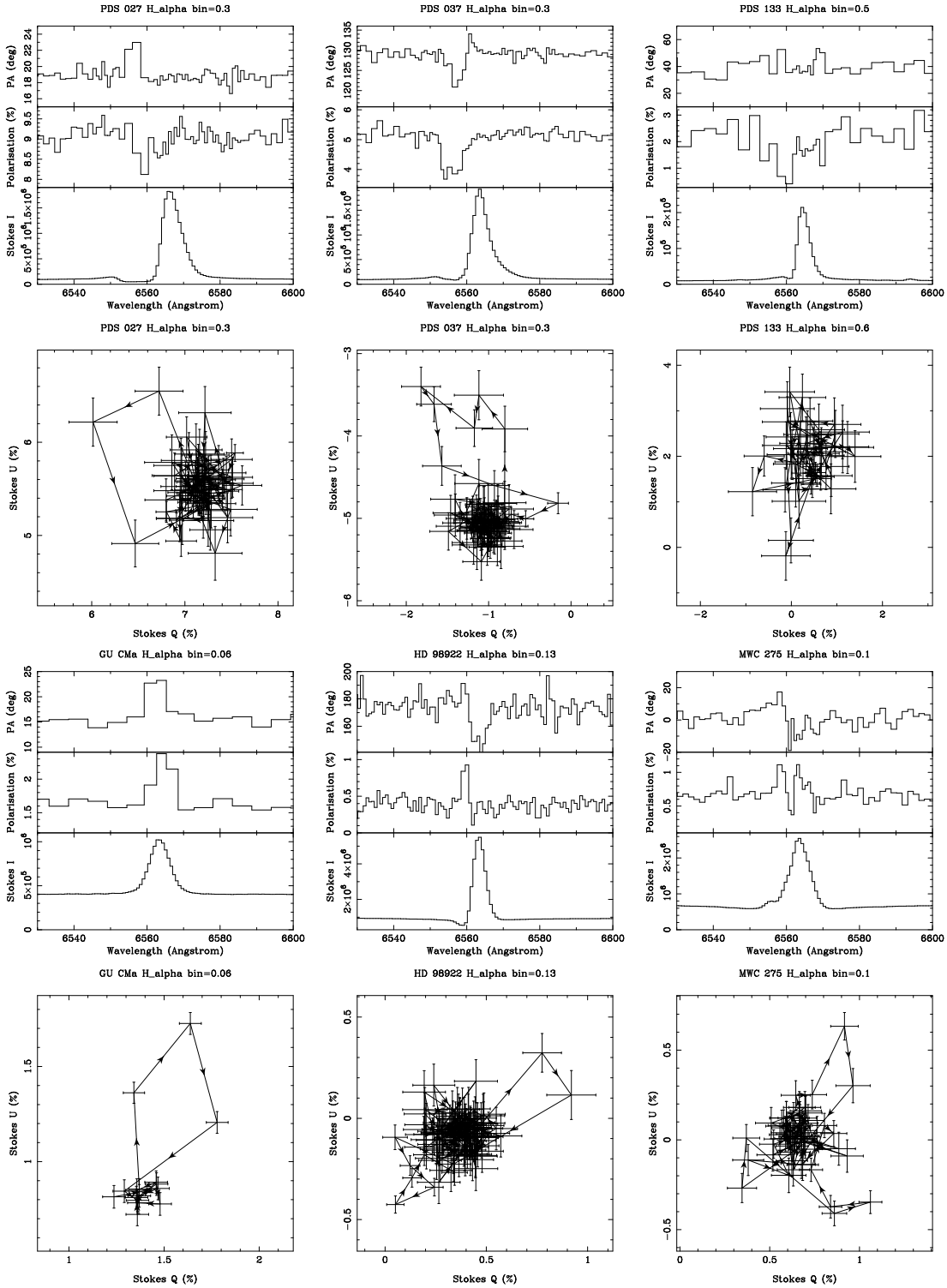

Figure 2.5: Hα spectropolarimetry of the stars. The data are presented as a combination of triplots (top) and (*Q, U)* diagrams (bottom). In the triplot polarisation spectra, the Stokes intensity (I) is shown in the bottom panel, polarisation (%) in the centre, while the position angle (PA) is shown in the upper panel. The Q and U Stokes parameters are plotted against each other below each triplot. The data are rebinned to a constant error in polarisation, which is indicated at the top of each plot. The arrows in the (*Q, U)* diagrams indicate the polarisation moves in and out of the line effect from blue to red wavelengths.

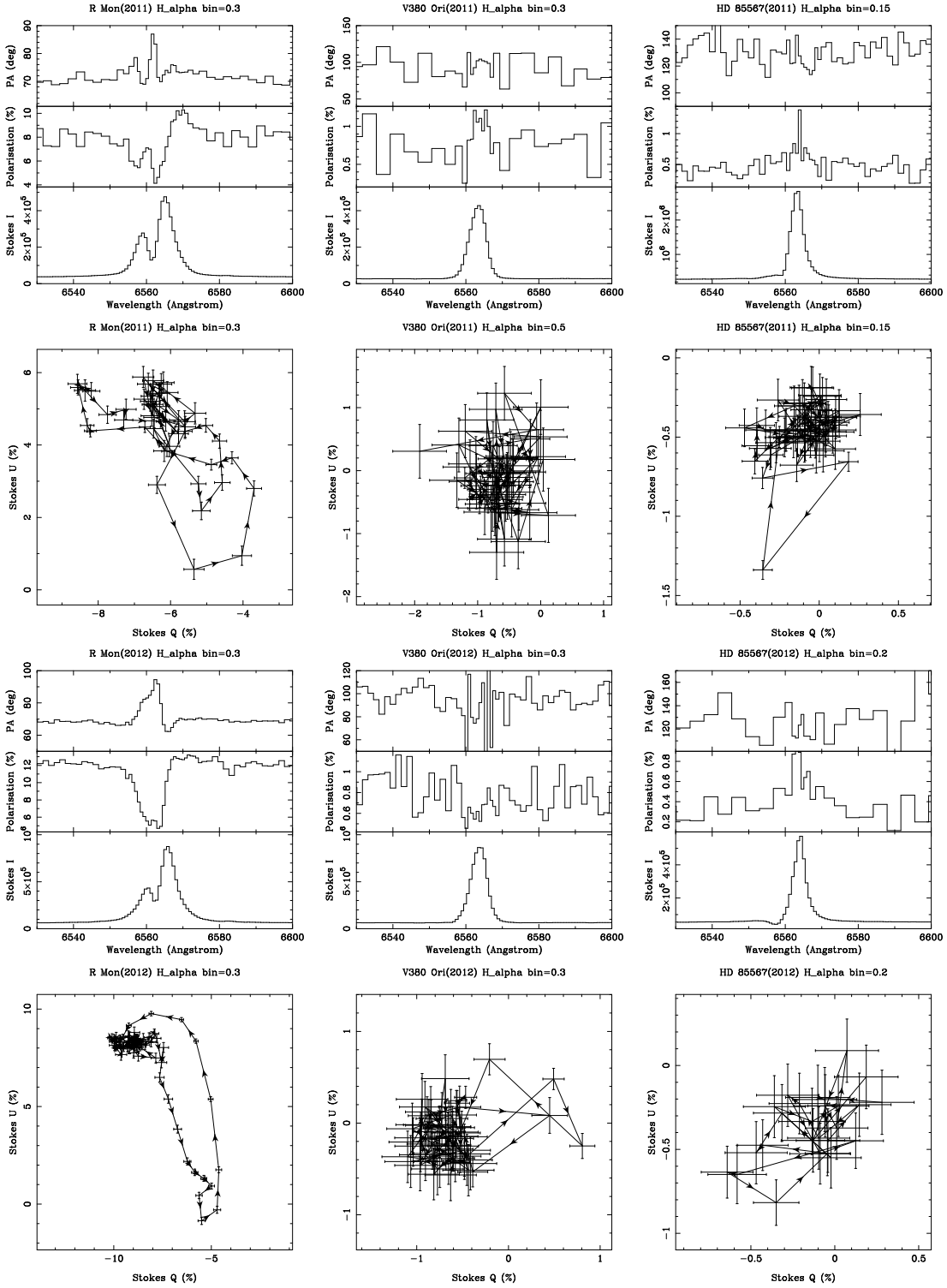

Figure 2.5: continued

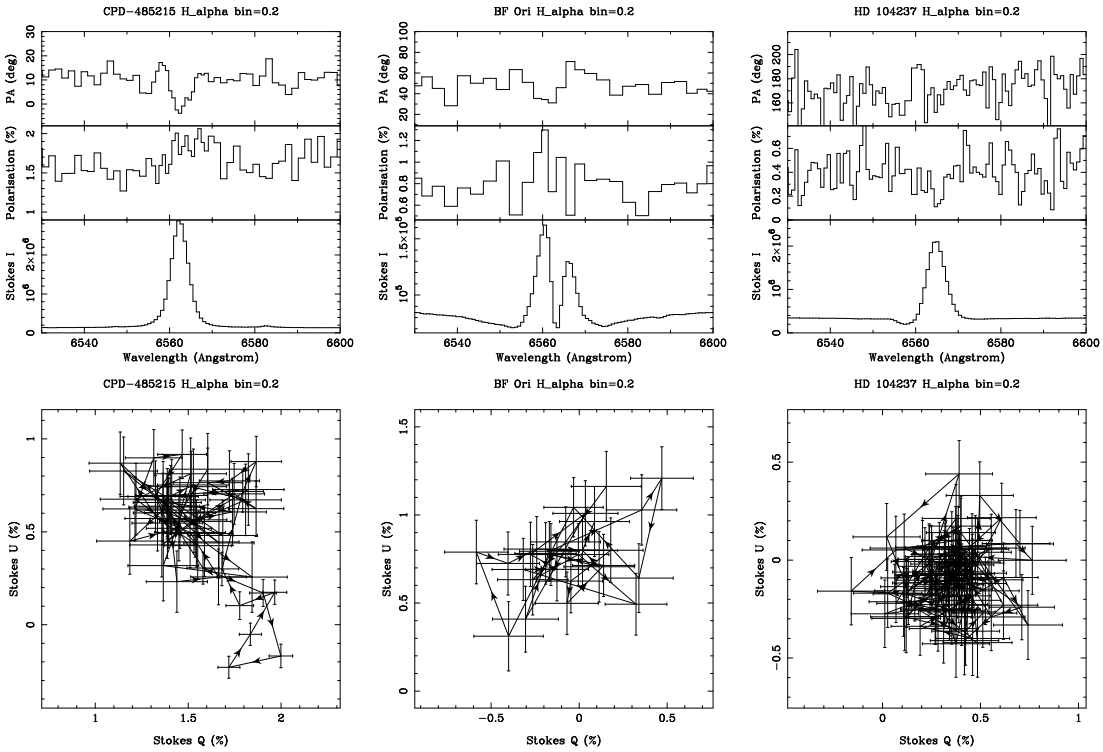

Figure 2.5: continued

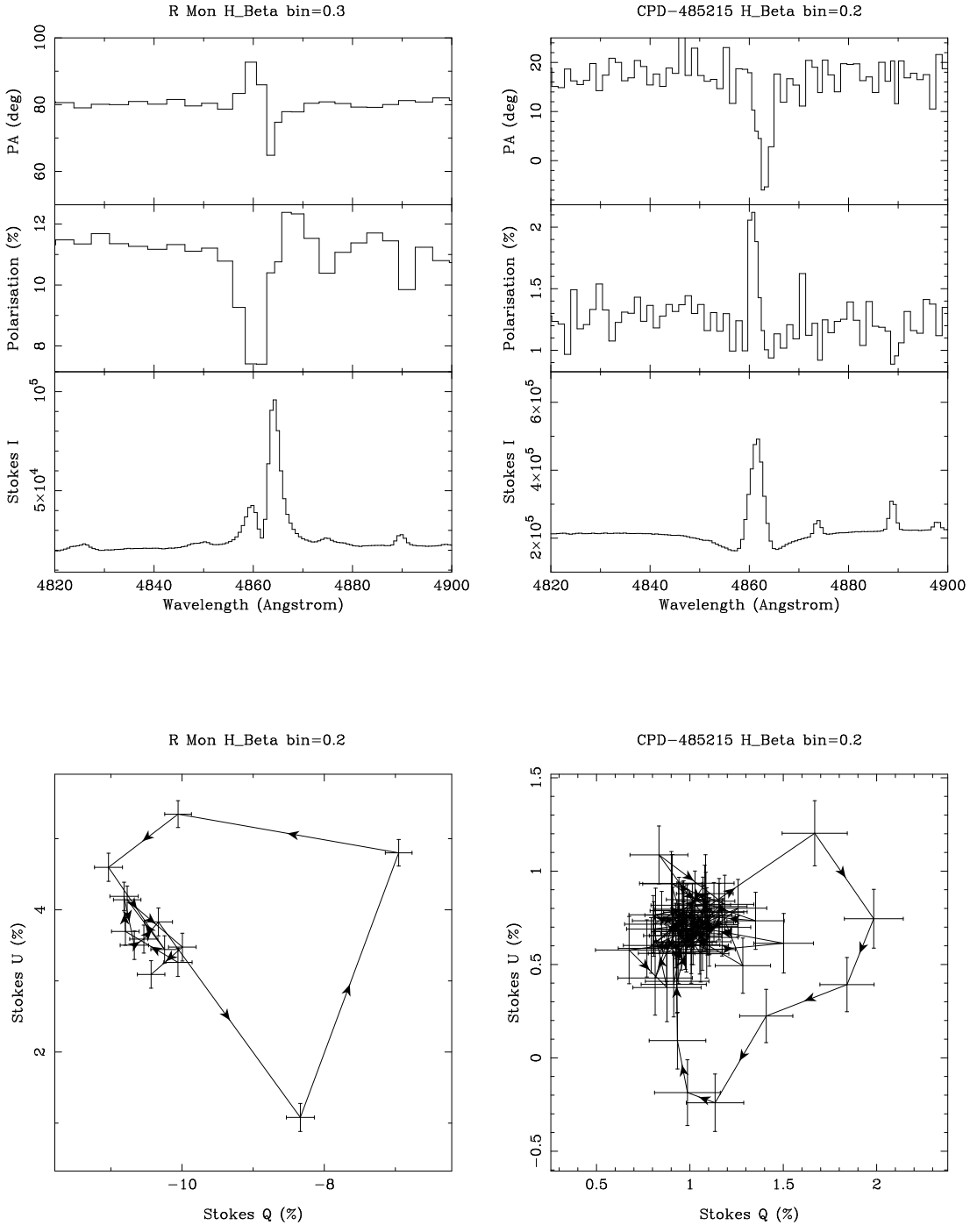

Figure 2.6: Hβ spectropolarimetry of R Mon and CPD-485215. See the caption of Fig. 2.5 for more details.

Table 2.5: The Hα line results: columns (3), (4) and (5) list the Stokes (I) characteristics; columns (6), (7) and (8) list line spectropolarimetry characteristics of each target. Column (8) provides an estimation of the intrinsic polarisation PA derived from line excursions in the (*Q, U)* diagram (see text for details). Errors in the EW measurements are typically 5%, the uncertainty in intrinsic polarisation angle is approximately 10°.

Object	Spec. type	line profile	EW (Å)	Line/cont.	Line effect(σ level)	Classification	θ°_{intr}
PDS 27	B3	P Cygni	-120.8	18.0	4.5σ	M	77
PDS 37	B3	P Cygni	-122.6	19.4	6.0σ	M	56
PDS 133	B6	P Cygni	-94.5	20.7	3.5σ	M	126
HD 98922	A0	P Cygni	-17.9	6.0	4.0σ	D/M	22
R Mon(2011)	B8	Double-peaked	-98.6	12.6	15.0σ		
R Mon(2012)		Double-peaked	-105.5	12.9	32.5σ		
GU CMa	B1	Pure emission	-11.1	2.6	15.5σ	D	127
CPD-485215	B6	Pure emission	-100.8	19.6	4.5σ	D	62
MWC 275	A1	P Cygni	-14.9	3.8	6.5σ	P	112
HD 85567(2011)	B7	P Cygni	-43.5	9.9	6.0σ	D	31
HD 85567(2012)		P Cygni	-42.1	10.2	2.5σ		
V380 Ori(2011)	A0	Pure emission	-82.7	15.5	No		
V380 Ori(2012)		Pure emission	-71.1	13.6	4.5σ	P	10
HD 104237	A7	P Cygni	-27.2	6.5	2.0σ		
BF Ori	A2	Double-peaked	1.0	1.9	3.0σ		

D: Depolarisation, P: Polarisation, M: McLean

2.3.3.2 Ca II Lines

The Ca II triplet at 8498, 8542 and 8662 Å originates at larger distances from the central star than Hα because of its lower ionisation energy. Only two objects out of twelve, show a change in polarisation across these lines. MWC 275, as shown in Fig. 2.7, displays a clear change across these lines. The change is as broad as the emission lines and is clear in both polarisation and polarisation angle. R Mon also shows a change in polarisation across these lines (see Fig. 2.17). PDS 37 shows a possible line effect in only the first two datasets while the second two datasets do not show such a line effect (Ababakr *et al.* 2015 and Chapter 3). Therefore, the line effect in PDS 37 is not a conclusive result based on the current data. The Ca II doublet at 8912 and 8927 Å is also seen in the spectra of most objects. R Mon is the only object that shows a line effect across the Ca II doublet.

2.3.3.3 He I Lines

The He I lines trace the very inner hot circumstellar environment as they have a very high excitation energy. Three He I lines at 5876, 6678 and 7065 Å are seen in the spectra of all objects. These lines do not show any signs of a line effect. In most objects the lines are in absorption however, while those in emission are very weak, possibly too weak to show the line effect.

2.3.3.4 Forbidden Lines

Most objects have forbidden emission lines, however line effects across them are limited to a few objects. All the [Fe II] lines show a depolarisation in R Mon

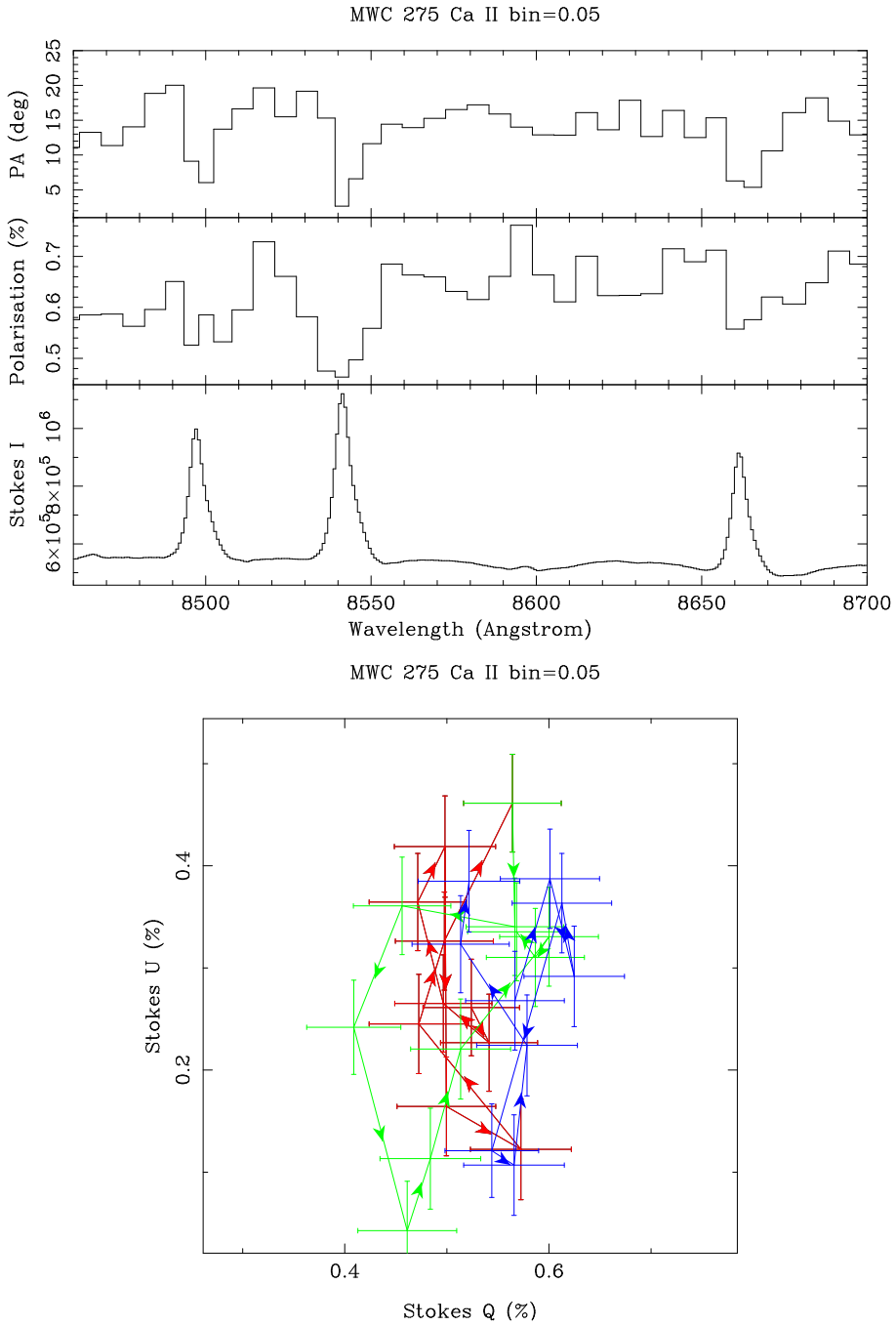

Figure 2.7: Ca II triplet polarisation data of MWC 275. In the (*Q, U)* diagram, the lines at 8498, 8542 and 8662 Å are plotted in red, green and blue solid lines. See the caption of Fig. 2.5 for more details.

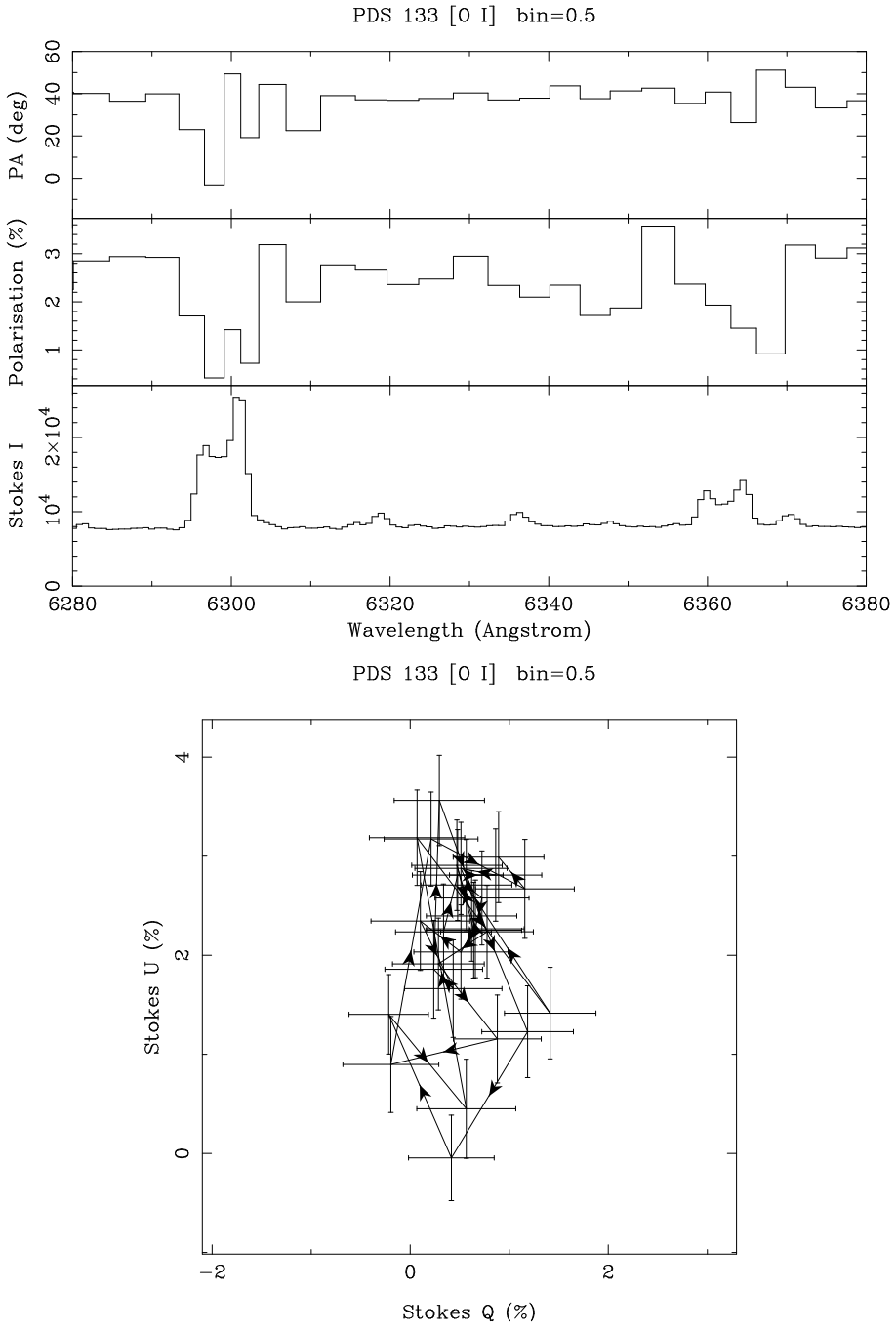

Figure 2.8: [O I] at 6300 and 6364 Å polarisation data of PDS 133. See the caption of Fig. 2.5 for more details.

and CPD-485215. Both [S II] display a clear depolarisation in the spectra of R Mon. [O I] lines also display a clear depolarisation in R Mon, CPD-485215 and PDS 133. However, the lines are broad and double peaked in PDS 133. The polarisation spectra of PDS 133 across [O I] at 6300 Å is presented in Fig. 2.8 and the remainder of the polarisation spectra of all forbidden lines are presented in Fig. 2.17.

2.3.3.5 O I and Fe II Lines

Two O I lines at 7773 and 8446 Å are observable. R Mon and CPD-485215 show a clear change in polarisation across these lines. Several Fe II lines are observable in the spectra of all objects. However, only R Mon shows the line effect across these lines. The polarisation spectra can be seen in Fig. 2.17.

2.3.3.6 Summary on the Occurrence of the Line Effect

I presented spectropolarimetry from ∼4500 to 9000 Å of a sample of HAeBe stars that were previously known to have a line effect across the Hα line. I find that this phenomenon is very rare across lines other than Hα. Strong emission lines such as Hβ and the CaII near-infrared triplet are only seen with a line effect in just a few sources. It should perhaps be noted here that the detection does not necessarily depend on the line strength. For example, lines such as Hβ and even Hγ in the Be star ζ Tau have line effects of order 1%, while the lines themselves hardly reach above the continuum (see the review by Oudmaijer 2007 and Chapter 4). The fact that strong lines do not exhibit a line effect is thus a very strong observational finding. Finally, R Mon appears to be an exceptional object in the sense that it is the only star in our sample that has a polarisation effect in most

of its emission lines. I will return to this object later in the following discussion.

2.4 Analysis

The spectropolarimetric results of the sample show a continuum polarisation at the level between ∼0.3 % to ∼12 %. Unlike the polarised standard stars, the majority of objects do not follow the empirical curve of the Serkowski law. A line effect is present across the Hα line in all objects.

Three different line effects are observed across the Hα line in the sample (see Table 2.5): depolarisation, intrinsic polarisation; and a polarisation change across the absorption, which is commonly referred to as the McLean effect. In depolarisation, the polarisation across the emission line decreases compared to the continuum, and it is more common in high mass stars (Clarke & McLean 1974; Poeckert & Marlborough 1976). Intrinsic line polarisation can be due to an anisotropic line emitting region scattering off circumstellar material, and it was found in T Tauri and HAe stars (Vink *et al.* 2002, 2003, 2005a). The McLean effect is where the absorption component of the emission line often has a different polarisation than the continuum, but the emission has not (McLean 1979). There is a distinct difference in polarimetric properties between the HBe stars, showing de-polarisation and the HAe stars showing enhanced polarisation across the line.

The intrinsic line polarisation is thought to be caused by the effects of magnetospheric accretion. In this case, disk material is funnelled through accretion columns on to the stars. The material shocks the photosphere where it crashes into at high speeds. The line emission coming from these hot spots will be polarised as they scatter off the disk material, which becomes detectable as a line

effect (Vink *et al.* 2005b).

2.4.1 McLean Effect

A number of objects display a polarisation change across the P Cygni absorption of the hydrogen lines and do not necessarily fit into the categories above. For illustration, the formation of P Cygni profile is schematically shown in Fig. 2.9.

The concept of the McLean effect is based on the fact that the wind material in our line of sight blocks the unscattered light and removes it from the beam. This leads to observation of a strong emission line with a blueshifted absorption component. However, the flux in the absorption does not reach zero because the re-emission process is isotropic; some of the photons will be scattered into our line of sight. If the distribution of the scattering material is aspherical, the observed light across the absorption will be more polarised than the continuum light. PDS 27, PDS 37 and PDS 133 show a clear McLean effect across the absorptive component of Hα. The line effect is of order 1-2% in these objects. Naively, the same line effect might be expected across the Hβ but this is not observed. Fig. 2.10 shows the Hα and Hβ P Cygni profile of PDS 27, PDS 37 and PDS 133. The P Cygni absorption seems to be saturated with broad and flat core features for PDS 27 and the absorption is around 0.4 and 0.15 of the continuum level for Hα and Hβ respectively. In PDS 37, the P Cygni absorption is at 0.75 and 0.3 of the continuum level for Hα and Hβ respectively. The absorption in Hβ is thus deeper than that of Hα in both objects. This is not expected as typically the higher lines display weaker absorption. This unusual behaviour is also seen for the Paschen lines as presented in Fig. 2.11. The figure shows that

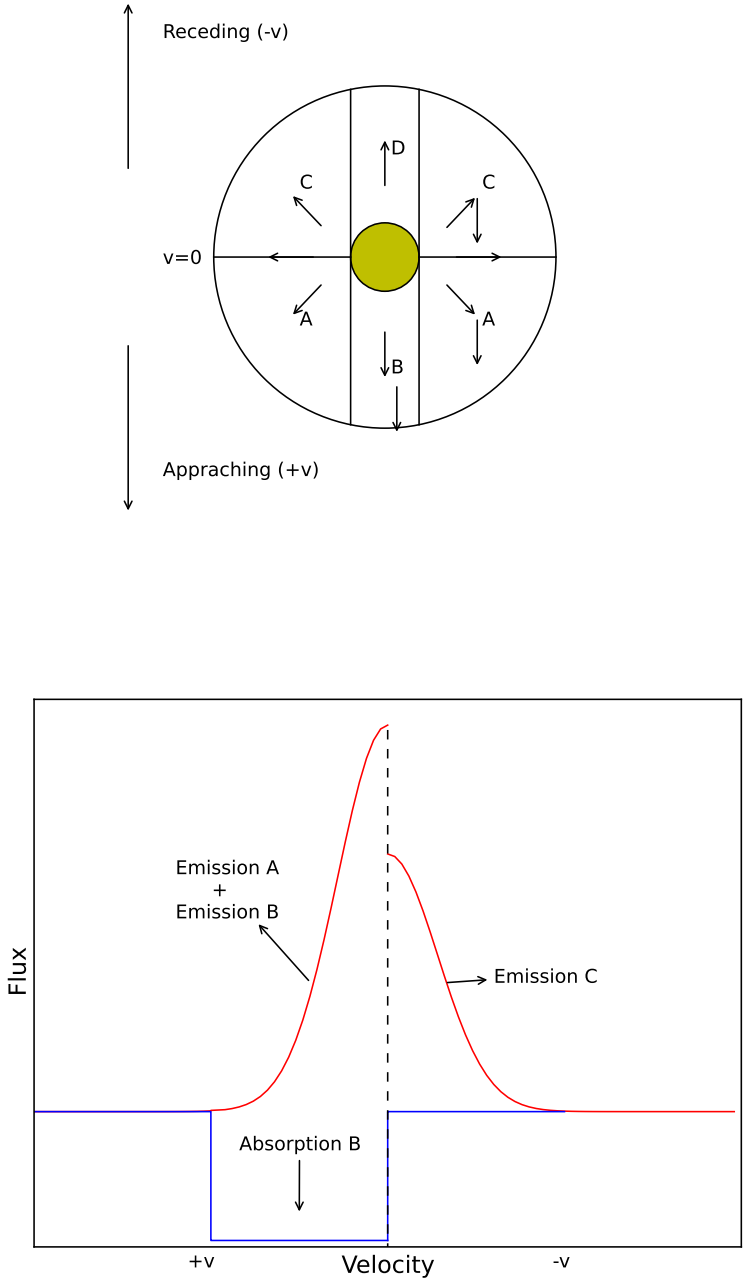

Figure 2.9: Schematic explaining P Cygni profile. In part B the photons are re-emitted to the direction of the observer following the absorption, both the absorption and re-emission are seen by the observer. Part A and C are the front and back sides of the envelope, the photons are re-emitted to the direction of the observer following the absorption of the photons that are not originally directed towards the observer, in these regions the absorption is not seen by the observer. Part D is the obscured region behind the star, this causes the emission profile to be asymmetric.

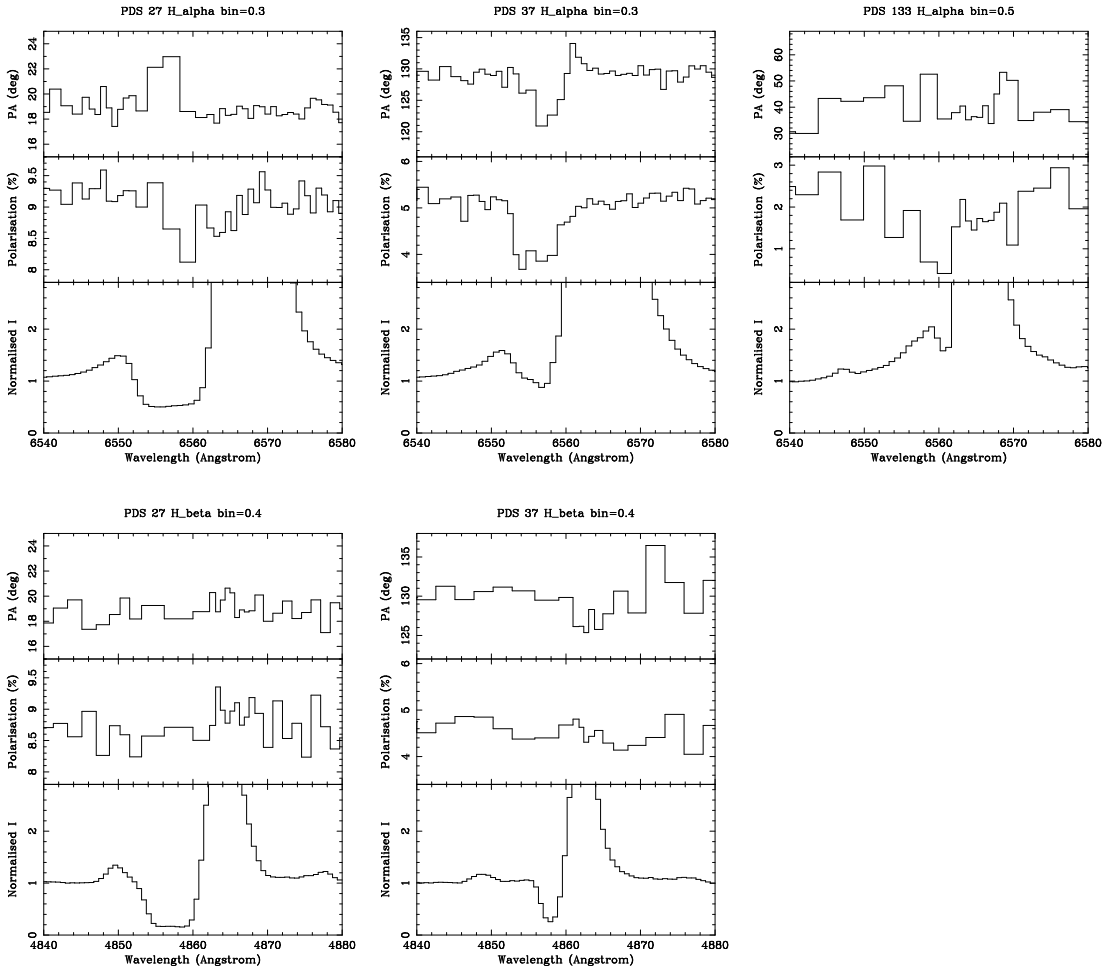

Figure 2.10: Hα and Hβ spectropolarimetry of PDS 27, PDS 37 and PDS 133. For PDS 133 only Hα data is available. See the caption of Fig. 2.5 for more details.

the absorption component of Paβ is weaker than Paγ and Paδ. Unlike PDS 27 and PDS 37 the absorption part of the line of PDS 133 is above the continuum.

By analysing the observed P Cygni spectral lines and the observed polarisation line effects, the McLean effect can be understood in Hα and its absence in Hβ relatively straightforwardly. The strong Hα line photons are scattered into the line of sight filling in the absorption component. If the scattering region is asymmetric, net polarisation across the absorption part of the line will be

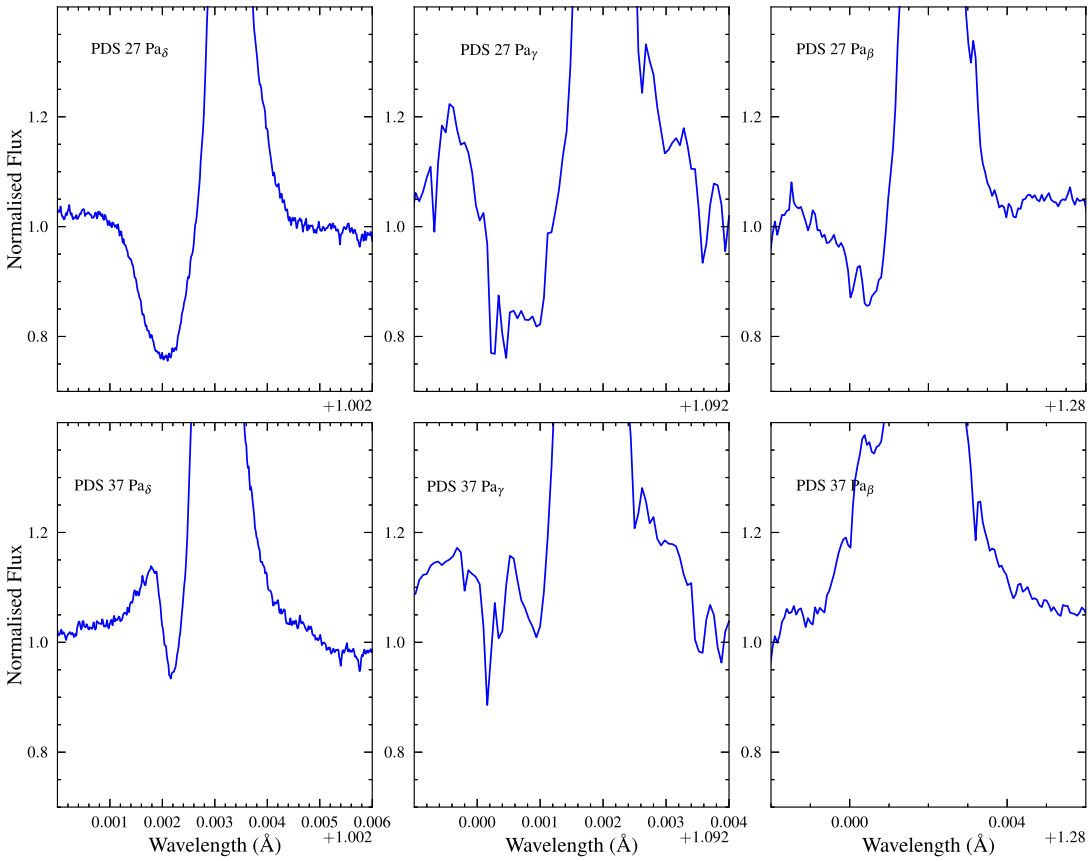

Figure 2.11: The comparison of P Cygni profile,Paδ, Paγ and Paβ of PDS 27 and PDS 37. The spectroscopic data are taken from the HAeBe X-shooter project (Oudmaijer *et al.* 2011; Fairlamb *et al.* 2015)

observable.

The Hβ line, which is weaker than Hα has fewer photons, and will therefore also have fewer scattered photons filling the absorption component (see Fig. 2.10). The net effect is that both the Hβ absorption remains deeper than for Hα, while the scattered, polarised component is less obvious. Therefore, the lack of the scattered photons in Hβ could explain the absence of the line effect across this line. This argument is supported by the observed line effects across the absorptive component of Hα in PDS 27, PDS 37 and PDS 133, as the line effect is stronger

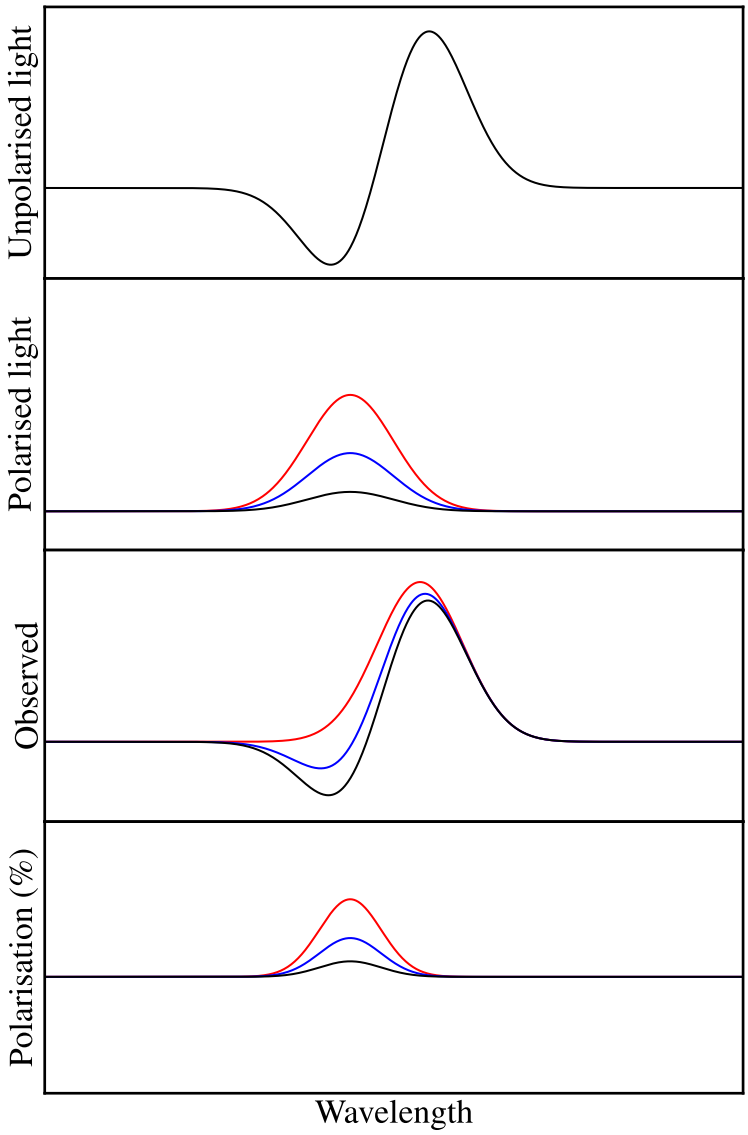

Figure 2.12: Schematic explaining the McLean effect with the data present in three sets: the unpolarised light is shown in the upper panel, polarised light into the line of sight in the upper middle, the observed Hα line profile in the lower middle and the observed polarisation (%) is shown in the lower panel. The absorption is completely filled when there is a significant amount of polarisation in our line of sight, this results in a detection of a notable line effect (red solid line). In contrast, when the polarised light into our line of sight is not sufficient to fill in the absorption component significantly, this results in a weak line effect which is challenging to observe (black solid line). The solid blue line represents an average between the two extreme cases.

for a weaker absorption component. Ababakr *et al.* (2015) suggested a similar scenario in an in-depth study of PDS 27 and PDS 37, but here an extra object, PDS 133, is available that follows the same pattern.

For illustration, I sketch the situation in Fig. 2.12. In the schematic, it can be seen that different levels of polarisation in the line of sight result in different absorption line profiles. In the case of large polarisation, no absorption is seen in the observed line profile as the polarised light fills in the absorption. Interestingly, the McLean effect can thus also be observed in the absence of absorption. In contrast, very deep absorption would be observed when there is little or no polarisation.

2.4.2 The Case of R Mon

A small number of objects display line effects across more lines than Hα alone. I discuss these here, focussing particularly on the most extreme object, R Mon. Its continuum polarisation is large, with values of order 12% and 8%, in the R band in 2012 and 2011 respectively. Unlike the other stars, R Mon displays a line effect across virtually all observed emission lines. The difference between line and continuum polarisation is 7% across the Hα and Hβ lines (see Figs. 2.5 and 2.6), which is large and rare. Typically, the strongest line effect due to electron scattering is of order 2% (Oudmaijer 2007 and Chapter 4). In addition, the direction of the intrinsic polarisation angle from the line effects in the (Q, U) diagram is not constant over different bands. Therefore, it would appear that R Mon is atypical as it differs on many counts from most objects that have been studied spectropolarimetrically.

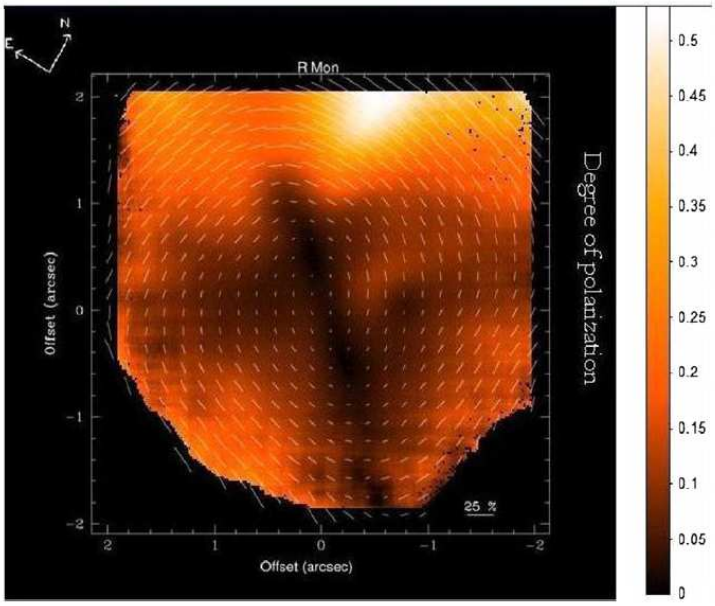

Figure 2.13: Polarisation image of R Mon in H band, the polarisation vector lines show the amplitude of polarisation and the polarisation position angle. The figure is taken from Jolin *et al.* (2010).

Relevant to this discussion is that R Mon is an extended object. Its reflection nebula is due to radiation from the inner parts, such as the star and wind, being scattered off circumstellar dust particles, resulting in strong polarisation. Spatially resolved polarisation images reveal polarisation in excess of 50 % (Jolin *et al.* 2010) (see Fig. 2.13). This polarised flux is largest closest to the star and decreases with distance, while the polarisation angles follow a centro-symmetric pattern. For a circularly symmetric, highly polarised object on the sky, the same would apply, but if it were unresolved, the net observed polarisation would be zero. However, because R Mon is asymmetric, a net polarisation will be observed, and this is even stronger in our data as the scattering circumstellar material is resolved and larger than the slit.

These features have important consequences for the observed polarimetry.

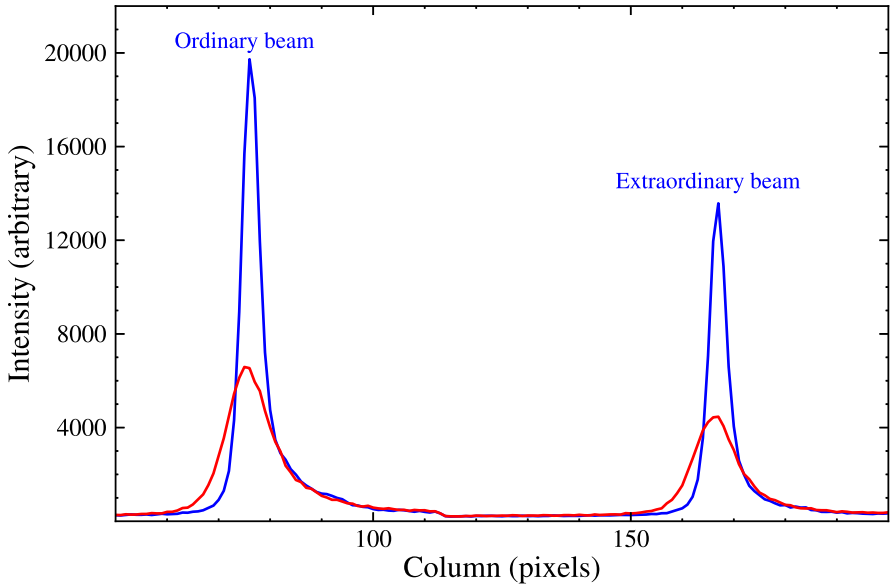

Figure 2.14: Ordinary and extraordinary polarisation beams at the Hα line of R Mon. The 2011 data are represented by red line while the blue line represents the 2012 data.

Below I will argue that this is the main reason that the (spectro-)polarimetric properties of R Mon are different from the other stars, and that the various emission lines originate from different line forming regions. For example, given that the polarisation drops off rapidly with distance from the star, a slight change in seeing or slight change in the positioning of the slit can result in largely different polarised light entering the slit. In addition, larger positioning errors can result in differently observed position angles, as the PA depends on position.

Inspection of the raw spectropolarimetric data shows that the width of the ordinary (O) and extraordinary (E) beam in the spatial direction in the 2011 data is about twice that of the 2012 data (and wider than the data for the other stars) (see Fig. 2.14). In addition, the individual beams do not follow the typical Gaussian shape of the seeing profile, but appear asymmetric. This confirms that R Mon is not a point source but an irregular, extended object.

I will discuss here the polarisation properties of R Mon in this context, starting with its observed broadband peculiarities. The polarisation seemingly increased by 4% over a timespan of 4 months, while the polarisation angle stayed the same. The slit direction and position were the same for both observations but as mentioned above, the spatial profile of the 2011 data, which has a smaller level of polarisation, is much wider than that in 2012 smearing at polarisation. As the polarisation closest to the object is highest, it follows that the net polarisation in 2012 is higher. A similar argument can be put forward to explain the discrepant position angles for each of the wavebands the object was observed. In Fig. 2.4, the slope of the PA is the same for the V, R and I bands, but they are offset by 10$^{\rm o}$ (see also Table 2.3). According to the data in Jolin *et al.* (2010), the polarisation is centro-symmetric, and the polarisation angle changes with at least 20° every 1 arcsec (see Fig. 2.15). Hence, a slight displacement can result in a noticeable change in PA. I argue, therefore, that the fact that R Mon is extended and asymmetric explains the high polarisation, large continuum variability, and offset in PA for the various wavelength settings. However, the cause of the observed discrepant position angles from one setting to another for other objects, for example MWC 275 and PDS 37, is unknown. The seeing is fairly constant among different settings for these two objects (see Table 2.2), and unlike R Mon their seeing profiles follow the typical Gaussian shape.

In regard to the spectropolarimetric properties, of which the fact that most lines seem to exhibit a line effect, and that the line effect is large, makes R Mon stand out.

The left hand panel of Fig. 2.16 shows the *(Q, U)* diagram of three forbidden lines of R Mon, with each line taken from a different wavelength setting. The

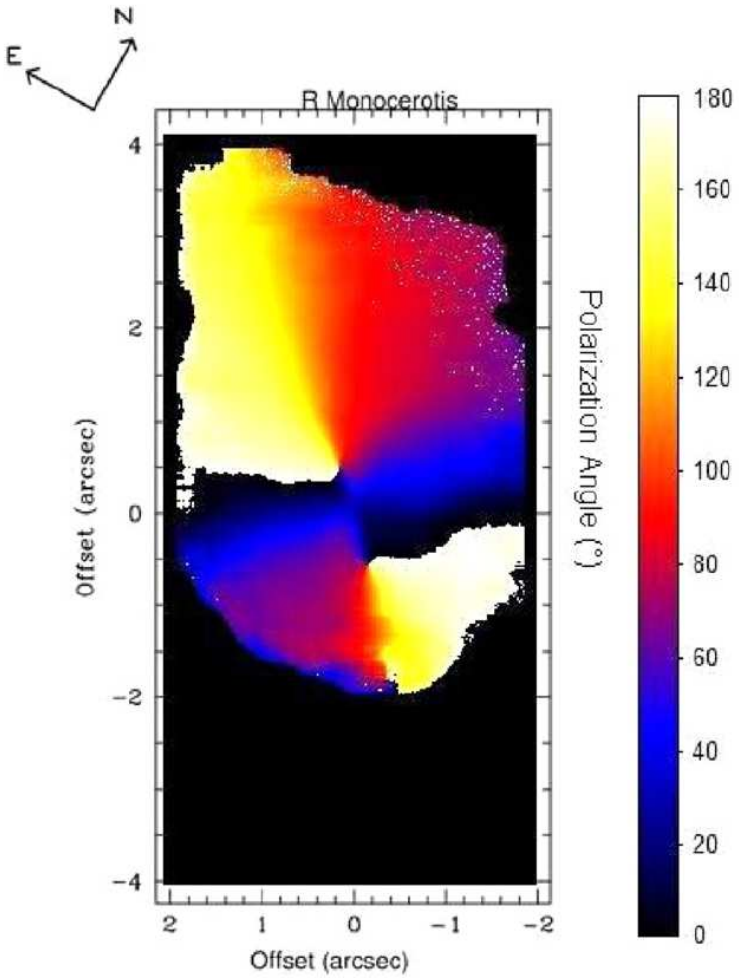

Figure 2.15: Polarisation position angle of R Mon in H band. The figure is taken from Jolin *et al.* (2010).

right hand panel shows lines from different wavelength settings as well; Hβ, Hα and a Ca II triplet line, at 8662 Å. The line excursions are large, ranging from $\sim$5% to $\sim$10% in Hα. The direction of the intrinsic polarisation angle is roughly the same for all forbidden lines, with an average value of 64 $\pm$ 5°. However, very different intrinsic angles of 90 $\pm$ 15°, 57 $\pm$ 10° and 128 $\pm$ 10° are found for Hβ, Hα and the Ca II triplet line respectively. The Hα and Ca II triplet data were taken at the same date while Hβ was taken a few days later. The polarisation

angle in Hα is the only one consistent with the forbidden lines.

The question that now arises is how can the line effects be strong, and why would the intrinsic angles be different for the various lines? By simply stating that the lines are formed in a larger region than the star and would be less prone to scattering, such as the polarisation dilution discussed in Trammell *et al.* (1994), does not hold in the current situation. The reflecting dust is located far away from the star and is in all likelihood much more extended than the ionized wind. In this case, the emission lines will be equally likely to be scattered and thus as polarised as the continuum. The remaining possibility is that the line emitting regions themselves are not isotropic - either asymmetric or clumpy, leading to a polarisation line emission different from the continuum. The different polarisation angles for the various lines may be the result of different geometries and volumes of the line forming regions. The optically thick Hα emission and the forbidden lines originate from large, possibly similar volumes, which could follow similar scattering paths, whereas other lines arise in regions closer to the star and have potentially different geometries, leading to different polarisation angles.

To our knowledge this is the first time an object has been reported to have so many lines with a polarisation effect across them. It will not be trivial to disentangle the various contributions and multi-parameter modelling is needed to retrieve the geometry of the system. This is beyond the scope of the current work. For the above reasons, the line spectropolarimetric result of R Mon is not used in the statistical conclusions in Chapter 4.

Another object, CPD-485215, also displays many line effects across the emission but again the intrinsic polarisation angle is not constant (see Fig. 2.16). In this case, all the spectral lines have an intrinsic angle of 60 $\pm$ 15° while the for-

bidden lines give an angle of 11 ± 5°. However, PDS 133 is the only object that has the same polarisation angle in both Hα and [O I] at 6300 Å (see Fig. 2.16), this suggests that both lines emerge from the same volume. This is evidenced by the observed profile of [O I] at 6300 Å which is unlike R Mon and CPD-485215, it is broad and double peaked.

2.5 Final Remarks and Conclusions

I have performed the first linear spectropolarimetry over a large wavelength range of a sample of HAeBe stars. The spectra cover the range from 4560 Å to 9480 Å, including many emission lines such as: hydrogen recombination lines, Ca II, Fe II, O I and He I and several forbidden lines including [O I], [Fe II] and [S II]. All the objects have a measurable continuum polarisation, ranging from ∼0.3 % in the very low polarised star HD 85567 to ∼12 % in the highly polarised star R Mon. Our values are broadly consistent with these values but there are some variations from the literature values. The continuum polarisation of some of our objects do not follow the general trend of the Serkowski law. This is evidence of the presence of intrinsic polarisation in the observed continuum polarisation as the interstellar polarisation does not vary significantly over time.

All the objects show a sign of line effect across Hα. All HBe objects display either a classical depolarisation or a McLean effect signature. The HAe objects show a mixture of McLean, depolarisation, intrinsic line polarisation and complex line effect. This suggests that the circumstellar environments around HAeBe stars have a flattened structure. Four objects in our sample show a McLean effect, where the change in polarisation occurs across the absorptive component of the

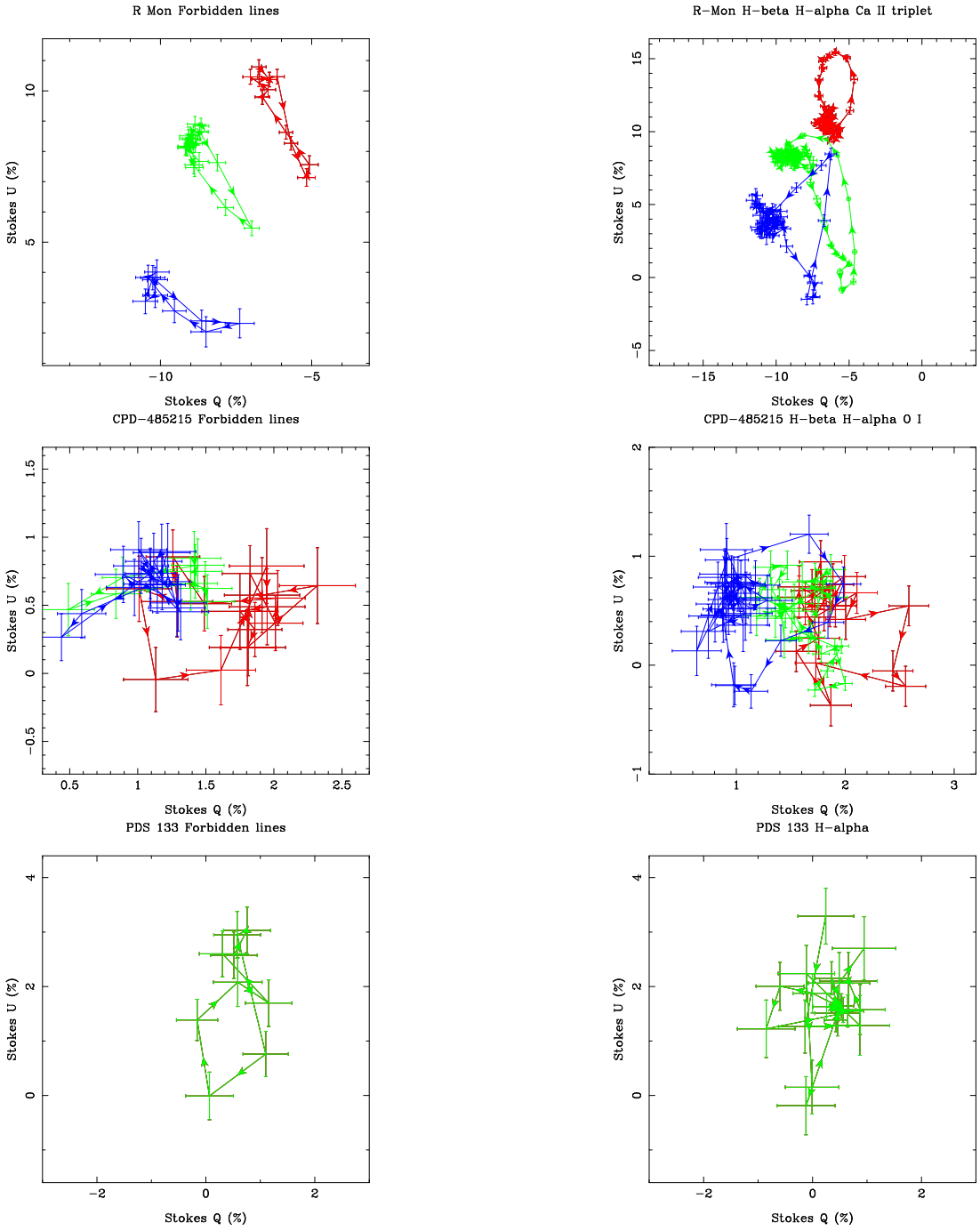

Figure 2.16: (*Q, U)* diagram of several spectral lines and forbidden lines of R Mon, CPD-485215 and PDS 133. The lines are taken from *B* band (blue solid line), *R* band (green solid line) and *I* band (red solid line). In R Mon Hβ, Hα and Ca II triplet at 8662 Å are presented in blue, green and red lines respectively (right); three forbidden lines: [Fe II] at 5158 Å, [O I] at 6364 Å and [Fe II] at 8616 Å are shown in blue, green and red lines respectively (left). In CPD-485215 Hβ, Hα and O I at 7773 Å are presented in blue, green and red lines respectively (right); three forbidden lines: [Fe II] at 5333 Å, [O I] at 6300 Å and [Fe II] at 8616 Å are shown in blue, green and red lines respectively (left). In PDS 133 Hα is presented in green line (right); forbidden line [O I] at 6300 Å is shown in green line (left).

emission line of Hα. This suggests that the distribution of the ionised material is not circular on the sky. From these four objects Hβ data are only available for PDS 27 and PDS 37. The same line effect would be expected across the absorption component of Hβ. However, the absorption in Hβ is approximately three times stronger than that of Hα. This apparent inconsistency can be explained by the fact that strong Hα line emission scatters into our line of sight filling in the absorption component. The Hβ line is weaker than Hα and thus fewer scattered photons fill in the absorption component, yielding a much lower polarisation effect, consistent with the observed non-detection.

It would appear, therefore, that the differing polarisation behaviour can be explained across the absorption parts of the Hα and Hβ lines very well in the context of the McLean effect. An alternative scenario to explain polarisation across the absorption parts of hydrogen lines was put forward by Kuhn *et al.* (2007). Essentially this invokes selective optical pumping of the lines, predicting that both Hβ and Hα will have polarisation effects of similar magnitude (Kuhn *et al.* 2011, their Figs. 4 and 5). This is not what has been observed in our data. What is more, this scenario will also struggle to explain why the Hβ absorption is so much stronger than that of Hα. Within the current set of observations, the McLean effect seems to be a more viable explanation.

Four HBe objects show a depolarisation line effect, where the change in polarisation is as broad as the emission line. This suggests that Hα emerges in an extended circumstellar disk. Two HAe objects show an intrinsic line polarisation, where a significant portion of the photons emerge from accretion hot spots. BF Ori and HD 104237 show a possible line effect across Hα.

I have observed depolarisation line effects across [O I] lines at 6300 and 6364 Å

in PDS 133, R Mon and CPD-485215. The line profile in PDS 133 is broad and double peaked unlike the other two, which are narrow and single peaked. The line profiles may suggest that the lines originate from a rotating disk in PDS 133 while in R Mon and CPD-485215 many forbidden lines display a depolarisation line effect. It is to be expected to see a depolarisation line effect across [O I] in PDS 133 as they originate in the disk further out from the inner ionised disk. The Ca II triplet also shows a depolarisation in MWC 275. These lines have low ionisation potential energy as they are formed in a predominately neutral zone. In general they originate in the circumstellar environment but outside the hydrogen ionisation boundary. Therefore, a depolarisation line effect might be expected across these lines. However, for the objects that display a depolarisation line effect, the Ca II triplet line effects are either absent or very weak.

Finally, I have presented the medium resolution spectropolarimetry on the entire optical range from 4560 Å to 9480 Å of a sample of 12 HAeBe stars. The data allow us to draw the following conclusions:

- I sample linear line spectropolarimetry in the optical wavelength range, which is much larger than any previous work at similar spectral resolution.

- Changes in the polarisation across the Hα emission line are detected in all objects, as an indication of a flattened structure of the circumstellar environment. The line effects vary from depolarisation, line polarisation to the McLean effect.

- Depolarisation and the McLean effect are observed in Be type stars predominantly in early B type stars while line polarisation is observed in Ae type objects.

- The McLean effect is observed only across the absorptive component of Hα and the line effect is stronger for a weaker absorption component, while Hβ does not display the effect. I propose a scenario to explain this property. It is based on the fact that the photons from the strong Hα line are scattered into the line of sight. As a consequence, the photons in the absorption are more polarised than the emission. A side result is that the selective absorption due to optical pumping as proposed by Kuhn *et al.* (2007) is unlikely to be responsible for the polarisation behaviour in these objects.

- A broad depolarisation line effect is detected across Ca II triplet and [O I] in two objects. These lines are emerging further away from the star and Hα region in the circumstellar environment. The depolarisation simply implies that the circumstellar environment has an asymmetrical structure in this region.

- The few spectra with calcium triplet lines that show an effect show a similar polarisation profile for all members of the triplet. I confirm a similar observation by Kuhn *et al.* (2011) for an evolved, RV Tau star. As these authors explained, resonant line scattering can then not be the cause for the observed line polarisation, as the Ca II 8662 Å comes from a different upper level than the other members of the triplet. Similar polarisation due to line scattering would then not be expected.

- Finally, apart from Hα, few lines in few objects show a line effect in the polarisation. I present the case of R Mon, which displays exceptionally strong line effects in most of its emission lines. In addition, not all lines show the same type of line effect. This can be explained by the fact that the

object itself is resolved and propose that different line forming regions and geometries are responsible for polarisation properties of the higher hydrogen recombination lines and forbidden lines and Hα on the other hand.

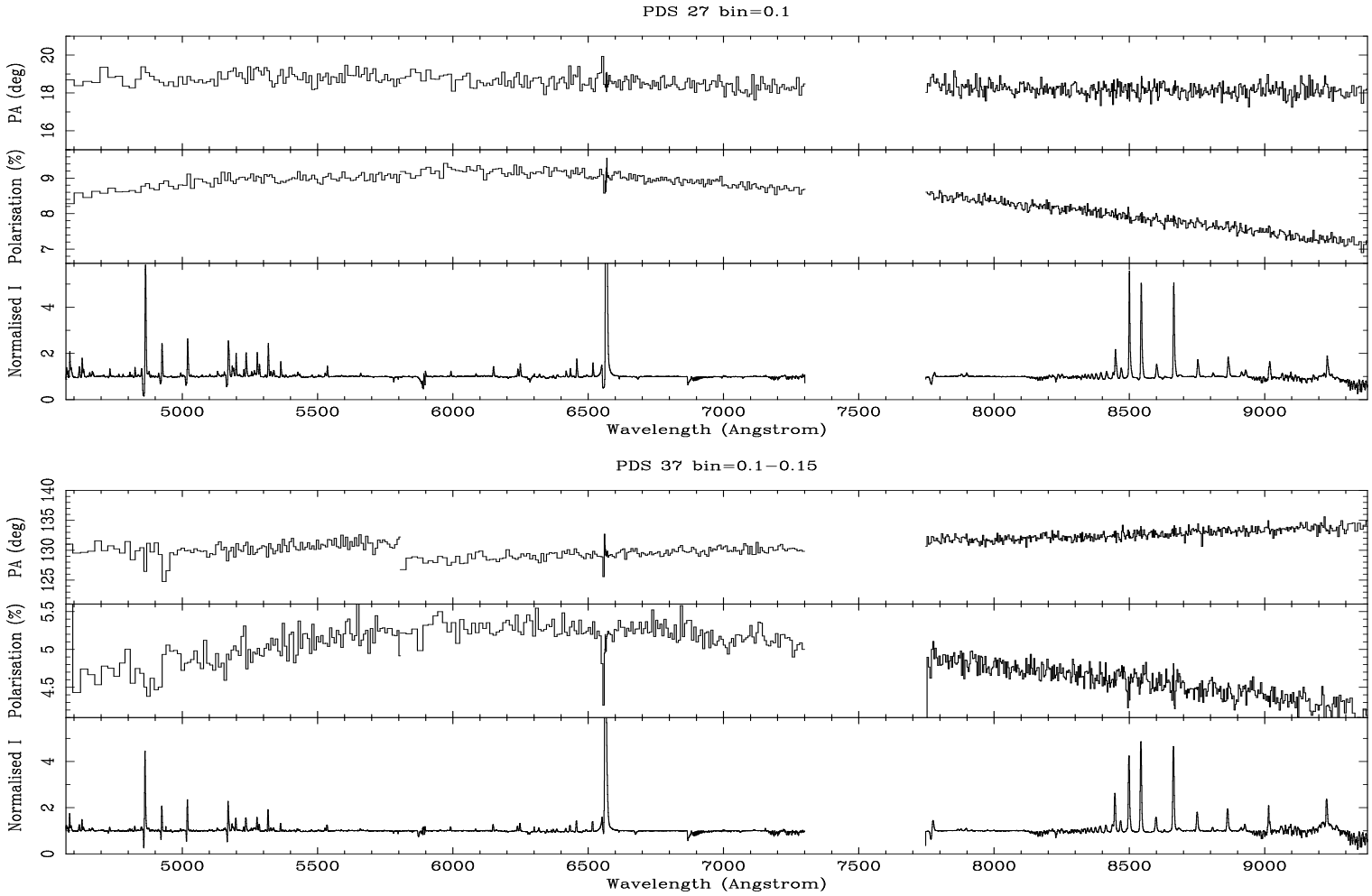

Figure 2.17: The polarisation data in V, R and Z bands for PDS 27, PDS 37 ,CPD-485215, R Mon and V380 Ori; and in R and Z bands for GU CMa, HD 98922, PDS 133, HD 104237, MWC 275, BF Ori and HD 85567. R Mon, V380 Ori and HD 85567 are presented in two epochs in R. The data are presented as a triplots. In the triplot polarisation spectra the Stokes intensity (I) is shown in the lowest panel, polarisation (%) in the centre, while the position angle (PA) is shown in the upper panel. The data are rebinned to a constant value, as indicated at the top of each plot.

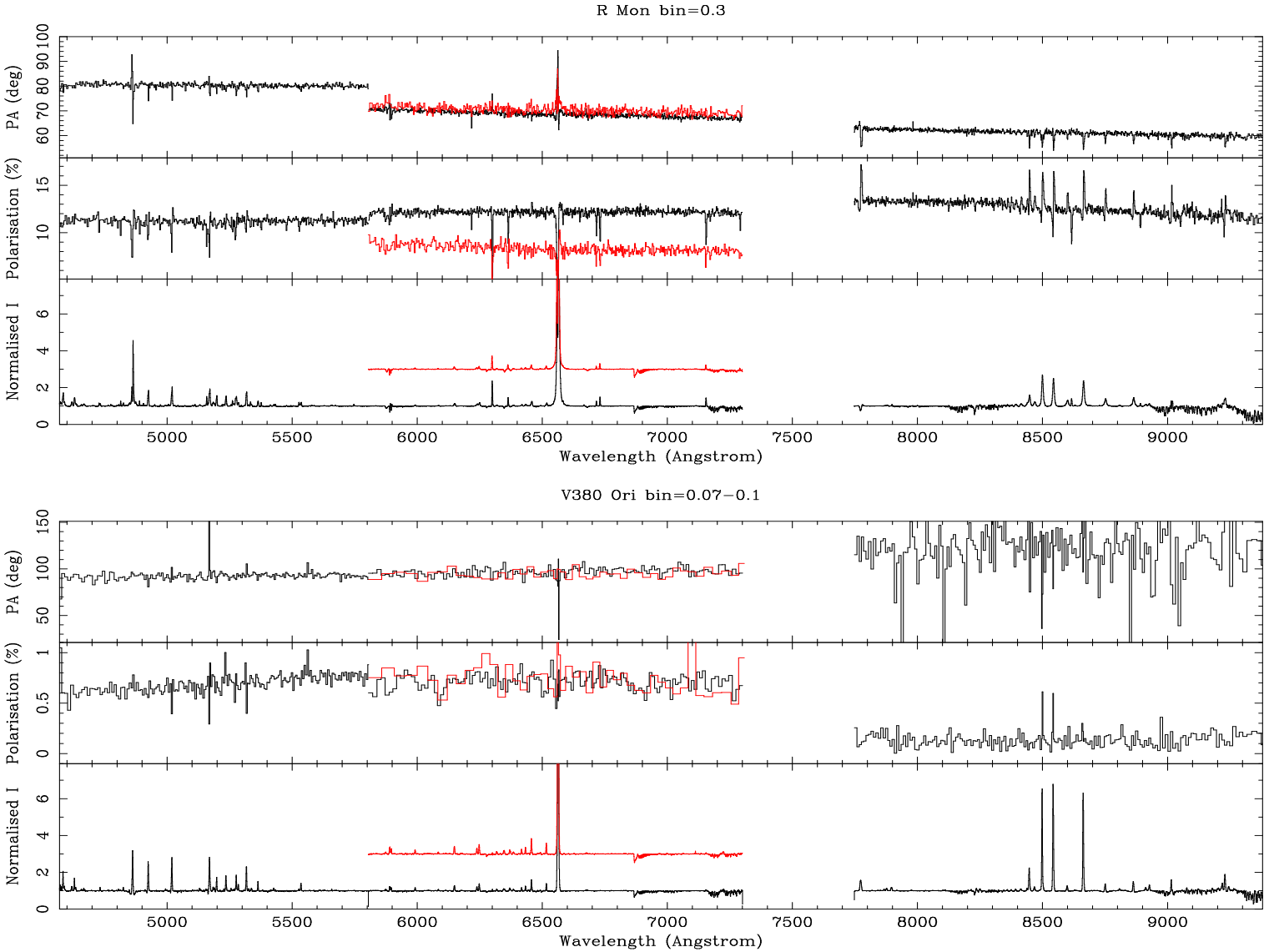

Figure 2.17: continued

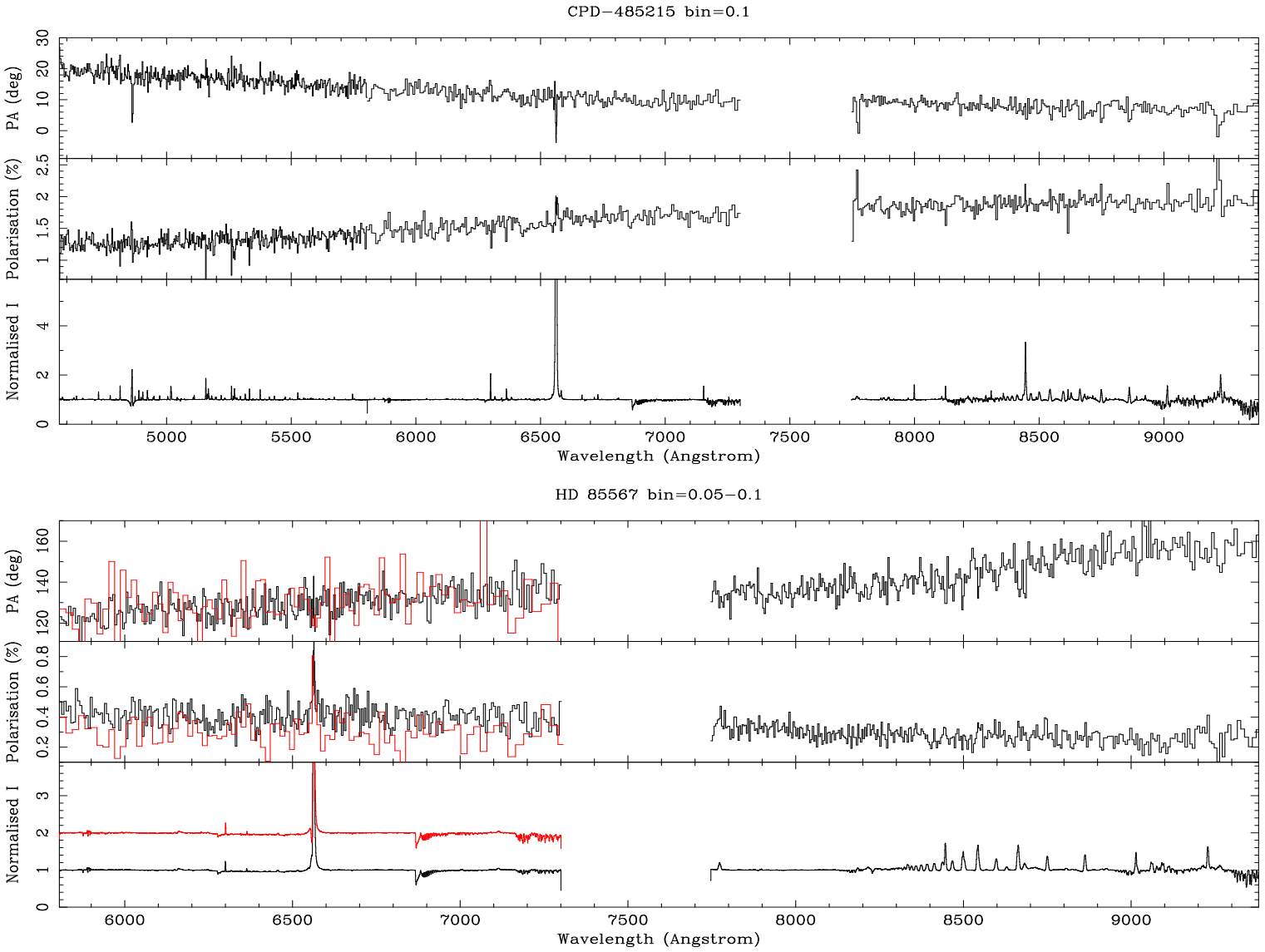

Figure 2.17: continued

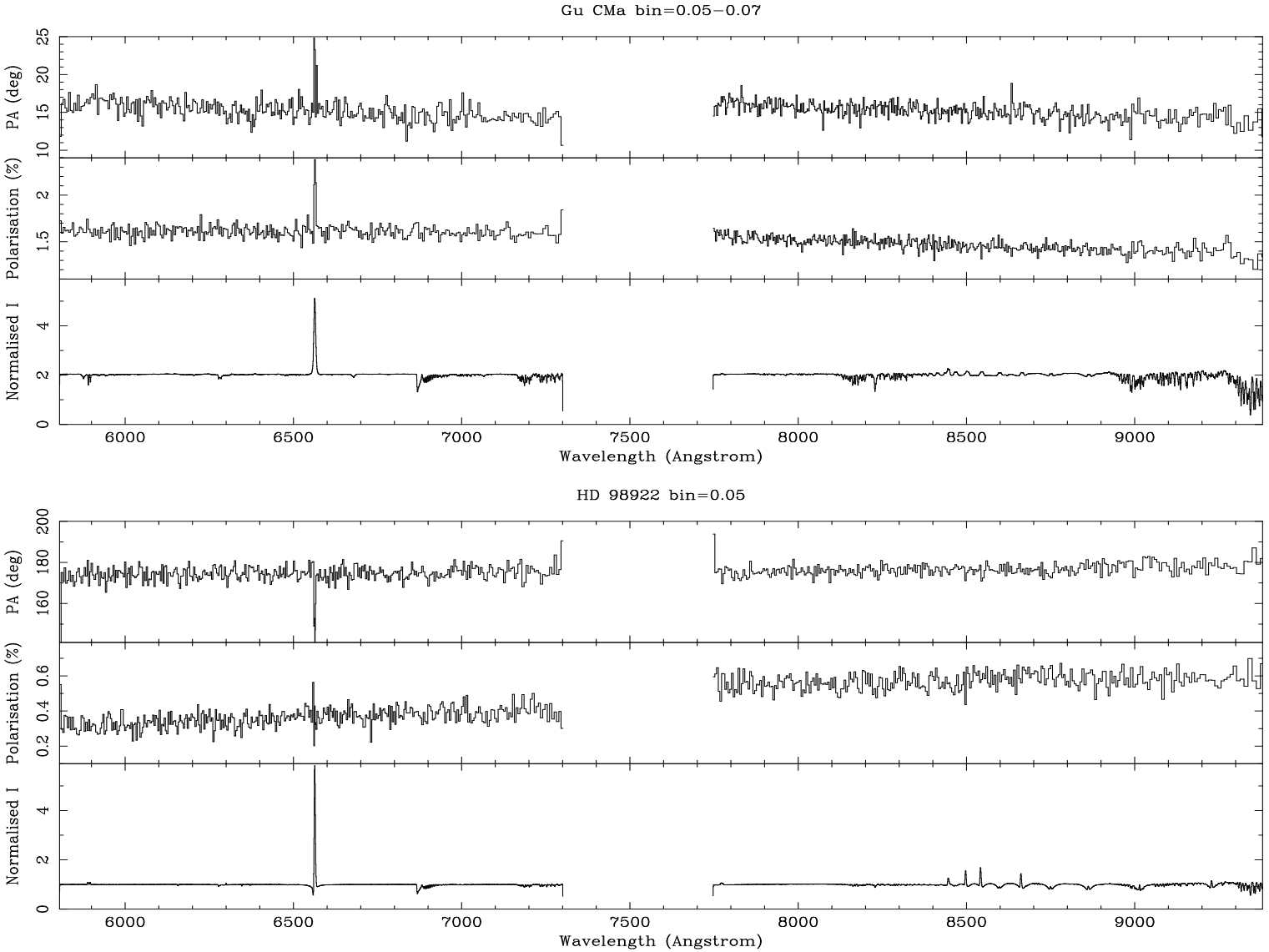

Figure 2.17: continued

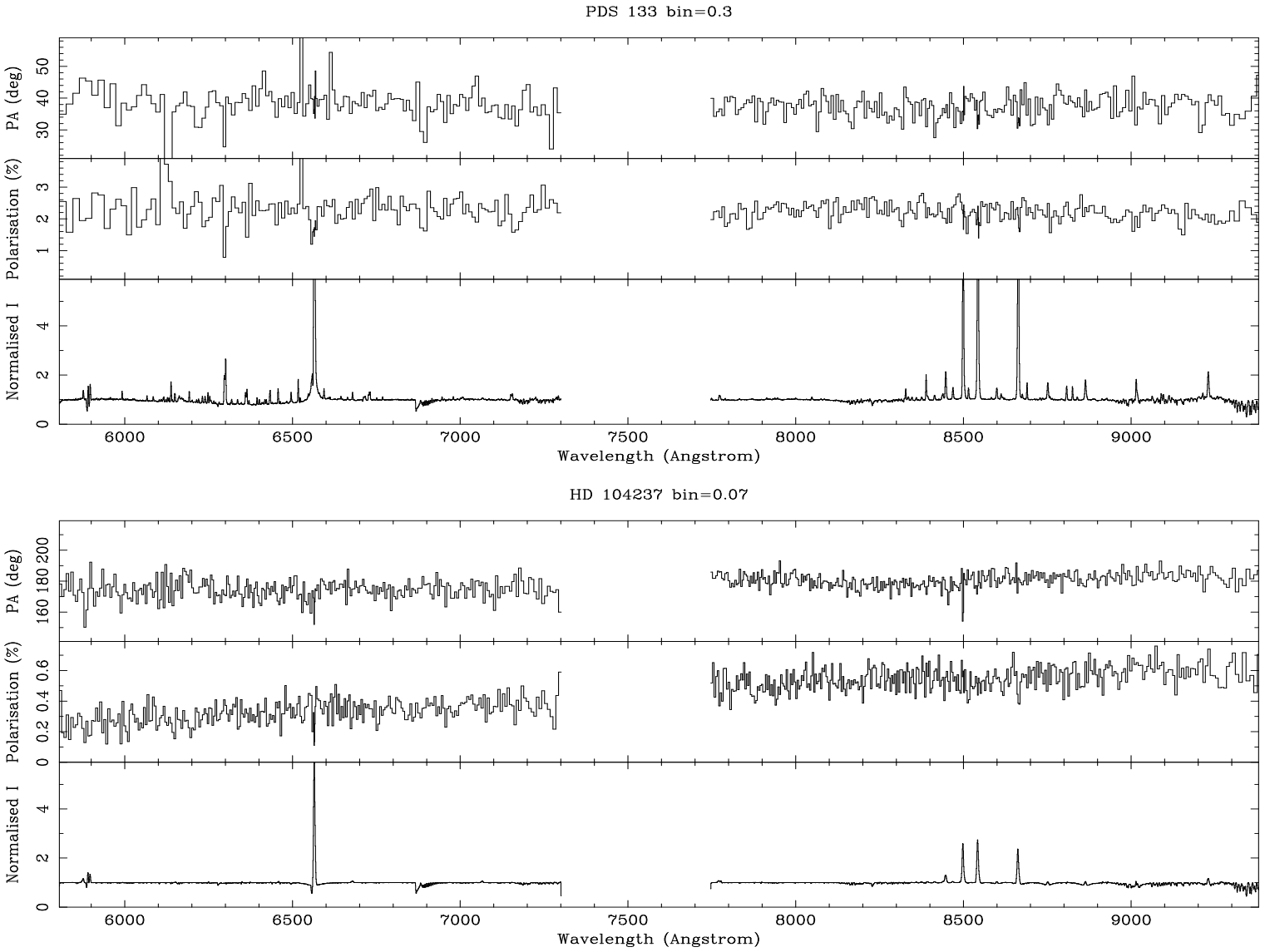

Figure 2.17: continued

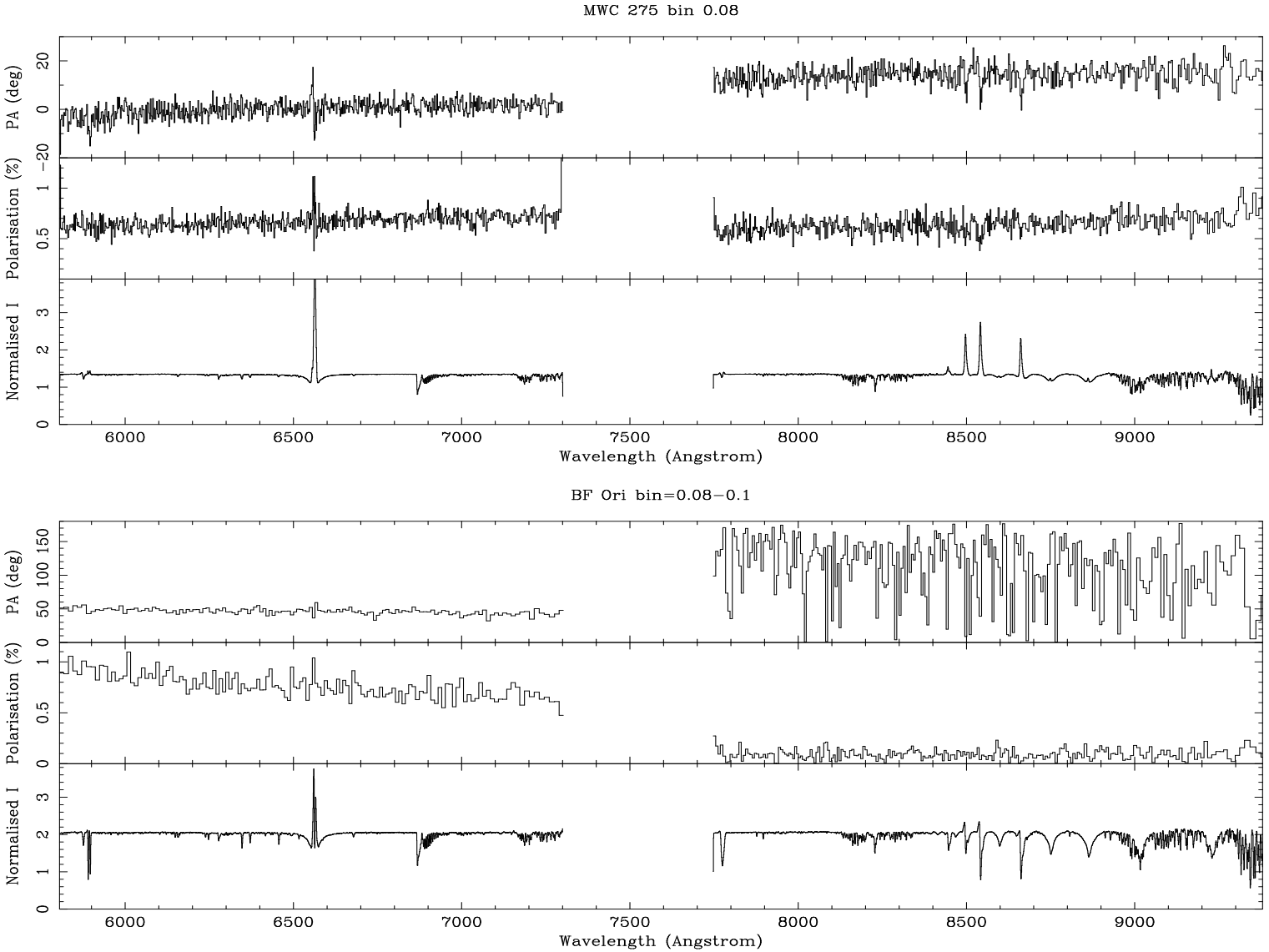

Figure 2.17: continued

Chapter 3

Observational Study of the Early Type Herbig Be Stars PDS 27 and PDS 37

3.1 Introduction

To study the star formation mechanism as a function of mass, it is necessary to sample a large number of HAeBe stars, with many representatives in all mass bins. The known sample of HAeBe stars [see e.g. the catalogue by The *et al.* (1994)] contains many A-type and late B-type objects, but there is a dearth of the earliest type, most massive HBe stars (also see e.g. Ochsendorf *et al.* 2011). In this chapter I present an in-depth investigation of two early HBe star candidates identified by the Pico dos Dias Survey (PDS). Based on their observational characteristics, PDS 27 (also known as DW CMa, RA 07:19:36, Dec. −17:39:18) and PDS 37 (also known as Hen 3-373, RA 10:10:00, Dec. −57:02:07.3) were proposed

to be early type Herbig stars by Vieira *et al.* (2003). The young nature of PDS 27 was also suggested by Suárez *et al.* (2006). Both stars were also classified as young in the Red MSX Source (RMS) survey for Massive Young Stellar Objects (MYSOs) (Lumsden *et al.* 2013). In 2011, Vieira *et al.* (2011) considered PDS 27 to be an evolved star instead, but ruled out an evolved nature for PDS 37. However, as I will demonstrate in this chapter, both objects are very similar, and I proceed under the assumption that they are young stars.

Using optical photometry, the temperature has been estimated to be around 22000 K for both objects (Vieira *et al.* 2003). Vieira *et al.* (2003) also estimated their distance and it was found to be 1100 pc for PDS 27 and 720 pc for PDS 37; PDS 27 is associated with CMa star-forming region while PDS 37 is associated with C 282.4+0. Ilee *et al.* (2013) studied the near-infrared (NIR) first overtone CO emission of PDS 37, and assuming that it originates from the circumstellar disc, they found the disc to be highly inclined to the line of sight (80°). Rodrigues *et al.* (2009) determined an intrinsic polarisation of 2.77% for PDS 37, suggesting that the circumstellar environment is not spherical.

Here I present a spectroscopic and spectropolarimetric study of these two objects. I will use the large wavelength coverage provided by X-shooter to determine the stellar parameters. Spectropolarimetry is a very powerful technique that can probe very small unresolved spatial scales of the order of stellar radii and allows one to extract information on the geometry of this material (see e.g. Oudmaijer & Drew 1999; Vink *et al.* 2002, 2005a and Chapter 1). A new element in the present study is that the medium-resolution spectropolarimetry has a wavelength coverage from 4560 to 9480 Å, which is much larger than presented in any previous study at similar spectral resolution. Another powerful technique

to study the circumstellar environment is interferometry. The inner gaseous and dusty disk is typically less than 10 au which requires a high angular resolution and the temperature in this region is of order of ∼1500 K. These make near infrared interferometry an ideal tool to reveal this region. I will present the results of the PIONIER interferometric data in the H-band continuum to further investigate the circumstellar environment of these two interesting objects.

This Chapter is organised as follows: in Section 3.2 the observations and data reduction are discussed. The results are presented in Section 3.3. Section 3.4 presents an analysis of the data followed by a discussion in Section 3.5. Finally, conclusions are drawn in Section 4.6.

3.2 Observations and Data Reduction

3.2.1 Spectropolarimetry

The data of PDS 27 and PDS 37 were taken as part of a wider spectropolarimetric investigation whose results are presented in Chapter 2. The details on the objects selection criteria, observation and data reduction procedures are contained in Chapter 2.

3.2.2 Spectroscopy

The spectroscopic data of PDS 27 and PDS 37 were obtained using the medium-resolution spectrograph X-shooter, mounted on the VLT, Chile (Vernet *et al.* 2011) as part of a larger programme (Oudmaijer *et al.* 2011; Fairlamb *et al.* 2015). One of the main strengths of the instrument is its huge wavelength cover-

age, taken simultaneously, over three arms: 3000 - 5900Å, UVB; 5300Å - 1.0μm, VIS; and 1.0 - 2.4μm, NIR. The smallest slit widths available (0.5 arcsec - UVB, 0.4 arcsec - VIS and 0.4 arcsec - NIR) were used and provided the highest spectral resolution available for X-shooter: R=9100, 17400 and 11300, respectively. Both objects were observed in nodding mode in an ABBA sequence. Two observations were made of PDS 27, on the evenings of 2009 December 18 and 2010 February 24 (these data sets will be referred to as X-shooter(a) and X-shooter(b), respectively, for the remainder of this chapter). The exposures were the same for each observation with a breakdown across the arms of UVB - 300s×4, VIS - 300s×4 and NIR - (2s×6)×4. PDS 37 was observed on the evening of 2010 March 31 with exposures of UVB - 300s×4, VIS 300s×4, and NIR (3s×6)×4. The spectra of both objects were reduced automatically by ESO, using the X-shooter pipeline v0.9.7 (Modigliani *et al.* 2010) following standard reduction procedures (flat-fields, wavelength calibration, etc.). I have noted that there is a shift in the spectrum of both objects, indicating that the wavelength calibration was not quite right. I used several telluric absorption lines using a solar spectrum catalogue (Delbouille *et al.* 1973) to manually perform the final wavelength calibration. Telluric lines are present in the spectra in the range between 6800 Å to 1000 Å. There is an average shift of the order of -6 kms^{-1} and -2 kms^{-1} for PDS 27 (X-shooter(b)) and PDS 37 respectively, the spectra were corrected accordingly. In the spectrum of PDS 27 (X-shooter(a)), only a negligible shift of the order of -0.2 kms^{-1} was found.

3.2.3 Interferometry

The near infrared interferometric data of PDS 27 and PDS 37 were obtained with the PIONIER, H band 4 beam combiner, at the VLT by using the 8.2 m Unit Telescopes (UT). With PIONIER, the visibility can be measured with six baselines simultaneously. Two observations were made for PDS 27 during the nights of 2015 March 2 and 3 (these data will be referred to as PDS 27(1) and PDS 27(2) respectively for the reminder of this chapter). The data from only three baselines are available for PDS 27(1). The data of PDS 37 were taken on the night of 2015 March 1.5. The baselines are ranging from 47 to 130 m, this corresponds to a maximum resolution of ~ 3 mas at 1.65μm (1.5 au at 1kpc, typical distance for massive stars). The data were reduced using the automated pipeline at ESO, the PIONIER pipeline was developed by Le Bouquin (Le Bouquin *et al.* 2011).

3.3 Results

3.3.1 Spectral Lines

The spectra of both stars are remarkably similar showing numerous emission lines, while there is a paucity of photospheric absorption lines. A representative set of lines is shown in Fig. 3.1.

The strongest emission is found among the hydrogen recombination lines, Fe II, Ca II and [O I]. The Hα and Hβ lines have P Cygni profiles, with absorption observed at velocities in excess of 500 kms^{-1} in the case of PDS 27, with some emission observed bluewards of the P Cygni absorption. The Hα lines are very strong with line-to-continuum ratios of the order of 20 and an equivalent width

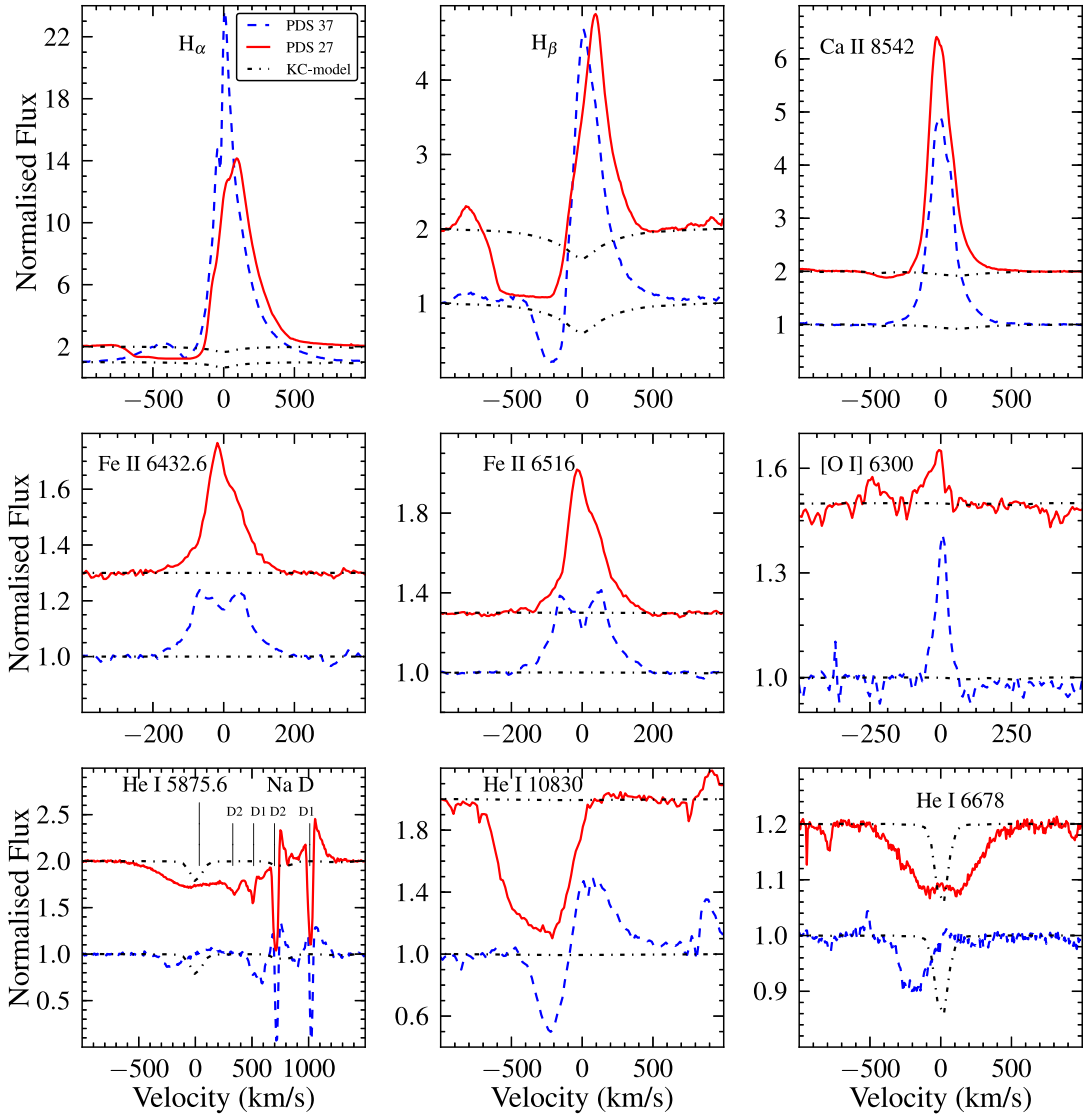

Figure 3.1: A selection of observed spectral lines from the X-shooter data is shown for both targets (for PDS 27 only the X-shooter(b) data set is shown for clarity). The spectra are shifted such that their systemic velocity (see the text) is 0 kms^{-1}. The red solid line denotes PDS 27, while the blue dashed line is PDS 37. The black dash-dotted line is a Kurucz-Castelli (KC) model atmosphere for a 21000 K type star (Kurucz 1993; Castelli & Kurucz 2004); this is an upper limit to the temperature (this limit will be discussed in Section 4.1.3). The spectra of both objects are normalised to one but PDS 27 is shifted by an arbitrary value for clarity. Note the similarity of both objects' spectra, with a difference being the number of double-peaked lines of Fe II in PDS 37. Blueshifted absorption reaching -700 and -400 kms^{-1} is observed in Hα and helium for PDS 27 and PDS 37, respectively.

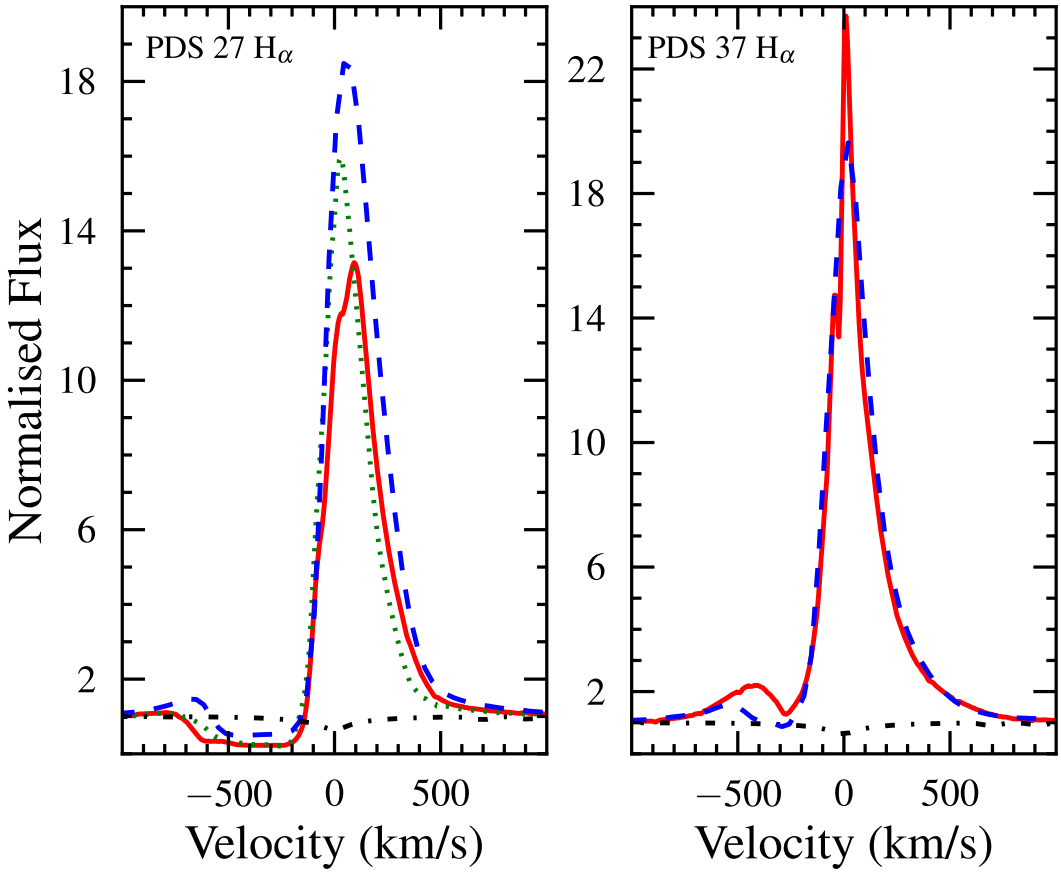

Figure 3.2: Hα line variability from three observation epochs for PDS 27: FORS2 (blue dashed line) and two X-Shooter epochs, X-shooter(a) (green dotted line) and X-shooter(b) (red solid line). For PDS 37, there is only one X-shooter data set (red solid line). A KC model (black dash-dotted line) of temperature 21000 K is also overplotted. The lines are shifted to the rest wavelength of the stars as in Fig. 3.1.

(EW) of -70.4 and -111.4 Å for PDS 27 and PDS 37, respectively. Several strong Fe II emission lines can be seen in the visible portion of the spectra; the majority of these are double peaked in PDS 37, while they are all single peaked in PDS 27. Strong emission is also present in the Ca II (8498, 8542, 8662 Å) and Ca II doublet (8912, 8927 Å) in both stars. The Ca II triplet lines are blended with the Paschen lines at 8502, 8545 and 8665 Å. The Ca II lines at 8542 and 8662 Å in PDS 27

have a very weak blueshifted absorption. The other nearby Paschen lines at 8598, 8750 and 8863 Å have similar absorption components. Therefore, the absorption seen in the Ca II lines is more likely to belong to lines from the Paschen series with which they are blended. He I lines at 5875, 6678, 7065 and 10830 Å are in absorption and blueshifted to the same velocities as observed in the hydrogen P Cygni profiles. He I at 10830 Å has a P Cygni profile in PDS 37 with absorption observed up to -450 kms^{-1}, and the EW of the emission is slightly larger than that of the absorption. For PDS 27, He I at 10830 Å has a very strong absorption up to -700 kms^{-1} and is accompanied by a very weak redshifted emission component. As we go from low-order lines in the hydrogen Balmer series (Hα, Hβ) towards the higher order hydrogen lines, we see a progressively weaker absorption component in each line. The only exception is that the absorption in Hα is less deep than in Hβ, which I shall discuss later. The varying hydrogen line profiles prevent a reliable measurement of the stars' radial velocity (V_{r}). Therefore, to obtain the systemic velocity, I measured the V_{r} from the clean and symmetric Fe II and Ca II triplet lines in the X-shooter and FORS2 spectra. The measured V_{r} are corrected for heliocentric motion and local standard of rest motion for the dates of observation. These give local standard of rest velocities (V_{LSR}) of 47.2 ± 3.4, 45.3 ± 4.3, and 63 ± 7 kms^{-1} for PDS 27 X-shooter(a), X-shooter(b) and FORS2, respectively. Both X-shooter(a) and X-shooter(b) values are in agreement with each other, while there is a difference of $\sim 18 \pm 8$ kms^{-1} between X-shooter and FORS2. For PDS 37, the V_{LSR} is found to be 11.7 ± 5.5 kms^{-1} for X-shooter and 13.5 ± 8.0 kms^{-1} for FORS2. For the final V_{LSR} to PDS 37 an average of the X-shooter and FORS2 values is taken and this results in a V_{LSR} of 12.6 ± 4.8 kms^{-1}.

Both stars' spectra are variable. An illustration of this is provided in Fig. 3.2

in which Hα is shown at three observing epochs for PDS 27 and two for PDS 37. The line profiles are variable with a deeper absorption component when the emission is weaker. For PDS 27 the Hα line-to-continuum ratio ranges from 13 to 18, and the EW increases from -70.4 to -120.8 Å from the X-shooter(b) to the FORS2 data sets (with the X-shooter(a) observations lying in between). For PDS 37 the line-to-continuum increases from 19.5 to 24, and the EW from -111.4 to -122.6 Å. Vieira *et al.* (2011) observed, in 1990, an EW of -88 and -105 Å for PDS 27 and PDS 37 respectively.

Variability of the He I line in PDS 27 also occurs between all observations. Fig. 3.3 shows four of the He I lines, along with overplots from each observation epoch in order to highlight the variability. The He I lines 5875, 6678 and 7065 Å are present in both X-shooter and FORS2 spectra, while 10830 Å is covered only by the X-shooter observations. The 5875 Å line in the FORS2 data shows a broad blue absorption wing which is seen extending from -500 kms^{-1} towards the red, but it cannot quantified how far it extends into the red due to the Na I lines blending with it. In the X-shooter(a) data set a clear absorption line is seen centred at $\sim$-150 kms^{-1} from the rest wavelength. The line in the X-shooter(b) is difficult to measure, due to the blending mentioned, but it appears to be centred at $\sim$-100 kms^{-1}. The 6678 and 7065 Å lines show a similar behaviour in their velocities between the data sets, as demonstrated in Fig. 3.3. The 10830 Å line only shows a small variability in the strength of the line.

In the case of PDS 37, all the He I lines, present in both X-shooter and FORS2, show variability in the line centre of $\sim$50 kms^{-1} between them, with respective line centres being blueshifted from the central wavelength. Some of these show a very weak redshifted emission, which is seen to be much stronger in the 10830 Å

line. There is also strong variability in the line strengths, measured solely across the absorption component, where the strength is ∼2.5 greater in FORS2 than in X-shooter.

3.3.2 Interstellar Lines

The spectra of both targets contain interstellar absorption lines, most notably the K I doublet (7664.9, 7698.9 Å), Na I doublet (5889.9, 5895.9 Å) and the diffuse interstellar bands (DIBs); their origin comes from the material present in the interstellar medium (ISM). The K I doublet at 7664.9 Å is blended with a telluric line. The strength of the DIBs increases with the amount of material, and therefore reddening, along the line of sight (Jenniskens & Desert 1994). However, the DIBs can only provide a lower limit to the total reddening. Oudmaijer *et al.* (1997) found for a sample of young objects that the majority of the DIBs correlate with the reddening due to interstellar dust, but they remain insensitive to the dust in circumstellar envelopes and their parental molecular clouds. Eight well-known DIBs are clearly identified in both objects; the measured EW for each line, along with the line strength per unit *E(B-V)* determined from Jenniskens & Desert (1994), and the resulting *E(B-V)* are given in Table 3.1. The overall *E(B-V)* is found to be 1.2 ± 0.16 for PDS 27 and 0.98 ± 0.37 for PDS 37. The spread of the values is fairly large with *E(B-V)* ranging, for PDS 27 and 37 respectively, from a low of 0.99 and 0.48, for the 5780 Å line, to a high of 2.42 and 2.9, for the 5849 Å line. The very large colour excess derived from the 5849 Å DIB is not entirely unexpected as it was suggested by Chlewicki *et al.* (1986) that the strength of this DIB could provide a good indication of the total redden-

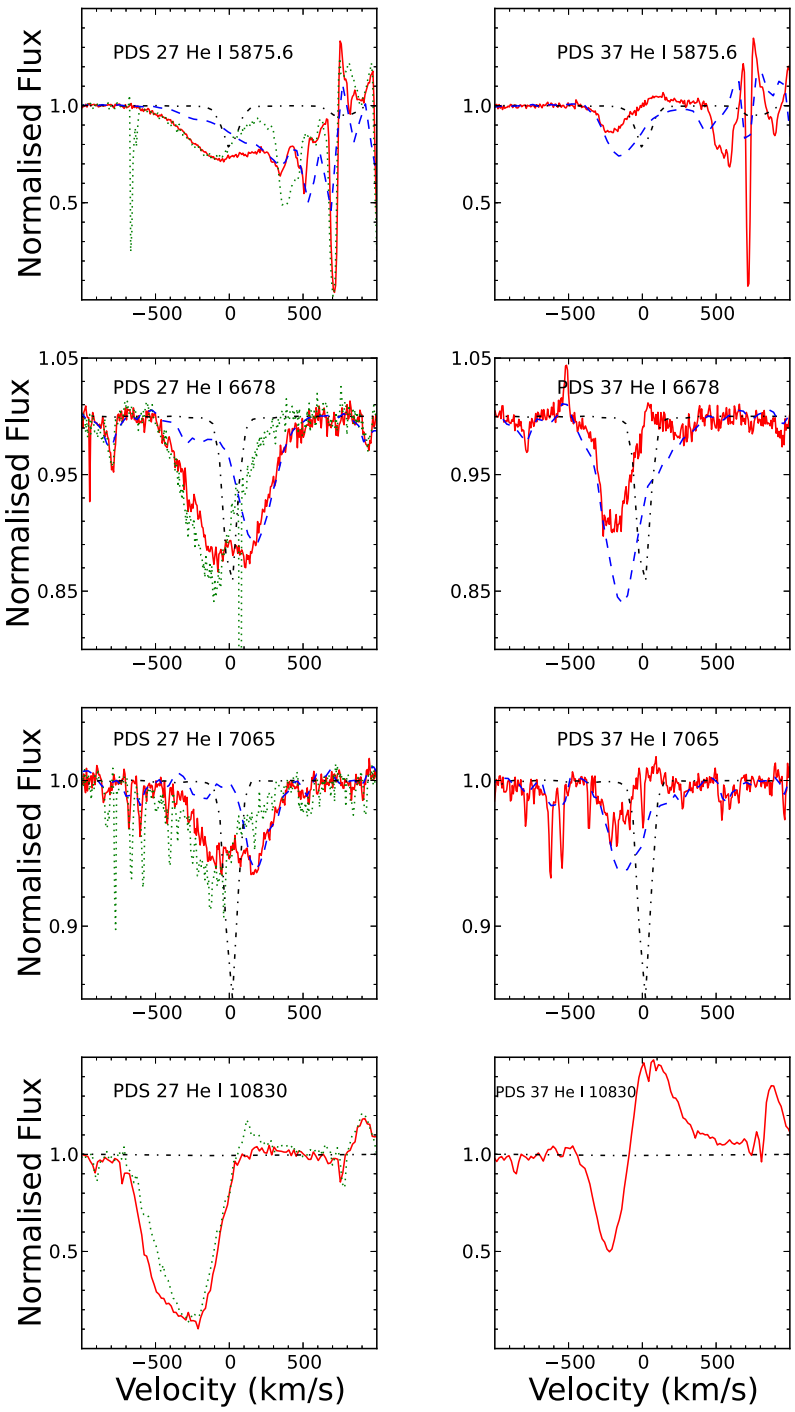

Figure 3.3: He I line variability is shown for PDS 27 of three observation epochs: FORS2 (blue dashed line) and two X-shooter epochs, X-shooter(a) (green dotted line) and X-shooter(b) (red solid line). For PDS 37, there is only one X-shooter data set (red solid line) and one FORS2 observation (blue dashed line). A KC model (black dash-dotted line) of temperature 21000 K is overplotted for the 5875, 6678 and 7065 Å lines, while for the 10830 Å line a black dash-dotted line shows just the continuum level. The lines are shifted to the rest wavelength of the stars as in Fig. 3.1.

Table 3.1: The observed EW and the *E(B-V)* values obtained from the DIBs. Errors in the EW and *E(B-V)* are typically 5%.

DIB	EW/*E(B-V)*	PDS 27		PDS 37	
		EW	*E(B-V)*	EW	*E(B-V)*
(Å)	(mÅ/mag.)	(mÅ)	(mag)	(mÅ)	(mag)
5780.6	579	571.5	0.99	278.9	0.48
5797.1	132	190.7	1.44	221.6	1.68
5849.8	48	116.4	2.42	139.4	2.90
6089.8	17	24.1	1.42	23.4	1.38
6204.3	189	230.8	1.22	129.0	0.68
6013.7	23	242.0	1.05	206.5	0.89
6660.6	51	61.8	1.21	46.9	0.90
6993.2	116	131.7	1.06	100.0	0.86

ing towards an object including the circumstellar component. This argument is strengthened by Oudmaijer *et al.* (1997) who found in their study that this DIB was an exceptional case which more accurately traced the total reddening for each star than any of the other DIBs. Therefore, in the overall *E(B-V)* reported above, the 5849 Å DIB is not included. The $V_{\rm LSR}$ of the DIBs is measured to be 26.6 ± 5.3, 27.3 ± 5.6 and 27.5 ± 2 kms^{-1} for PDS 27 X-shooter(a), X-shooter(b) and FORS2 spectra, respectively; all the values are in very good agreement with each other. This indicates that there is no variability and an extra check on the quality of the data. For PDS 37, the $V_{\rm LSR}$ is found to be 0.5 ± 2.8 and 6 ± 4 kms^{-1} for the X-shooter and FORS2 spectra, respectively. This is consistent with the $V_{\rm LSR}$ observed in the sharp absorption lines from Na I 5889.9 and 5895.9 Å, which is found to be 26.5 ± 1, 26.8 ± 0.3 and 26 ± 2 kms^{-1} for PDS 27 X-shooter(a), X-shooter(b) and FORS2 spectra, respectively, and -4.5 ± 0.5 and -5 ± 1 for PDS 37 X-shooter and FORS2 spectra, respectively. Fig. 3.4 shows three DIBs, Na I 5889.9 Å and K I doublet at 7698.9 Å in order to highlight the consistency between the observed interstellar lines.

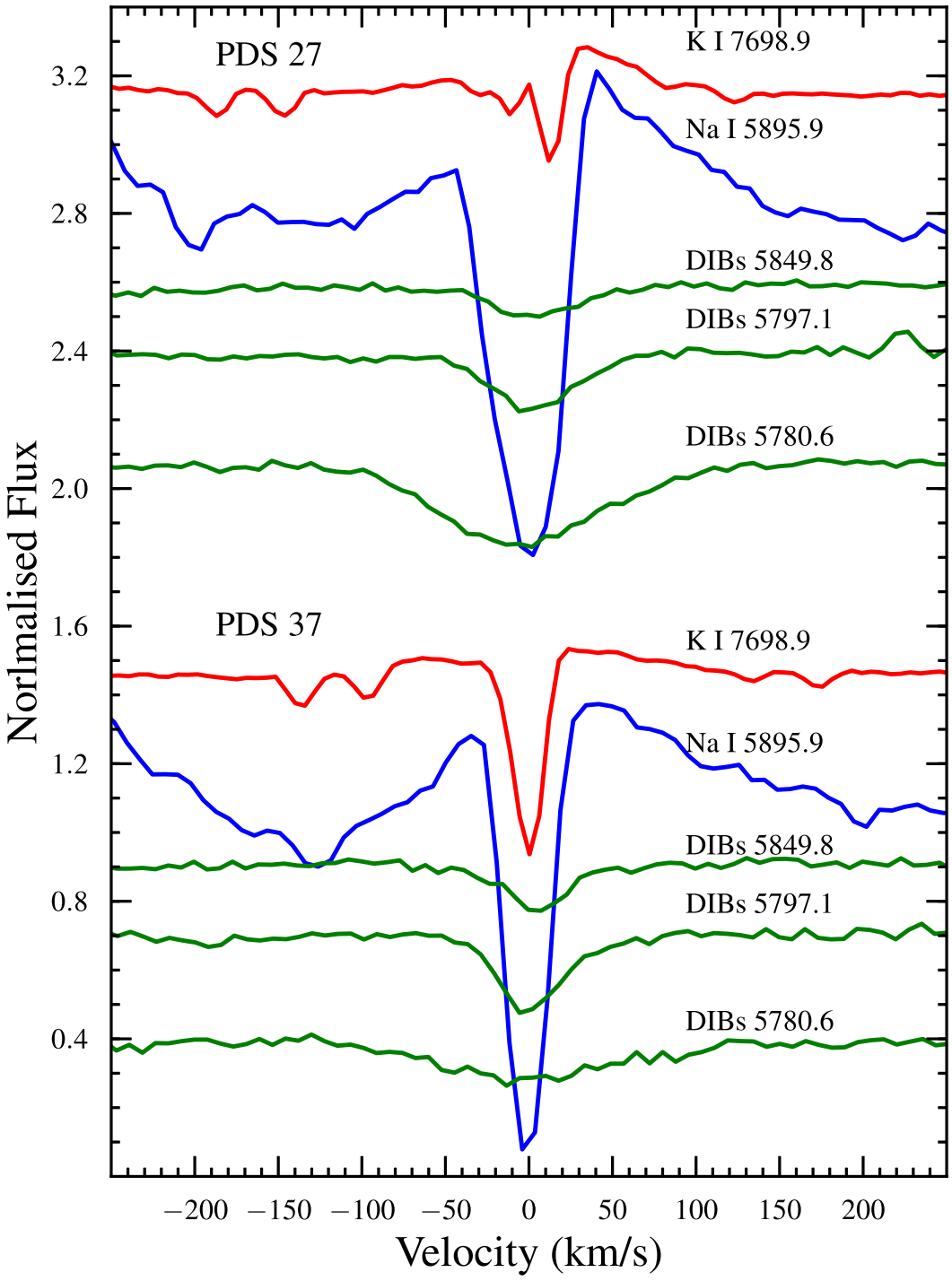

Figure 3.4: A selection of observed interstellar lines from the X-shooter data is shown for both targets (for PDS 27 only the X-shooter(b) data set is shown for clarity). For both targets, the red solid line denotes K I doublet at 7698.9 Å, while the blue solid line is Na I 5889.9 Å and finally the green solid lines are three DIBs line at wavelengths shown on the graph. The lines are shifted to the rest wavelength of the stars as in Fig. 3.1.

3.3.3 Continuum Polarisation

The continuum polarisation of the targets is shown in Fig. 3.5. In the figure, the spectropolarimetric data were rebinned using a coarse sampling, of ~ 250 Å per bin, to minimize errors. It can be seen that the percentage of polarisation increases from short wavelengths, peaks in the V band and then decreases towards longer wavelengths. The Serkowski law provides an excellent fit to the observed continuum polarisation for both objects. This combined with the large *E(B-V)* found towards these objects in Section 3.2 suggests that the bulk of the observed polarisation is indeed interstellar. The angle of polarisation changes slightly over the different bands; a change of 1 deg is observed for PDS 27 while a 5 deg change is observed for PDS 37. The polarisation angle normally does not change as a function of wavelength for the ISM. The slight change in position angle with wavelength indicates that there is a contribution from another polarising agent to the total polarisation.

3.3.4 Line Spectropolarimetry

The polarisation spectra around the strongest lines, Hα, Hβ and the calcium triplet are displayed in Fig. 3.6. There is a clear change in polarisation across the Hα line in both objects. The red peak and, where visible, the blue peak have almost the same polarisation value as the continuum, while there is a strong change across the absorptive component in both polarisation spectra and the (Q,U) plots. The shift in the polarisation from continuum to the line is of the order of 1% for PDS 27 and 1.6% for PDS 37.

Fig. 3.6 also shows that there is no clear change in the polarisation spectra

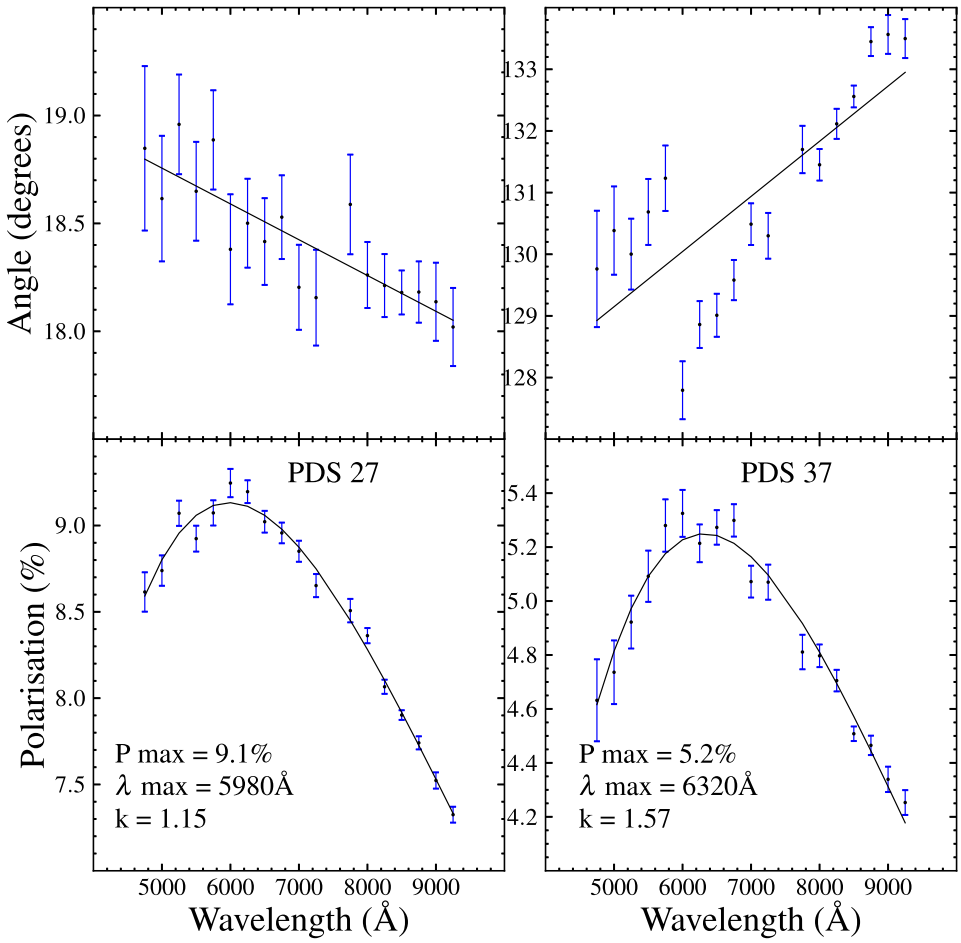

Figure 3.5: The polarisation and polarisation angles as a function of wavelength for PDS 27 and PDS 37. The spectropolarimetric data were coarsely sampled to improve the error bars. The black lines denote the best-fitting Serkowski law to the data.

across Hβ for both targets. Several different ways of rebinning the data were tried, but no compelling evidence for line effects across Hβ could be found.

The Ca II triplet has a lower ionisation potential than the Hα line, and as such it originates in a different region at a larger distance from the central stars. I did not detect any line effect across the Ca II triplet in PDS 27, whereas in PDS 37, the first two data sets show a possible line effect while the second two data sets do not show such a line effect (see Fig. 3.6). Therefore, the current data are not

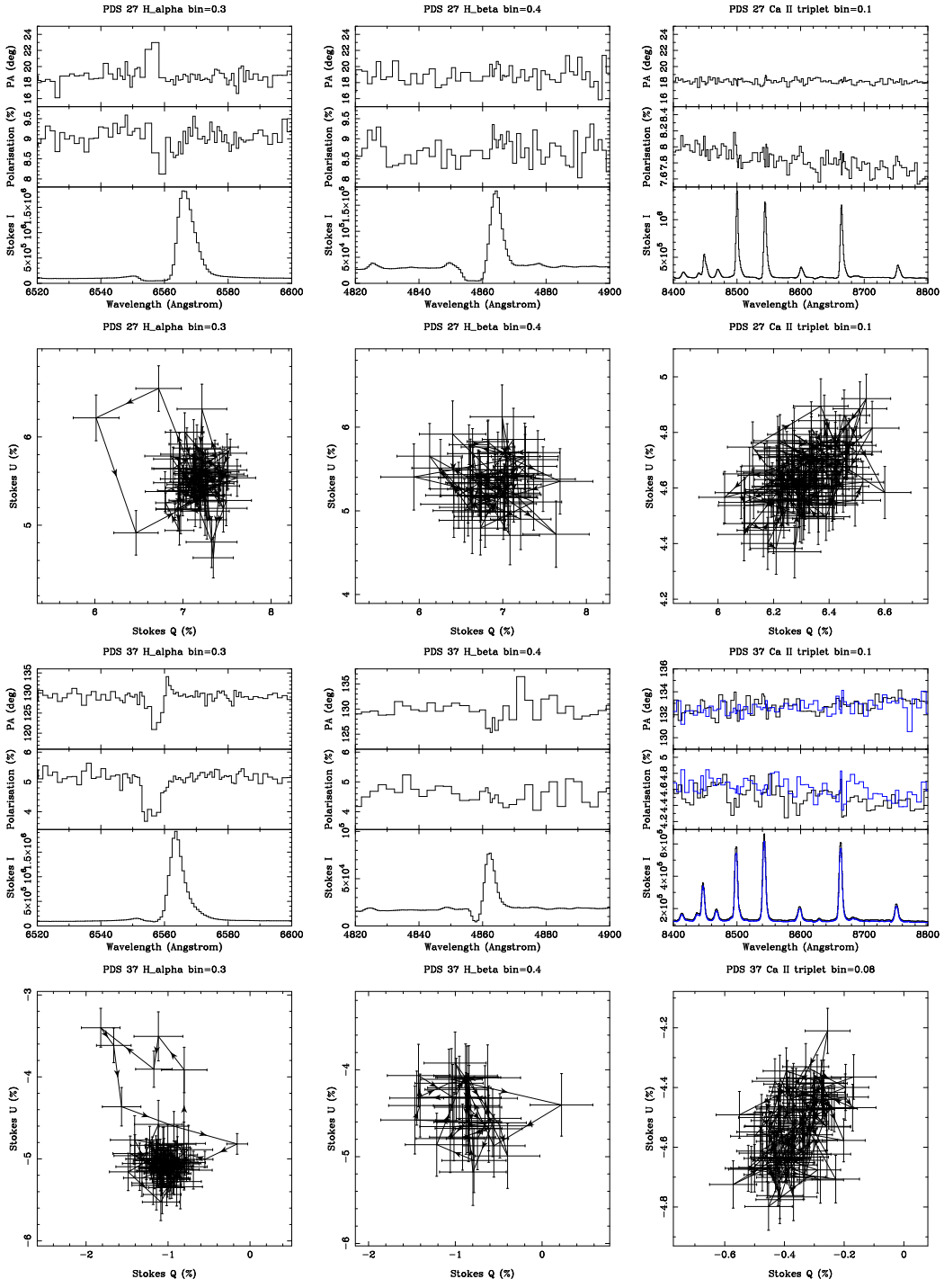

Figure 3.6: The polarisation data of PDS 27 (upper half) and PDS 37 (lower half) are shown here. The data are presented as a combination of triplots (top) and (Q, U) diagrams (bottom). In the triplot polarisation spectra, the Stokes intensity (I) is shown in the lowest panel, polarisation (%) in the centre, while the position angle (PA) is shown in the upper panel. The Q and U Stokes parameters are plotted against each other below each triplot. The data are rebinned to a constant value, as indicated at the top of each plot. The Ca II triplet in PDS 37 is presented in two colours: the first two data sets with possible line effect are shown in black solid line; the second two data sets with no line effect are shown in blue solid line.

Table 3.2: The line spectropolarimetry results: columns (2), (3), (5) and (6) list the Stokes (I) characteristics; columns (4) and (7) list line spectropolarimetry characteristics of each target. Errors in the EW measurements are typically 5%.

Lines	PDS 27			PDS 37		
	EW (Å)	Line/cont.	Line effect	EW (Å)	Line/cont.	Line effect
Hα	-120.80	18.0	Yes	-122.60	19.4	Yes
Hβ	-14.56	5.8	No	-12.27	4.5	No
Ca II(8498)	-24.05	6.0	No	-22.66	4.4	–
Ca II(8542)	-23.97	5.3	No	-25.43	5.1	–
Ca II(8662)	-22.78	5.2	No	-23.12	4.8	–
Ca II(8912)	-1.11	1.2	No	-0.81	1.1	No
Ca II(8927)	-1.79	1.3	No	-1.69	1.3	No
He I(6678)	0.90	0.9	No	1.40	0.8	No
He I(7065)	0.27	0.9	No	0.52	0.9	No
[O I](6300)	-0.36	1.1	No	-0.46	1.2	No
Fe II(6456)	-3.14	1.8	No	-2.07	1.5	No

sufficient to confirm whether there is a line effect or not across the Ca II triplet in PDS 37. I do not detect changes across any other lines in this polarimetric spectrum, which includes the Ca II doublet, He I, [O I] 6300 Å and Fe II lines. The observed line characteristics of the targets in the FORS2 data are presented in Table 3.2, including an indication whether a line effect is present.

3.4 Analysis

3.4.1 Stellar Parameters

3.4.1.1 Stellar Velocity

Due to the lack of photospheric absorption lines in the spectra of both stars, the clean and symmetric Fe II and Ca II triplet emission lines were used to estimate the systemic velocity.

For PDS 27 I noted that in Section 3.1 both X-shooter observations provide a similar $V_{\rm LSR}$, while there is a difference of $\sim 18 \pm 8$ kms^{-1} in $V_{\rm LSR}$ between X-

shooter and FORS2. To examine the reliability of this variation, it is important to check the $V_{\rm LSR}$ of the interstellar lines as this should not vary over different epochs. In Section 3.2, a similar $V_{\rm LSR}$ was found of the DIBs in all epochs. These velocities are consistent with the $V_{\rm LSR}$ observed in the sharp absorption lines from Na I 5889.9 and 5895.9 Å. The observed variation in $V_{\rm LSR}$ of PDS 27 could be due to the star itself through changes in the circumstellar environment. On the other hand, it could be due to the presence of a second star in the system. Distinguishing conclusively between the two scenarios is challenging with only a few epochs of data, and requires additional observations. However, the line profiles are almost symmetric in all epochs; hence, it is more likely that the changes seen are due to binary motions and are not due to the movements of circumstellar material around the star. Based on the above argument, the stellar velocities for PDS 27 is not used for kinematic distance determinations.

For PDS 37, the $V_{\rm LSR}$ is consistent within the errorbars for the X-shooter and FORS2 data.

3.4.1.2 Distance

Accurate stellar parameters are required for any quantitative analysis to be made about either age, accretion or evolution for these two enigmatic objects. First the distance will be discussed, which will later help constrain the total luminosity.

Using a Galactic rotation curve an estimate of the distance to the stars can be made using the observed velocities. In this work, the rotation curve from Reid *et al.* (2009) is used. The observed $V_{\rm LSR}$ in PDS 27 is unlikely to trace the actual stellar velocity as argued in the previous section. Fortunately, molecular observations of ^{13}CO (1-0) and NH3 (1,1) towards these objects are available (Urquhart

et al. 2007, 2011). The molecular lines in this case trace the parental clouds in a larger volume around the star compared to the optical lines. These authors observe velocities of 43.5 and 5.4 kms^{-1} for PDS 27 and PDS 37, respectively. Using the molecular velocities the resulting kinematic distance for PDS 27 is 3.17 (+0.66, -0.62) kpc, while for PDS 37 the distance is found to be 3.67 ± 0.95 kpc. For PDS 37 the stellar lines can also be used; these provide distances of 4.53 ± 0.77 and 4.74 (+0.75, -0.90) kpc for the lines measured from X-shooter and FORS2, respectively. The molecular and spectral line measurements are in agreement with each other in PDS 37. For the final distance to PDS 37, an average of the three values is taken and this results in a distance of 4.31 ± 0.67 kpc.

An interesting consistency check is to see what the kinematic distances to the DIBs along the line of sight towards the objects are. This is because the DIBs trace the material between us and the star, and should therefore be closer than the stellar and molecular distances. The observed V_{LSR} velocities of the DIBs in Section 3.2 provide kinematic distances for PDS 27 of 1.76 (+0.58, -0.55) and 1.80 (+0.58, -0.55) kpc for the X-shooter and FORS2 data, respectively. For PDS 37 the kinematic distances of DIBs are found to be 2.59 ± 1.4 and 3.76 ± 0.92 kpc for the X-shooter and FORS2 data, respectively. These distances are indeed lower than the ones traced by the stellar and molecular lines, which is as expected.

3.4.1.3 Temperature

Spectral types of both stars are difficult to determine due to a general lack of photospheric absorption lines in the spectra. So far, the only spectral type given to these stars is by Vieira *et al.* (2003), who assign them both a tentative B2

classification based on their photometry.

A rough lower limit on the temperature can be found using the observed colour indices. Vieira *et al.* (2003) measure a $(B-V)_{obs}$ of 1.32 for PDS 27 and 1.52 for PDS 37. The DIBs provide colour excesses, $E(B-V)$, of 1.20 ± 0.16 and 0.98 ± 0.37 for PDS 27 and PDS 37, respectively. Combining the observed and excess colours allows an intrinsic $(B-V)$ to be derived. This is only a lower limit as the DIBs trace the ISM, but not necessarily the total extinction. The highest $(B-V)_{int}$ from the DIBs is found to be -0.04 in PDS 27 and 0.15 in PDS 37. This gives a lower limit to the temperatures which corresponds to B9-type star with a temperature of 10000 K and A5-type star with a temperature of 8000 K for PDS 27 and PDS 37, respectively. The stars are likely to be even hotter than this, as this is a lower limit.

An upper limit to the temperature can be placed using the Balmer jump in the spectra. This is because the Balmer jump decreases in size with increasing temperature (for temperatures greater than $\sim$ 9000 K, where the Balmer jump is at its maximum). The observed size of the jump therefore places an upper limit on the photospheric temperature. Moreover, a small jump can also be achieved by cooler stars combined with a flux excess due to accretion. The Balmer jump constraint provides an upper limit of 21000 K (see Fig. 3.7). In the figure, the observed Balmer excess for each star is shown for different temperatures, beyond 21000 K no excess can be observed.

The DIBs and Balmer jump constraints give an effective temperature range of 8000 K/10000 - 21000 K. In addition, the observed lines from the two objects suggest that they lie more towards the upper temperature limit. N I emission lines at 8629 and 8683 Å are seen in both objects. These lines have a high

excitation energy (∼10 eV), and have only been observed in B-type HAeBe stars, predominately early types (Hamann & Persson 1992). Given that the latest spectral type in which these authors detected both N I emission lines was B6 (corresponding to 14000 K), a revised lower limit of around 14000 K is inferred to the temperatures of PDS 27 and PDS 37 .

Based on the above three arguments, which combine knowledge of photometry and spectra, the most plausible range to the temperatures is found to be 14000 – 21000 K. A temperature of 17500 ± 3500 K is adopted for both objects.

In addition, the only absorption lines that are present in both spectra are from He I. If their origin were assumed to be from the photosphere, then their strength would peak at around 21000 K. However, the observed strengths are greater than predicted from stellar model atmospheres, and they are asymmetric. The blueshifted absorption extends all the way to -500 kms^{-1} and covers the same velocity range as the hydrogen lines. Therefore, an additional contribution to the absorption could be due to a strong wind. Although strong absorption has been regularly observed for T Tauri stars in the He I 10830 Å line, such a strong and broad absorption in a wind is not expected in the higher energy transitions of He I in classical T Tauri stars (CTTs) by either theory (Kurosawa *et al.* 2011) or observations (Beristain *et al.* 2001). This suggests that the stars are much hotter than CTTs, which is in agreement with the other temperature constraints adopted.

3.4.1.4 Other Stellar Parameters

With a limit on both distance and temperature established for the stars, other stellar parameters were found. A start will be made with determining the lu-

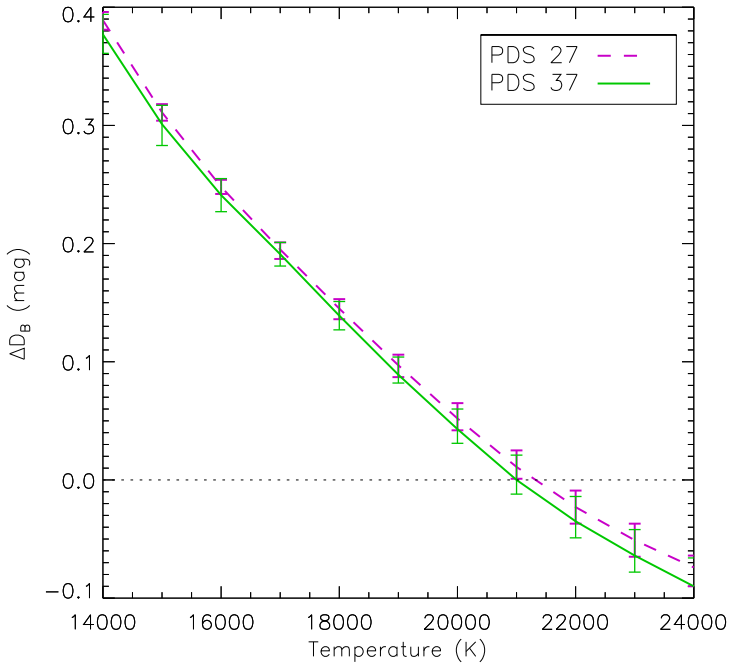

Figure 3.7: The measured Balmer Excess changes for each star depending upon the adopted temperature. PDS 27 is represented by the magenta dashed line, and PDS 37 by the green solid line. For both stars a zero Balmer Excess is measured around 21000 K. Figure by Fairlamb (Fairlamb 2015, PhD thesis; Ababakr *et al.* 2015).

minosity using the previously observed optical photometry. The Kurucz-Castelli (KC) models of 17500 K are used which provide a surface flux density. The observed photometry is then dereddened until their shape matches the slope of the KC model for the adopted temperature. To fit the models to the photometry, a scaling factor must be applied, as the models used are in surface flux while the photometry is observed flux. This scaling factor is just a ratio between the distance and radius squared, $(D/R)^2$. Fig. 3.8 shows the result of dereddening the photometry and a 17500 K KC-model fit to the data The luminosities are then calculated as a sum of the scaled KC model flux multiplied through by the

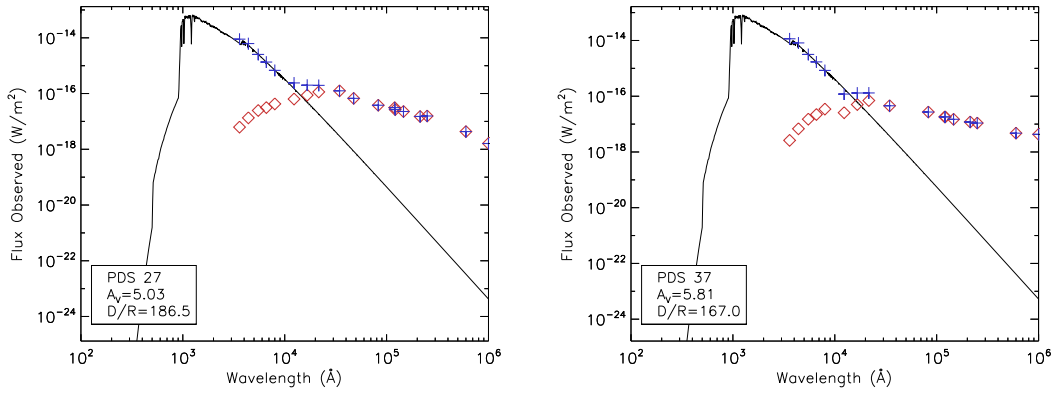

Figure 3.8: An example of the SED integration for extracting a dereddened total flux for the case of PDS 27 (left) and PDS 37 (right). The red diamonds are the observed photometry, the blue crosses are the dereddened photometry and the solid black line is a KC model of 17500 K. Figure by Fairlamb (Ababakr *et al.* 2015).

distances found previously. Taking into account the errors on the distance and temperature, the luminosities are calculated to be $\log(L_*/L_\odot) = 4.39 \pm 0.40$ for PDS 27 and $\log(L_*/L_\odot) = 4.75 \pm 0.39$ for PDS 37.

With the luminosity established for each star, along with a well-defined temperature limit, the calculation of remaining stellar parameters through the use of PMS tracks can be performed. In this work, two sets of PMS tracks are adopted: one set by Siess *et al.* (2000), as they cover up to 12 $M_\odot$, and the other set from Bernasconi & Maeder (1996), as they cover a larger luminosity and mass range (these are the 15 and 25 $M_\odot$ tracks in Fig. 3.9). Along each mass track, there is a unique relation between the luminosity and temperature. Fig. 3.9 shows where PDS 27 and PDS 37 lie on the PMS tracks. Based on their position, a mass of 15.3 (+5.4, -4.4) $M_\odot$ and 21.1 (+11.0, -5.3) $M_\odot$ is found for PDS 27 and PDS 37 respectively.

The radius is found straightforwardly from the D/R values, determined in the

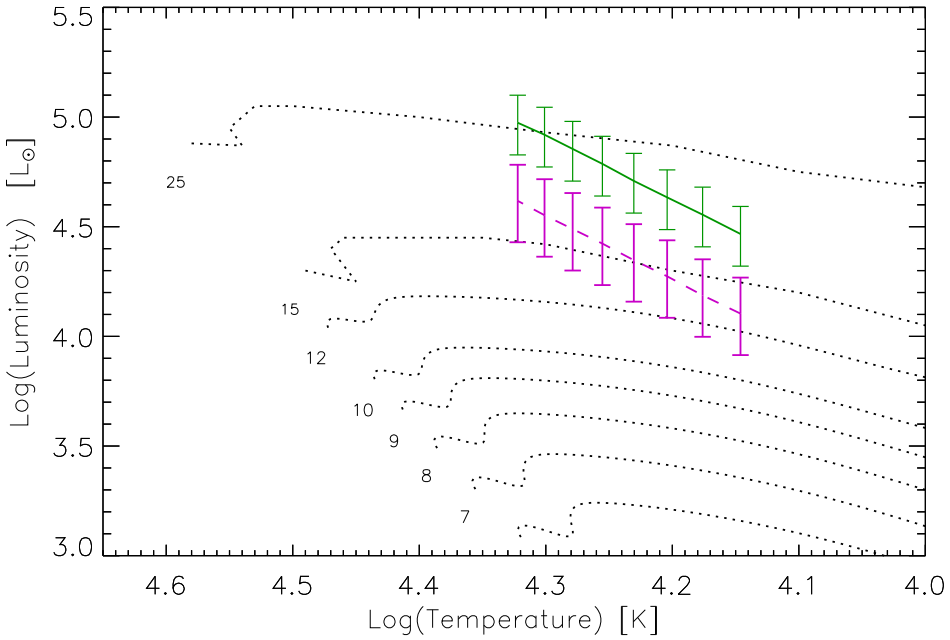

Figure 3.9: Shows the PMS tracks of Bernasconi & Maeder (1996) (15 and 25 $M_{\odot}$ tracks) and Siess *et al.* (2000) (up to 12 $M_{\odot}$ track), along with the positions of PDS 27 in magenta dashed line and PDS 37 in green solid line. The lines show where the objects lie for the determined temperature range, while the error bars show the allowed changes in luminosity given the errors in distance. Figure by Fairlamb (Ababakr *et al.* 2015).

previous section, by using the distance. This provides 17.0 ± 4.0 $R_{\odot}$ for PDS 27 and 25.8 ± 5.0 $R_{\odot}$ for PDS 37. With a mass and radius determined, the log(g) is calculated to be 3.16 ± 0.27 for PDS 27 and 2.94 ± 0.35 for PDS 37. The errors in log(g) are dominated by the errors in distance. The position of the stars in the HR diagram suggests that they are very young objects, which may be evolving into massive O-type stars.

3.4.2 Interferometric Results

As seen in Fig. 3.8, both objects show a significant near infrared excess, in fact the brightness of the extended dust and the star is almost the same in H band. On the other hand, the spectropolarimetric results, strongly suggest the presence of a circumstellar disk very close to the stars. Although the SED provides useful information about the presence of the dust in the circumstellar environment, its interpretation is challenging. Another technique is needed with high angular resolution to directly trace these inner regions.

The key point to understand the spatial scale of these two objects relies on the spatial resolution. The spatial resolution in radians of an instrument operating at a wavelength (λ) is given by:

$$\Delta\theta = 1.22\frac{\lambda}{D} \tag{3.1}$$

Where D is the diameter of the instrument. According to this equation the angular resolution of the VLT (8.2 m), at near infrared H band wavelengths ($\sim$ 1.65μm), is 50 mas. For a typical distance of massive stars, $\sim$ 1 kpc, this corresponds to a linear size of 50 au. This limits the observations of the very inner part of the circumstellar environment. Instead of building a large telescope, interferometer can be be used to achieve high angular resolution by combining separate light beams from several telescopes. Since the performance of an interferometer depends on distance between telescopes, baseline (B), its angular resolution increases significantly compared with a single dish telescope. A resolution of $\sim$ 1.5 mas, $\Delta\theta = \frac{\lambda}{2B}$, B=130 m, can be achieved with the PIONIER near infrared interferometry at the VLTI for the same above example. Thus increasing the

resolution by ~ 30 times. Because of the nature of light, combining beams from different telescopes results in observing constructive and destructive interference fringes. Analysing these fringes provides information about the spatial scale of observed objects. The fringe contrast or visibility amplitude is given by the following equation:

$$V = \frac{I_{max} - I_{min}}{I_{max} + I_{min}} \tag{3.2}$$

Where I_{max} and I_{min} are the maximum and minimum intensity of the fringes, the value of visibility amplitude is between 0 and 1. If V = 1, $I_{max} = 1$ and $I_{min} = 0$, then the object is unresolved (point source) which means the source emits coherent radiation. In contrast, if V = 0, $I_{max} = 1$ and $I_{min} = 1$, then the object is completely resolved (extended source). The value of the visibility varies between 0 and 1 as it is measured with different baselines, the visibility decreases towards longer baselines. Another observed quantity is the closure phase. The closure phase is the ratio of symmetric and asymmetric flux of the targets, a non zero closure phase means that there is asymmetry in the observed flux. This asymmetry in flux could be due to the presence of an inclined disk or unequal brightness binary (in case of binary system). For a binary system the closure phase in radians is roughly of the same order of magnitude as the inverse of flux ratio.

Here, the results of the near infrared PIONIER data are presented in Fig. 3.10. By looking at the observed visibilities and closure phases, a number of indicative clues can be seen to understand the nature of the surrounding environment of the objects. The observed visibility for both objects, even in the smallest baseline is

not equal to one, which indicates that either the objects are not point sources but extended or they are a member of a resolved or unresolved binary system at the resolution of our data. In addition, the visibility oscillates especially in PDS 37, this could suggest that the objects have a possible companion. Another way to look at the circumstellar environment is the observed closure phase. The observed closure phase is around $3\pm3^{\circ}$ and $5\pm2^{\circ}$ for PDS 37 and PDS 27 respectively. PDS 37 shows a large uncertainty in the closure phase but a non zero closure phase in PDS 27 is seen, which could suggest that the object is part of a binary system.

First let us see what kind of visibility is expected from a binary system. Fig. 3.11 shows a few examples of how the visibility of a point source binary system looks like for different separations between the two components and the flux ratios. From the figure, it can be seen that the visibility has a typical oscillation structure. The main two parameters in modelling the visibility of a binary are the separation between the two components and their flux ratio. The frequency of the oscillation depends on the separation, it increases with the separation, while the flux ratio controls the amplitude of the oscillation, which is at maximum when the flux ratio is 1. Now, let us assume that both objects are extended. Fig. 3.12 shows a modelled visibility of a resolved binary (right) and a uniform disk (left) for comparison. The visibility of a resolved binary appears as a modulation of a uniform disk.

3.4.2.1 Modelling the Visibility

I fit the observed visibility of both objects with different models including: uniform disk and binary system with and without circumstellar disks.

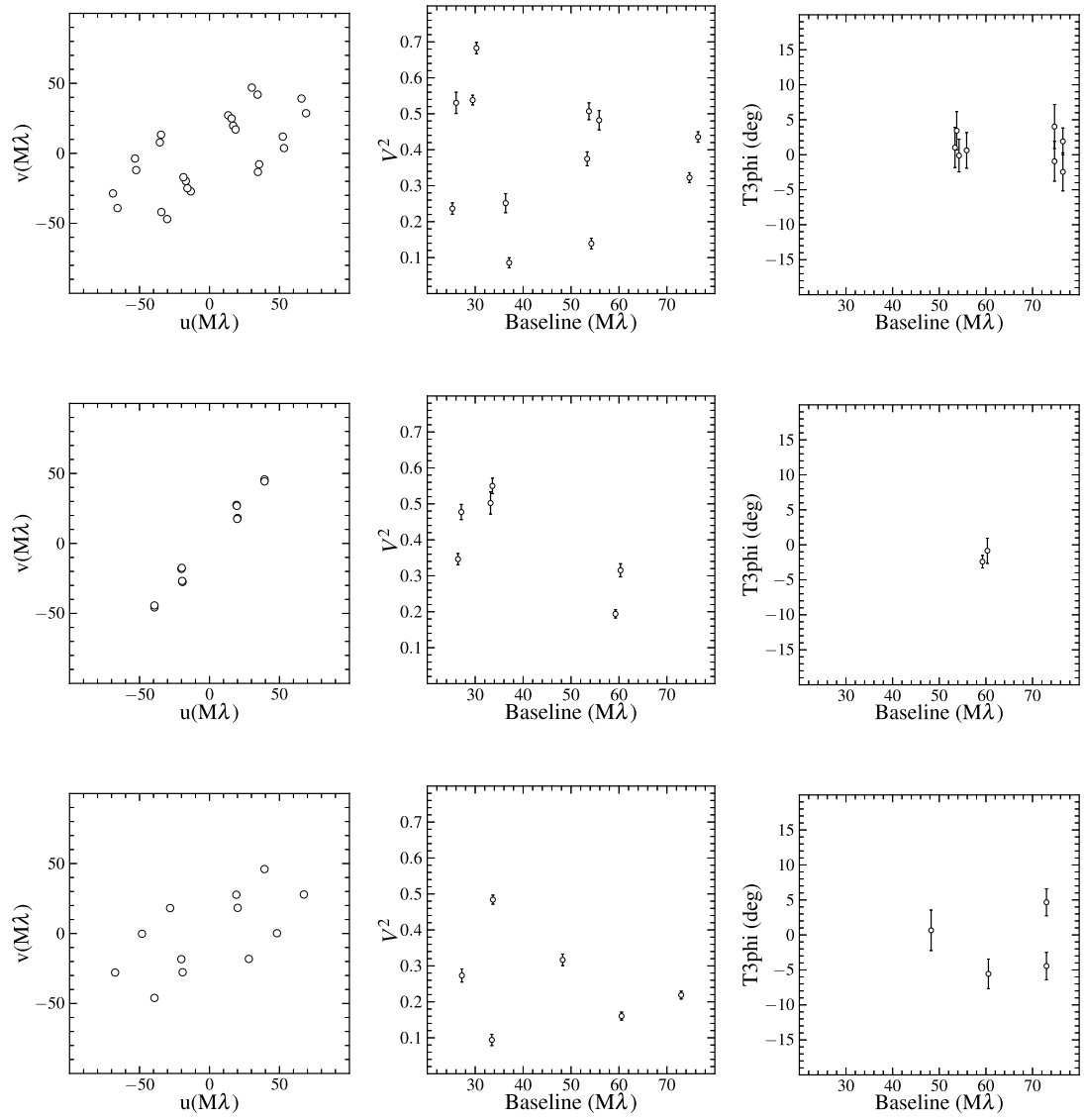

Figure 3.10: uv coverage, visibility and closure phase: upper panels are PDS 37 while the middle and bottom panels are PDS 27(1) and PDS 27 (2) respectively.

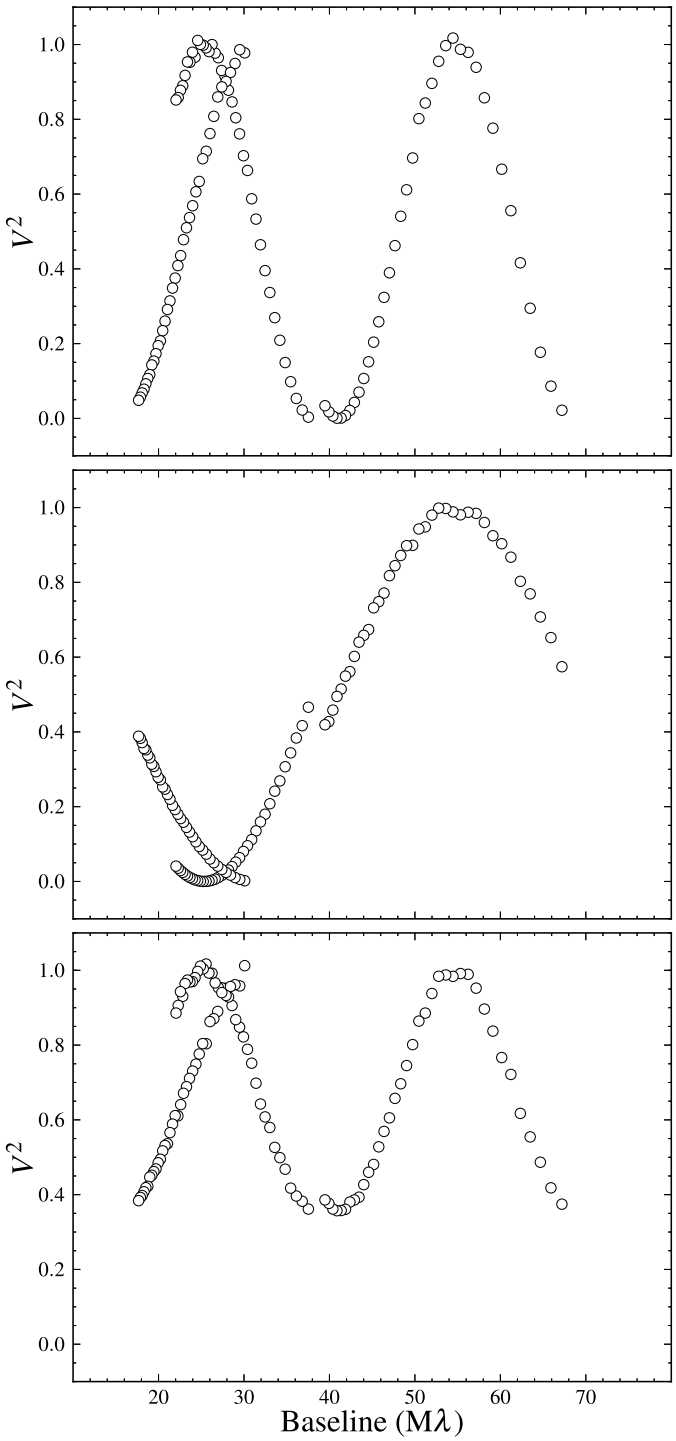

Figure 3.11: Examples of the visibility of a binary system for different separations between the components and the flux ratios. The figures were made using Aspro and for simplicity the AMBER interferometry is used with three baselines at 47, 57 and 102 m. The uppermost image represents an expected visibility of a binary that has a separation of 10 mas between the components and the flux ratio of 1:1, in the middle image the separation is 5 mas and the flux ratio is 1:1. The lowermost, the separation is 10 mas and the flux ratio is 0.8:0.2

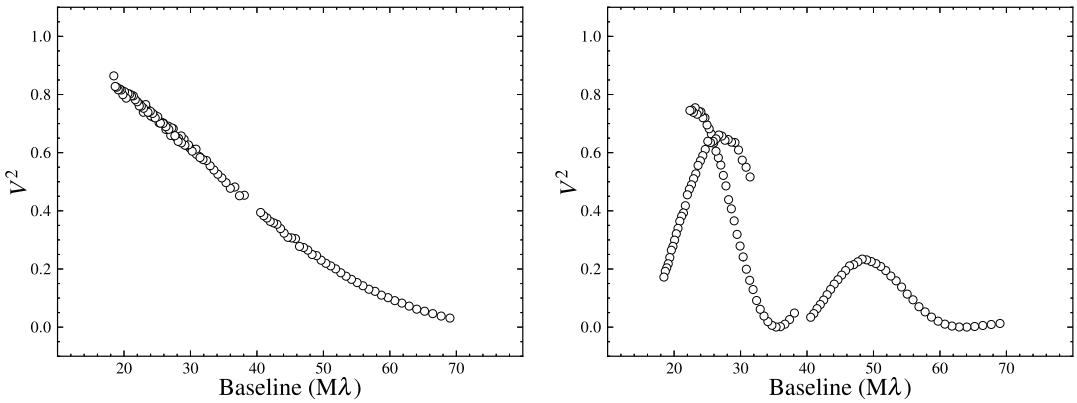

Figure 3.12: Left: the visibility of a uniform disk of a diameter of 3 mas. Right: the visibility of a binary whose components have a disk of a diameter of 3 mas with a flux ratio of 1:1. The visibility appears as a modulation of a uniform disk.

PDS 37

The visibility of PDS 37 shows that the object is resolved, and it also shows a sinusoidal shape. LITpro, which is a model fitting program, is used to fit the observed visibility. The program provides a number of models to fit the visibility.

To begin with, I first show a uniform disk model for a single object. The parameters that need to be constrained are the angular diameter of the disk and the flux ratio (star:disk). The best fit is shown in the top panel of Fig.3.13. The disk diameter in this model is 7.3±1.3 mas and the flux ratio is $1.38^{+6.85}_{-1.38}$. It is clear from the figure that there is a poor agreement between the data and the model. The high value of reduced χ^2 of 140 is another indication that the fit did not work. In addition, the flux ratio is poorly determined as it has very large uncertainties.

Now we consider fitting the data with a point source binary model without circumstellar environment. The parameters that need to be constrained are the

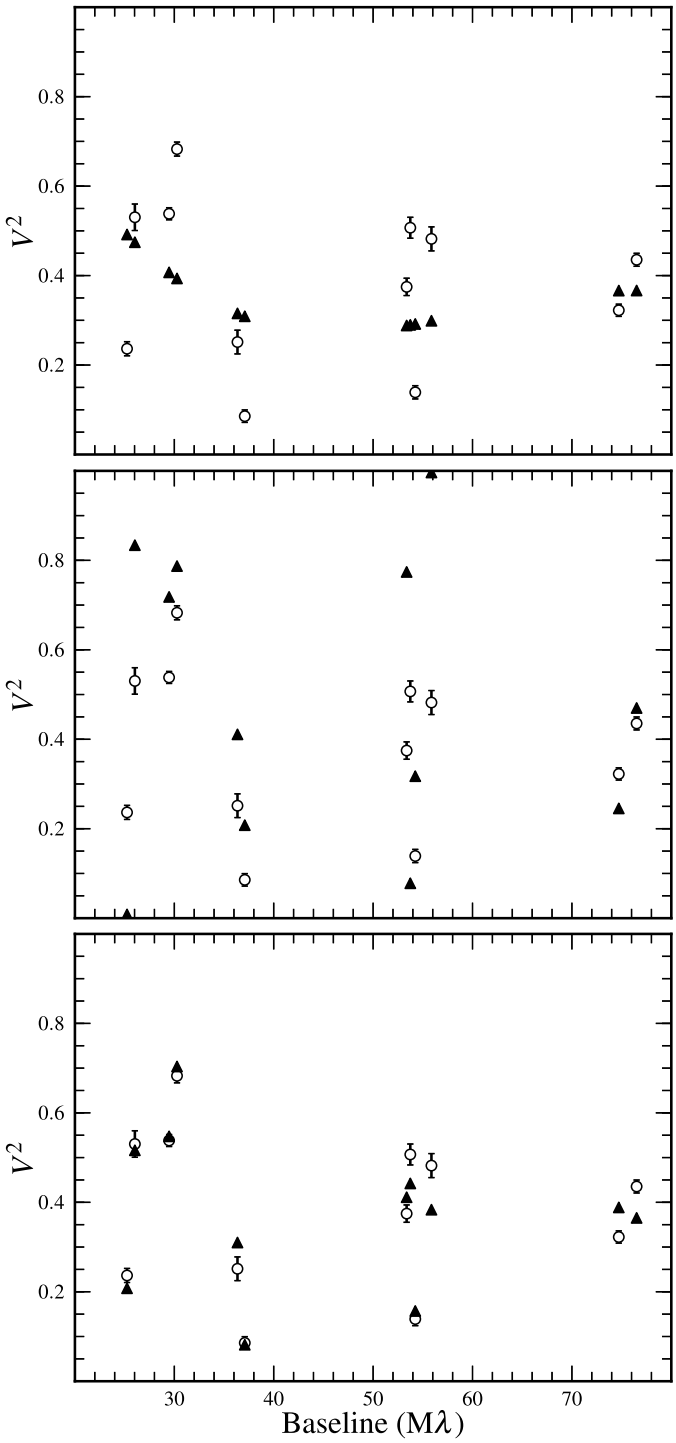

Figure 3.13: Three different models are compared with the observed visibility of PDS 37. The black circles with vertical error bars are the observed data while the solid black triangles represent the best visibility fit. Upper image is the best fit of a uniform disk model to the data. Middle image is the best fit of a point source binary model to the data. The bottom image represents the best fit of a binary model with a resolved primary object.

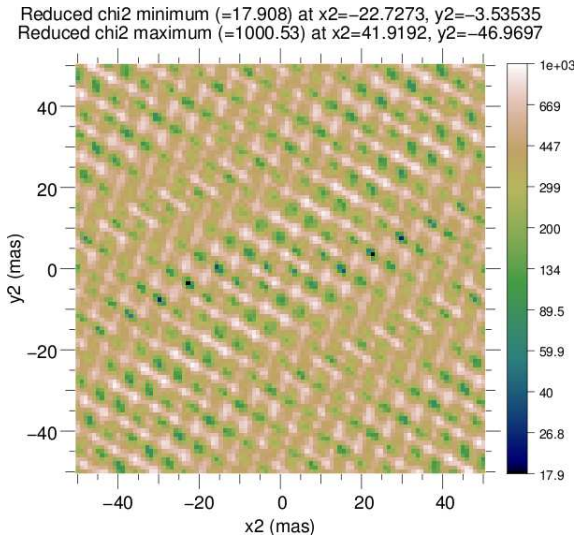

Figure 3.14: Reduced χ^2 map of the position, x2 and y2, of the secondary companion. The minimum and maximum value are shown at the top of the figure. There are two symmetrical minima to the origin which introduce an ambiguity of 180° in the PA of the binary.

position of the second component in x and y directions which constrain the separation and the position angle; and the flux ratio star1:star2. The best fit is shown in the middle panel of Fig.3.13. Again the fit shows a poor agreement with the observed data. However, in this case the general shape of the measured visibility is in good agreement with the observed visibility as both show a rippled structure. The above two models give a good indication that PDS 37 is possibly a binary star with one or both objects being resolved. Finally, we consider a binary system with one or both objects resolved. The added complication of this situation, is the large number of variables. For simplicity, I considered two stars with a disk and I fixed the position of one object and the disk at the origin and let the position of the second object to be free. This will give two possible results depending on the position of the secondary object and the diameter of the disk. The two possible results are a binary system with a circumstellar disk around both components or

a disk around one object and a point source companion. The result for a binary and a disk around one object is shown in the lower panel of Fig.3.13. The figure shows that the model is able to better fit the visibility, $\chi^2 \sim 14$, than the previous two models. The best fit provides the following parameters: the normalised flux of $0.535^{+0.578}_{-0.535}$, $0.135^{+0.151}_{-0.135}$ and $0.33^{+0.36}_{-0.33}$ for primary object, secondary object and a disk around the secondary object respectively; the diameter of the disk is estimated to be 4.56±0.54 mas; the position of the secondary object is set on x2=-22.47±0.23 mas, y2=-3.77±0.27 mas from the primary object. Although the fit of the model is in fairly good agreement with the data, the uncertainty in the flux ratios is large. I created a χ^2 map as a function of the position of the secondary object which is shown in Fig. 3.14. From the figure, it can be seen that there are two symmetric minima relative to the origin. This means that the solution is either x2= -22.7 mas and y2= -3.5 mas, which corresponds to PA of 260°, or x2= 22.7 mas and y2= 3.5 mas, which corresponds to PA of 80°. In order to remove this ambiguity of 180°, the closure phase needs to be considered which is sensitive to the PA of the binary. Unfortunately, the quality of the closure phase measurement for PDS 37 is not good enough to remove this ambiguity.

PDS 27

For PDS 27, the same procedure was followed as for PDS 37. The results of a disk model and a binary model with one of the companion being resolved, are presented in Fig. 3.15, the left images are the disk model and the right images are the binary model with one object being resolved. The upper images are PDS 27(1) while the middle images represent PDS 27(2) and both data sets are shown in the bottom. The Figure shows that there is a poor agreement between the

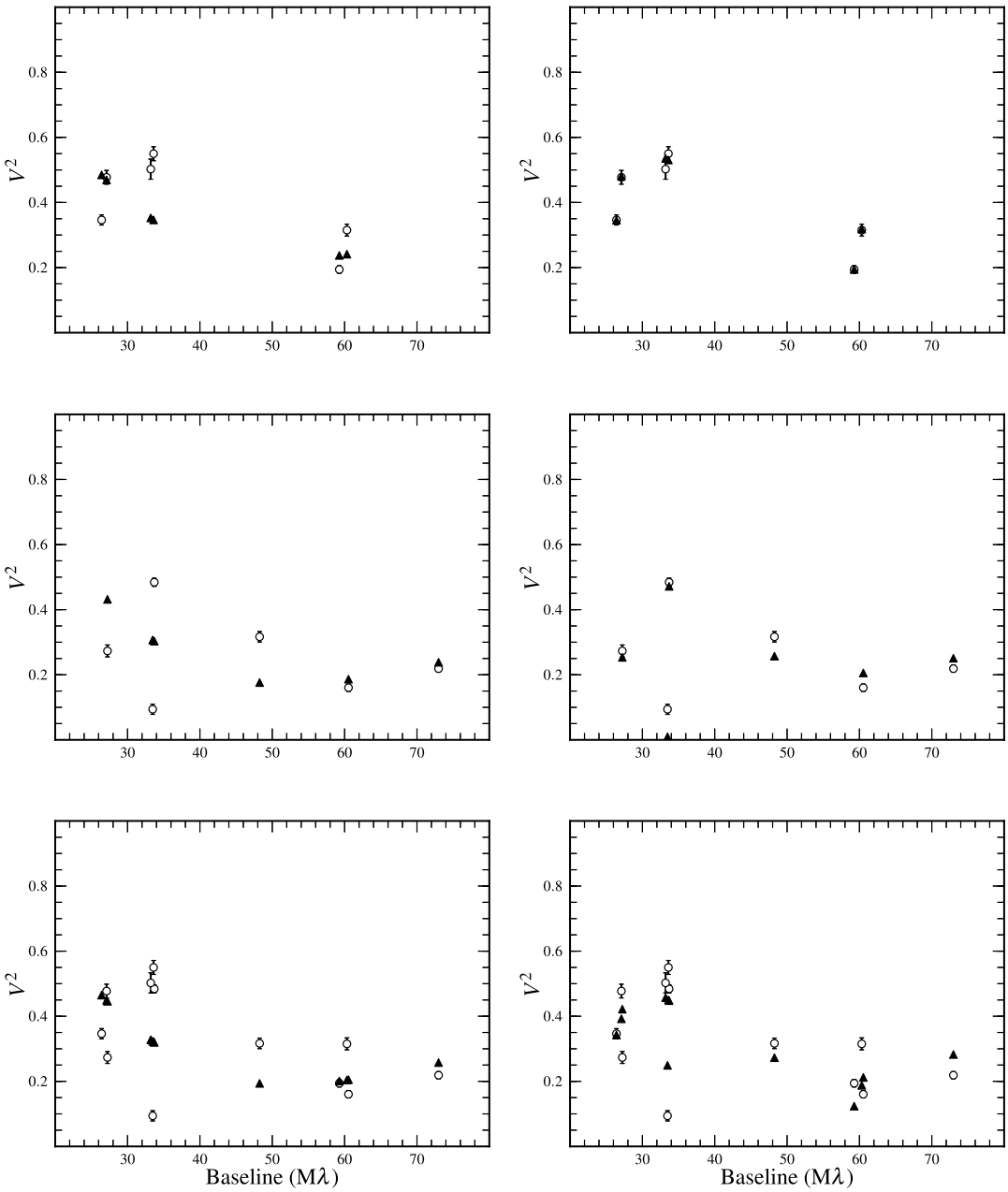

Figure 3.15: Two different models are compared with the observed visibility of PDS 27, uniform disk model (left) and resolved binary model (right). The black circles with vertical error bars are the observed data while the solid black triangles represent the best visibility fit. Upper images represent PDS 27(1), PDS 27(2) is shown in the Middle while both data together are shown in the bottom images.

observed visibility and the disk model. In contrast, the binary model provides a good fit to the observed visibility for the individual data. The position of the companion is found to be x2=87±0.5 mas and y2=37±0.5 mas. The best fit is also indicates a disk of a diameter of 6.3±0.2 mas around the primary object. The flux ratio has a large uncertainty which is comparable to the value itself. The reduced χ^2 of the position of the companion is 1.5, 22, 35 for PDS 27(1), PDS 27(2) and both data together. The χ^2 map shows only a single global minimum for PDS 27(1) while for the PDS 27(2) and both data together, there are several local minima. This is a degenerate problem where several combinations of x and y lead to the same result. Therefore, the available data are not sufficient to constrain all the parameters. The degeneracy can be broken by obtaining more data. The non zero closure phase seen in PDS 27 is another good indication of the presence of a companion but it also could be due to an inclined disk.

Overall, there are a number of clues to understand the nature of the objects by qualitatively looking at the data. The observed oscillations in the visibility, especially in PDS 37 is a good indication of the presence of a binary system. The non zero closure phase again suggests an asymmetry in the observed flux. It seems that the binary model with one extended object is the best model to represent the observed data. However, the available data can not constrain all the parameters due to the degeneracy problem.

3.5 Discussion

I have presented a spectroscopic, spectropolarimetric and interferometric study of two early-type Herbig stars. The spectra of both objects are remarkably similar,

strongly suggesting that both are in the same evolutionary phase. The spectra are dominated by strong emission lines, and do not reveal any photospheric absorption lines. Indeed, the only lines that are fully in absorption are the interstellar DIB lines.

The picture that emerges is that both objects undergo strong winds as attested by the clear, and numerous, P Cygni profiles observed. P Cygni absorption extends in both stars to hundreds of kms^{-1}. The He I line at 10830 Å is the only helium line seen as a P Cygni profile. The remaining He I lines at 5875, 6678 and 7065 Å are present only in absorption (see Fig. 3.3). These lines are broader than the expected intrinsic lines from the photosphere. If they originate from the wind, they must probe the very hot inner wind.

3.5.1 Circumstellar Geometry

The majority of the observed Fe II lines are double peaked in PDS 37, while they are single peaked in PDS 27 (see Section 1.3.1). This suggests that PDS 37 has an inclined disc that we are viewing close to edge-on. This interpretation is supported by a high inclination angle being reported by Ilee *et al.* (2013), based on first overtone CO emission. In addition, the continuum polarisation shows a change in position angle with wavelength. The observed polarisation must have an intrinsic component as normally the interstellar polarisation angle is constant with wavelength. This change is stronger in PDS 37 than PDS 27 as illustrated in Fig. 3.5. Further information on the geometry of the circumstellar environment can be achieved by performing spectropolarimetry across the lines.

Both PDS 27 and PDS 37 show a strong McLean-type effect across the absorp-

tive component of Hα (see Fig. 3.6) and the change is as broad as the absorption. This indicates the presence of intrinsic polarisation which in turn implies that the ionised material around the star is asymmetrically distributed. The strength of the line effect in Hα is of the order of 1% in PDS 27 and 1.6% in PDS 37. This supports the idea that PDS 37 has a more inclined disc than PDS 27, as we would expect more intrinsic polarisation in a more inclined disc. The slope of the loop from the continuum to the line in the (Q, U) diagram represents the intrinsic polarisation for the continuum polarisation (see Fig. 3.6). The intrinsic continuum polarisation angle represents the electron scattering angle in the circumstellar medium. An intrinsic polarisation angle of $\sim 77^{\circ}$ and $\sim 56^{\circ}$ is determined for PDS 27 and PDS 37 respectively. The angle has been measured from the continuum to the line in the (Q, U) diagram in Fig. 3.6 (see the discussion in Wheelwright *et al.* 2011b also in Chapter 1).

The interferometric results also show that both objects have an extended circumstellar environment as seen from the observed visibilities. The angular size at which PIONIER is sensitive to can be determined. According to the Wien's law, $\lambda \mathrm{T} = 2.898 \times 10^{-3}$ m.K, the PIONIER wavelength range (1.533μm - 1.772μm) is sensitive to the thermal radiation of the dust at temperature range between 1500 to 2000 K. The angular distance of the dust from the star can be estimated according to the following equation.

$$d = \frac{R\star}{2} \frac{T\star^2}{T_d^2} \tag{3.3}$$

Where d is the distance of the dust from the star, $R\star$ and $T\star$ are the radius and temperature of the star and T_d is the dust temperature. Based on this equation,

the larger the star's radius and temperature, the larger the distance of the dust from the star. In contrast, the larger the distance of the dust from the star, the lower its temperature. The stellar radius and temperature for our objects, found in the previous sections are ∼17500 K and ∼20 $R_\odot$ respectively. For a dust temperature of 1500 K, an angular size of ∼ 6 au is estimated for our objects, which would correspond to the very inner parts of the circumstellar disk. The maximum angular resolution of the PIONIER at the measured distance of our objects is ∼ 5±1 and 6.5±1.0 au for PDS 27 and PDS 37 respectively. This suggests that the observed flux is not thermal emission in the inner region but it is scattered light from the outer disk.

3.5.2 Stellar Properties

Based on their position in the HR diagram, it can be inferred that both of the targets are young objects with an active circumstellar environment. This is evidenced by strong winds, with P Cygni absorption of around 90 and 80% of continuum level for PDS 27 and PDS 37, respectively, in Hβ, and also maximum respective velocities of ∼-700 and ∼-400 kms^{-1} measured in the Hα line; and variability in line strengths and velocities seen in both the hydrogen and the He I lines. In particular, PDS 27 has shown unusual variability in the He I lines where the velocity of the line centre and the line strength change dramatically between epochs. This type of variability in line strength has been observed previously in other objects by Kučerová *et al.* (2013), but an origin of the varying line strength cannot be reached with only three epochs of data. On the binary nature, PDS 27 also shows variability in the observed $V_{\rm LSR}$ between the X-shooter and FORS2

spectra. This could be due to the presence of a secondary companion. However, with only three epochs of data, the binary nature of PDS 27 can not be established conclusively; additional data are required to determine the frequency and magnitude of the velocity variations. Based on this observed velocity variation in the period of two years, the system is expected to be a close binary, less than 10 au. However, the interferometric results suggest that the second companion is about 300 au from the primary object, this could suggest that PDS 27 is in fact a triple system. Unlike PDS 27, PDS 37 did not show any variability in the observed $V_{\rm LSR}$ between the X-shooter and FORS2 spectra but the interferometric results suggest that the object has a companion at 100 au. Although the spectroscopic and interferometric results show indications of the presence of a companion in these two objects, further investigations are needed to confirm this. Studying the multiplicity of these two objects could help in better understanding them, in particular these two objects are optically visible even though they are massive, $\sim$20 $M_{\odot}$. Recent studies have shown that binarity has a significant impact on the evolution of massive stars (e.g. Sana *et al.* 2012). Sana *et al.* (2012) found that $\sim$70% of O-type stars have a close companion that interchange material with their primary objects. They also found that one third of the primary stars could eventually merge with their companion. In fact, the binary fraction is higher in massive stars than low mass stars (Chini *et al.* 2012).

3.6 Conclusions

This chapter presents new data on two previously poorly studied HAeBe candidate stars. By combining X-shooter spectroscopy and FORS2 spectropolarimetry,

our understanding of properties in the circumstellar environments and the stellar parameters of the stars themselves has improved. The main findings in this work are as follows:

- The targets are both hot 17500 ± 3500 K with a spectral type of around B2. When combined with their high luminosities, of $\log(L_*/L_\odot) \sim 4.5$, they are placed in a secluded area on the HR diagram where very young objects lie. They are swollen objects with large radii, 17.0 ± 4.0 and 25.8 ± 5.0 $R_\odot$, and large masses, 15.3 (+5.4, -4.4) and 21.1 (+11.0, -5.3) $M_\odot$, for PDS 27 and 37 respectively.

- Spectropolarimetric line effects are detected in the Hα line for both objects. This polarisation property is explained by the McLean effect; line photons are scattered into the line of sight, increasing the polarisation across the P Cygni absorption. The spectropolarimetry indicates that the circumstellar environment is of a flattened structure, likely a disc.

- No line effects are seen across lines other than Hα. This is consistent with the notion that the spectropolarimetric behaviour in both cases is due to the McLean effect. The effect requires a strong emission line filling in absorption and a line with great optical depth so that the scattered photons will dominate the polarisation. It appears that in the cases studied here, only Hα fulfils both requirements.

- Line variability is seen in both objects, which can be ascribed to an active circumstellar environment. Extreme line variability of the He I species is seen in PDS 27. In addition, PDS 27 also shows a variability in the observed

$V_{\rm LSR}$ between X-shooter and FORS2; this could be due to the fact that the system is binary.

- The PIONIER data suggest that both objects might have a companion as seen from the observed visibility. In addition, PDS 27 also shows a variation in the observed $V_{\rm LSR}$ suggesting a binary system. However, the interferometric results and velocity variations are not consistent, suggesting that PDS 27 could be a triple system but more data are required to confirm this.

To conclude this chapter: two young PMS stars are presented, whose spectral classification as early B-type is consistent with them belonging to the group of HAeBe stars. Their masses and locations in the HR diagram indicate that they will continue to evolve to become O-type stars. As they are optically bright, these stars provide important test beds to study the formation of the most massive stars. Their young age is further supported by their large radii and low surface gravities. These properties are typical of very young objects where their puffed-up envelope is still undergoing contraction and will shrink as it progresses towards the main-sequence (Davies *et al.* 2010).

Chapter 4

Statistical Spectropolarimetric Study of Herbig Ae/Be Stars

4.1 Introduction

One of the difficult questions in the field of star formation is, at what spectral type, the accretion mechanism switches from magnetically controlled accretion from disks with inner holes to the as yet unknown mechanism. Vink *et al.* (2005a,b) demonstrated that the spectropolarimetric signatures observed across the Hα line in both T Tauri and HAe stars can be explained with accretion hot spots due to magnetically channelled accreting material. However, Hα does not necessarily probe the inner accretion regions in the very inner parts of the circumstellar disk. This is especially case for the hotter objects which have a much larger ionizing flux and consequently, the Hα forming region occupies a very large volume. Hence, we need another line that effectively traces the inner accretion regions. The helium line at 1.083μm is a very powerful accretion diagnostic. Its transition requires a

high excitation energy, and as such it probes the hot inner wind and accretion region much closer to the star than Hα. The line was recently recognised as an accretion tracer in the low mass T Tauri stars (Edwards *et al.* 2006; Fischer *et al.* 2008). Oudmaijer *et al.* (2011) in an exploratory study of a large sample of HAeBe stars, reported for the first time that the line is present in the spectra of HAeBe stars. Fig. 4.1 shows the helium line at 1.083μm and hydrogen recombination line Paγ of the spectrum of PDS 133 (spectral type B6). In the figure, the helium line shows both absorption and emission, while the Paγ line only shows emission. The helium emission line originates from the inner regions, which are not visible in the optically thick hydrogen line, because it arises from a much larger volume, masking the spectrum from the inner parts. By performing spectropolarimetry around this line we can hope to identify the geometry of the helium emitting material and distinguish between a disk accretion and an accretion funnel scenario for the massive objects. Studying both Hα and He I lines will thus allow us to see the similarities and the differences in the inner and the very inner parts of the disk.

Over Hα, the main line that has been studied in this manner, the line shows straight depolarisation signatures for the hotter HBe stars and intrinsic line polarization for the cooler HAe and T Tauri stars (Vink *et al.* 2005a). It is expected that for cool stars, the helium line displays a similar behaviour as the hydrogen lines as they both arise in accretion shocks. For the hotter stars, the hydrogen lines originate from a disk, further out from the star. If the helium shows a straight depolarisation for these more massive stars, then it arises from a disk, just like hydrogen, but much closer in, and disk accretion is the most likely mode of formation. If however, helium polarisation appears to exhibit intrinsic polariza-

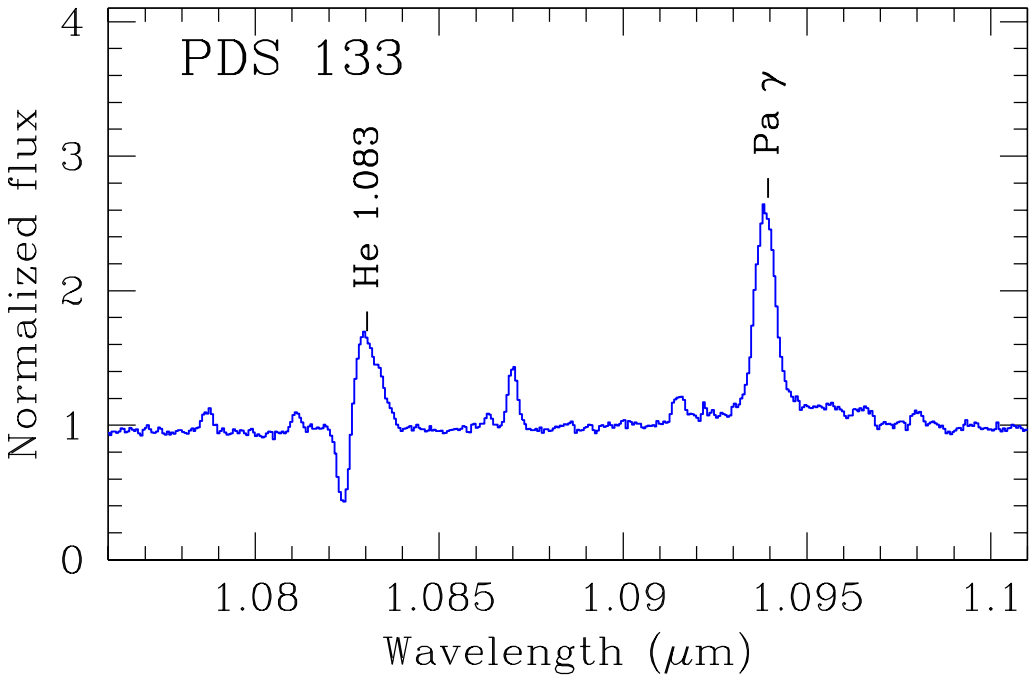

Figure 4.1: The helium line and Paγ line in the spectrum of PDS 133. The lines have different profiles, which is due to the fact that the hydrogen line originates and traces in a larger volume than the helium line. The figure is taken from Oudmaijer *et al.* (2011).

tion, accretion shocks and hot spots are then most likely the origin of the helium emission, indicating a different formation scenario. In this chapter I attempt to carry out the first spectropolarimetry across He I line at 1.083μm.

4.2 Observations and data reduction

The original plan was to observe a sample of HAeBe stars quasi-simultaneously with both the NICS instrument on the TNG, to perform spectropolarimetry on the helium line at 1.083μm, and the ISIS spectrograph on the WHT, La Palma, to perform spectropolarimetry on Hα. The reason for using the TNG is that linear

Table 4.1: HAeBe Observations (ISIS/WHT). The V magnitude and spectral type are taken from The *et al.* (1994); Cauley & Johns-Krull (2015); Fairlamb *et al.* (2015) and SIMBAD, and are listed in column 2 & 3. The integration times (column 5) denote the total exposures. The continuum polarisation was measure in the range between 6900 and 7100 Å and are listed in column 6 & 7. All the errors are differential, where the systematic error is ~ 0.16 per cent in polarization and $\sim 0.5^{\circ}$ in angle (see the text in Section 4.2.1 for details)

Name	V	Spec. type	Date	Exposure (s)	$P_{cont}(\%)$	θ°_{cont}
HD 163296	6.9	A1	04-08-15	12×20	0.160 ± 0.005	52.90 ± 0.94
MWC 610	8.9	B3	04-08-15	4×240	2.507 ± 0.006	81.95 ± 0.07
MWC 342	10.6	B(e)	04-08-15	24×20	0.736 ± 0.015	97.83 ± 0.56
HD 200775	7.4	B2	04-08-15	24×15	0.782 ± 0.005	93.36 ± 0.18
HD 203024	8.8	A	04-08-15	4×240	0.496 ± 0.007	49.77 ± 0.42
V361 Cep	10.2	B4	04-08-15	8×300	0.846 ± 0.007	89.36 ± 0.25
HD 240010	9.2	B1	04-08-15	4×240	3.018 ± 0.008	72.63 ± 0.07
V374 Cep	10.6	B0	04-08-15	8×300	4.841 ± 0.007	127.80 ± 0.04
MWC 863	8.8	A0	05-08-15	12×150	5.319 ± 0.004	56.95 ± 0.20
V718 Sco	8.9	A4	05-08-15	12×120	0.457 ± 0.007	78.77 ± 0.44
HD 141569	7.1	A0	05-08-15	8×90	0.639 ± 0.004	86.69 ± 0.18
MWC 300	11.6	B(e)	05-08-15	20×90	4.467 ± 0.015	58.62 ± 0.10
MWC 953	10.8	B2	05-08-15	12×180	2.555 ± 0.008	75.80 ± 0.10
MWC 623	10.9	K2/B4(e)	05-08-15	24×45	2.548 ± 0.010	54.02 ± 0.12
V1977 Cyg	10.9	B8	05-08-15	12×300,4×45	2.774 ± 0.008	168.91 ± 0.08
MWC 1080	11.6	B0	05-08-15	20×300	1.601 ± 0.007	81.36 ± 0.12
HD 144432	8.2	A7/F0	05-08-15	12×150	0.432 ± 0.004	12.80 ± 0.25

spectropolarimetry around He I line at 1.083 μm can not be obtained with the WHT and ESO at sufficient spectral resolution. The observations were carried out on the night of 2015 July 11 for the NICS and during the nights of 2015 August 4 and 5 for the ISIS. The reason was to have quasi-simultaneous observations to avoid misinterpretation of the data, the objects do not vary strongly over the weeks period between the two observations. Seventeen targets were selected from the HAeBe catalogue of The *et al.* (1994) and candidates of Vieira *et al.* (2003). The list of the objects is presented in Table 4.1, alongside their spectral type and V magnitudes from The *et al.* (1994); Cauley & Johns-Krull (2015); Fairlamb *et al.* (2015) and SIMBAD.

4.2.1 ISIS Observations

The linear spectropolarimetric data were obtained with the ISIS spectrograph on the WHT, La Palma, during the nights of 2015 August 4 and 5. The dates the data were taken and the exposure times per object are given in Table 4.1. The 1200R grating centred at 6800 Å, with a spectral range of 1000 Å, was employed with a windowed 351 × 4200 pixel CCD and a slit width of 1.0 arcsec. This setup provides a spectral resolution of ∼35 kms^{-1} as measured from arc lines around Hα line. The seeing was less than 1.0 arcsec throughout both nights. The polarisation optics, which consist of a rotating half-wave plate and a calcite block, was used in order to perform linear polarisation observations. The calcite block separates the light into two perpendicularly polarised light beams, the ordinary (O) and extraordinary (E) beam. One complete set of observations consists of four exposures with the half-wave plate set at angles: 10°, 55°, 32.5°, and 77.5°. The dekker with 18 arcsec slot separation was used to observe the object and the sky simultaneously. Several cycles of observations per object were obtained at the four position angles to check for the consistency of the results. Several short exposure times were taken for objects with strong Hα line to avoid the saturation. Polarised standard stars and zero-polarised standard stars were observed on each night to calibrate for the instrumental polarisation and angle offset.

The data reduction was carried out using IRAF (Tody 1993), which includes bias subtraction, flat fielding, sky subtraction and extraction of the O and E spectra. The extracted spectra were imported into the TSP package (Bailey 1997) maintained by Starlink to compute the Stokes parameters. The wavelength calibration was performed using FIGARO. For the analysis purposes, the data were

imported into the POLMAP package (Harries 1996) maintained by Starlink. Multiple observations of the same targets provided a very consistent results. As the observations were obtained at the parallactic angle to achieve high SNR, the angle calibration was performed using the observed polarised standard stars. The instrumental polarisation is found to be ∼0.1% while the angle offset is found to be less than 0.5° from the observation of unpolarised and polarised standard stars. As the instrumental and interstellar polarisation add a wavelength independent vector to the observed spectra, I did not correct the observed polarisation for them.

4.2.2 NICS Observations

The linear spectropolarimetric data were obtained with the NICS instrument on the TNG, La Palma on the night of 2015 July 11. The original plan was to use the medium resolution (R ∼ 2500) 1MIC grism combined with the 0.5 arcsec slit results in the highest resolution available and just enough to sample the line profiles (see later). The setup covers a spectral range from 0.96 to 1.09 μm. This enables us to observe the He I line at 1.083 μm. An added bonus is that for the brightest targets, the Paγ hydrogen recombination line at 1.094 μm ,which is at the edge of the filter, can be observed at good SNR and would even facilitate a direct comparison between He and H. The medium spectral resolution at 2500, which is the highest possible with NICS, is sufficient for our purposes as it will resolve the line profiles.

The proposal for these observations, using spectropolarimetry with the 1MIC grism, was submitted to the OPTICON panel. After technical and scientific

assessment, the time was awarded. However, on the day of the observations after taking flat fields and calibration lamp spectra with 1MIC grism, the support astronomer found out the that requested spectropolarimetry setup had never been possible at the TNG at all. It turns out that the polarising optics and 1MIC grism are in the same filter wheel, making it impossible to carry out observations in this set up. Instead, the observations in spectropolarimetry mode were carried out with low resolution (R $\sim$ 1000) IJ grism despite the fact that the chances to observe a line effect would be very low at this resolution. The grism covers a spectral range from 0.9 to 1.45 μm. To see the line profiles in the medium resolution and compare it with the low resolution, additional data in spectroscopic mode were obtained with 1MIC grism. In addition, due to a faulty motor, the targets were acquired manually resulting in significantly more overhead. In the end, it was only possible to observe three targets out of seventeen and at low resolution. The seeing was in the range between 1 to 4 arcsec, where the early objects have the worst seeing which progressively improved towards the end of the night. On average the seeing was worse and more unstable on the standard stars. Below I will describe the observations and data reduction. An assessment of the quality of the data is also provided, as the instrument had never been used in spectropolarimetric mode.

The NICS is able to simultaneously measure the polarised light at angles 90°, 0°, 45°, and 135° in a single exposure. Thus the NICS is very efficient as Q and U Stokes parameters can be derived in a single exposure, which eliminates any uncertainties due to time variability. Two polarised standard stars and a zero-polarised standard star were observed to calibrate for the instrumental polarisation and angle offset. The polarised standard stars were observed at many

position angles of the derotater to accurately measure the instrumental polarisation. The data reduction for both spectroscopic and spectropolarimetric data was carried out using IRAF following the standard procedures, which includes bias subtraction, sky subtraction, extraction of spectra and wavelength calibration. The spectral resolution was measured from arc lines around He I line at 1.083 μm and it was confirmed to be 1000 and 2500 for the IJ and 1MIC grisms respectively. I found a wavelength displacement among the spectra at angles 90°, 0°, 45°, and 135°. This is because the data at those angles are curved on the CCD. I shifted the spectra with reference to one of the spectra after identifying the features and computing the shift. All the polarised standard stars were observed twice at many position angles of the derotater. The Stokes parameters were then computed by using IRAF according to the following equations.

$$\begin{aligned} Q &= \frac{I(0^\circ) - I(90^\circ)}{I(0^\circ) + I(90^\circ)} \\ U &= \frac{I(45^\circ) - I(135^\circ)}{I(45^\circ) + I(135^\circ)} \end{aligned} \tag{4.1}$$

The observations consisted of several short exposures at two different nod positions (hereafter Nod A and Nod B) along the slit to perform sky subtraction. On average the position of Nod B is 20 arcsec from Nod A (see Fig. 4.2). The order of the individual beams on the CCD are as follows: 90°, 0°, 45°, and 135°. According to equation 4.1, the beams at 90° and 0° give the Stokes Q parameter while the Stokes U parameter is determined from the beams at 45° and 135°. The observations for the targets were as follows: 10, 20 and 6 sets of data were taken for HD 163296, HD 200775 and MWC 1080 respectively.

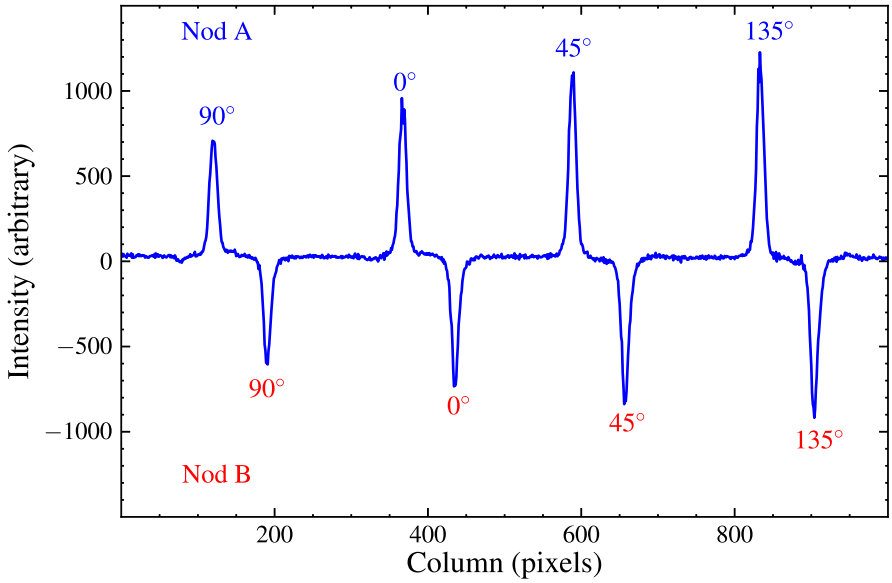

Figure 4.2: The NICS polarisation raw data, one column, at four angles in two nod positions (Nod A and Nod B) of HD 163296. In the figure the Nod A is subtracted from the Nod B to perform sky subtraction.

4.3 Results on He I 1.083 μm

The full spectra at both resolutions are shown in Figs. 4.3 and 4.4. The medium resolution spectra show Paδ in emission in all the targets and weak Paγ at the edge of the spectra in HD 200775 and MWC 1080. A P Cygni profile He I line at 1.083 μm is present in the spectra of HD 163296 and MWC 1080 while a very weak absorption is visible in the spectra of HD 200775. In the medium resolution spectra, the counts at the edge of the spectra around He I at 1.083 μm are very low ($\sim$ 1000). The low resolution spectra show Paβ, Paγ and Paδ line in emission in all objects. In addition, a P Cygni He I line at 1.083 μm is also seen in the low resolution spectra of HD 163296 and MWC 1080. Paδ, Paγ and He I line at 1.083 μm lines for both resolutions are overplotted in Fig. 4.5. The Paγ line is

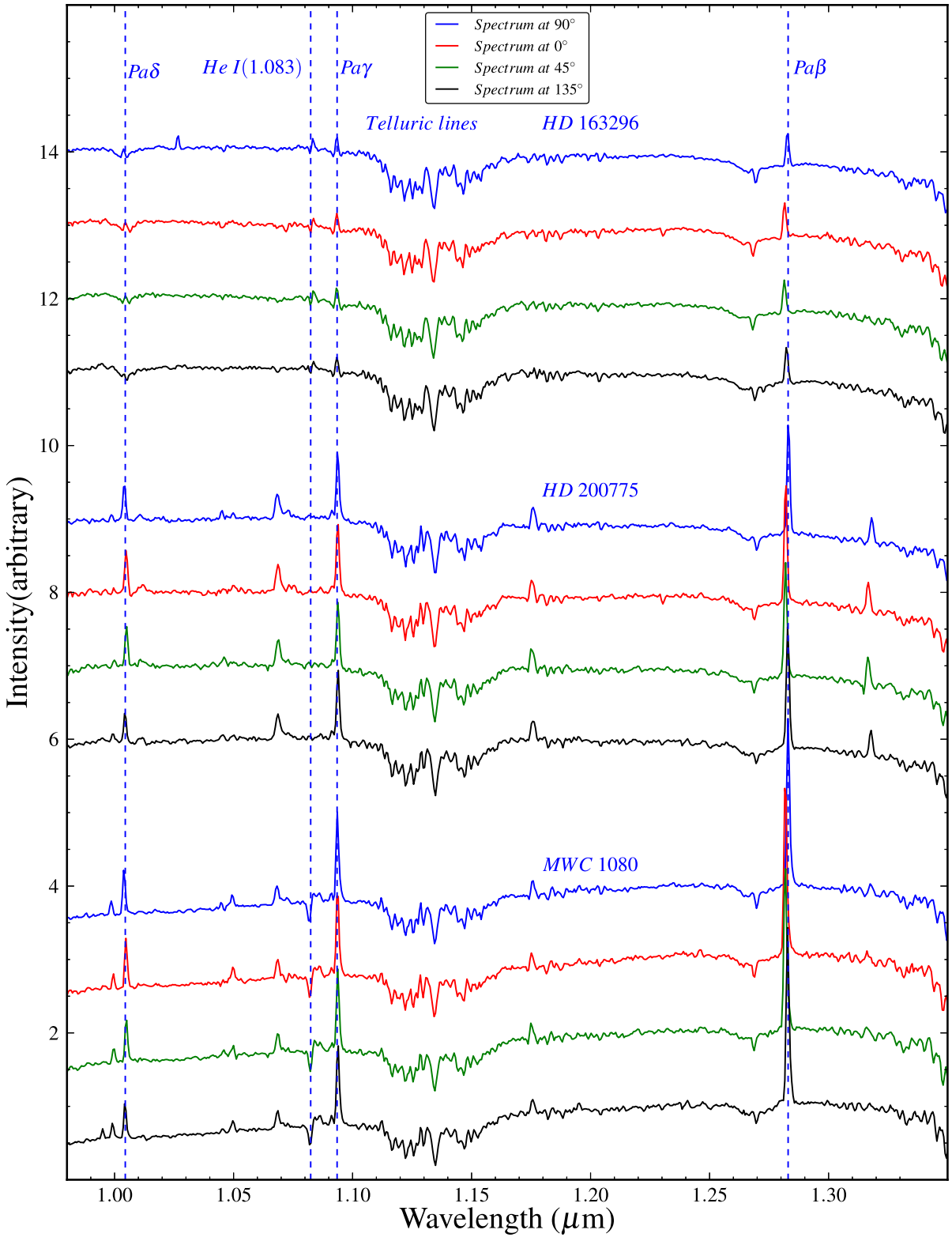

Figure 4.3: NICS spectropolarimetric observations at low resolution. The polarisation spectra at angles 0°, 45°, 90°, and 135° of HD 163296, HD 200775 and MWC 1080. The observed spectral lines are highlighted by blue dashed lines. Fe II lines at 0.999 and 1.050 μm, and [O I] at 1.317 μm are also identified.

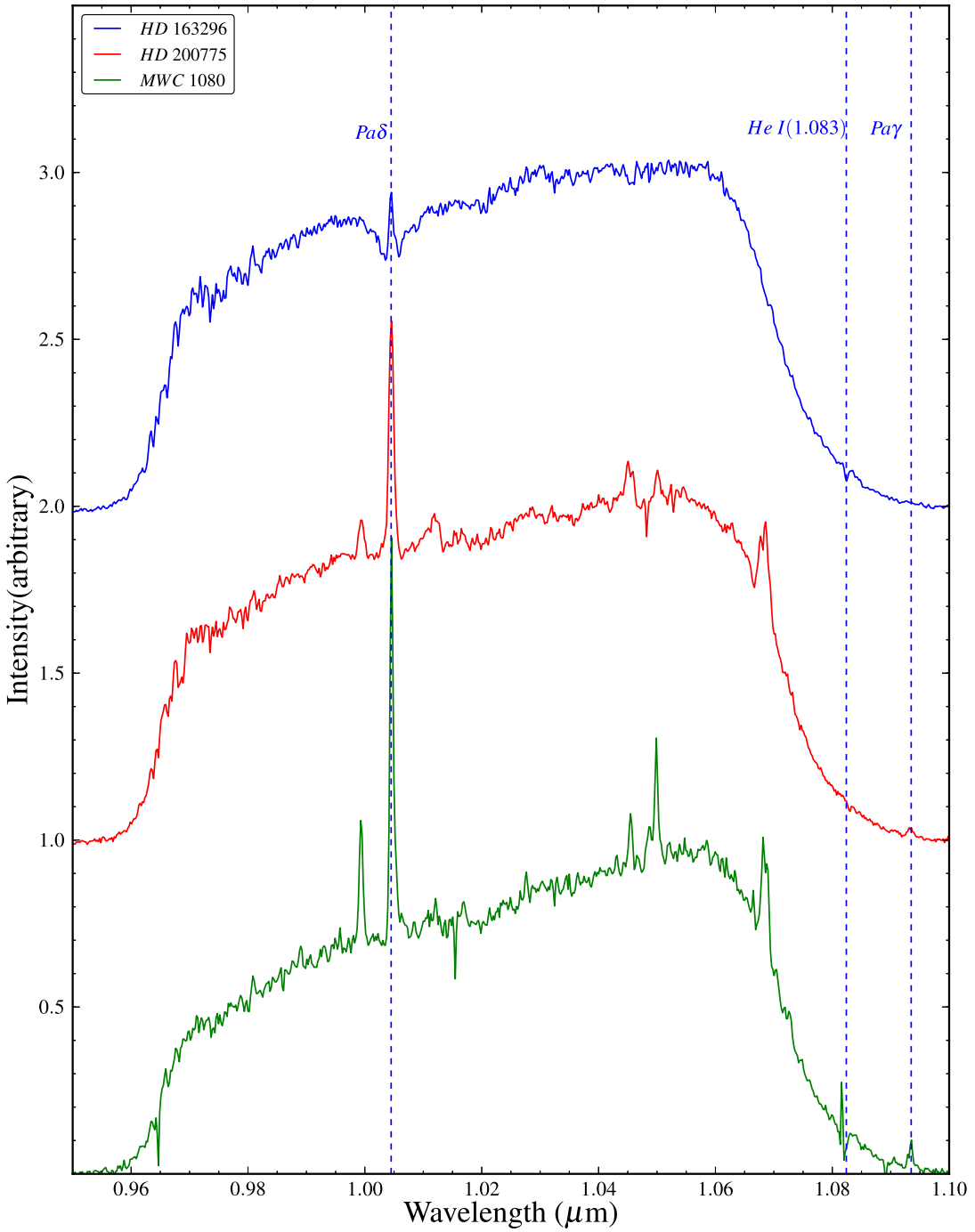

Figure 4.4: NICS spectroscopic observations at medium resolution. The spectra of HD 163296, HD 200775 and MWC 1080. The observed spectral lines are highlighted by blue dashed lines. Fe II lines at 0.999 and 1.050 μm are also identified.

not observed in the medium resolution for HD 163296 due to low counts at the edge of the spectrum. I present the continuum and line polarisation around He I at 1.083 μm.

4.3.1 Continuum Polarisation

The continuum polarisation in the Q and U Stokes parameters was measured in the the range between 1.0μm and 1.05μm for the two polarised standard stars and the zero polarised standard star, the results are summarised in Table 4.2. For the zero polarised standard star HD 188512, the Q and U values are measured twice in 10 derotater position angles. The polarisation values are different over different position angles of the derotater which may perhaps be expected. However, different sets of observations at the same angle should provide similar polarisation values, which is not the case in our observations. As seen in Fig. 4.6 and Table 4.2 there is a big difference between the first and second sets at the same position angle in zero polarised standard star HD 188512, for example Q and U vary by 10% and 5% respectively at the angle of 60°. The assessment of the raw data, count rates, by eye is consistent with these results. The polarised standard stars HD 187929 and HD 183143 were also observed several times at the angle of 0°. The measured Q and U values for these two standard stars vary significantly among the observed sets (see Table 4.2). However, the Q and U polarisation are more stable in our science objects, the average Q and U of several sets of observations are summarised in Table 4.3.

The *(Q, U)* diagram of the NICS observations and the ISIS observations in R band are plotted in Fig. 4.7. The Q and U were measured around 0.7 μm

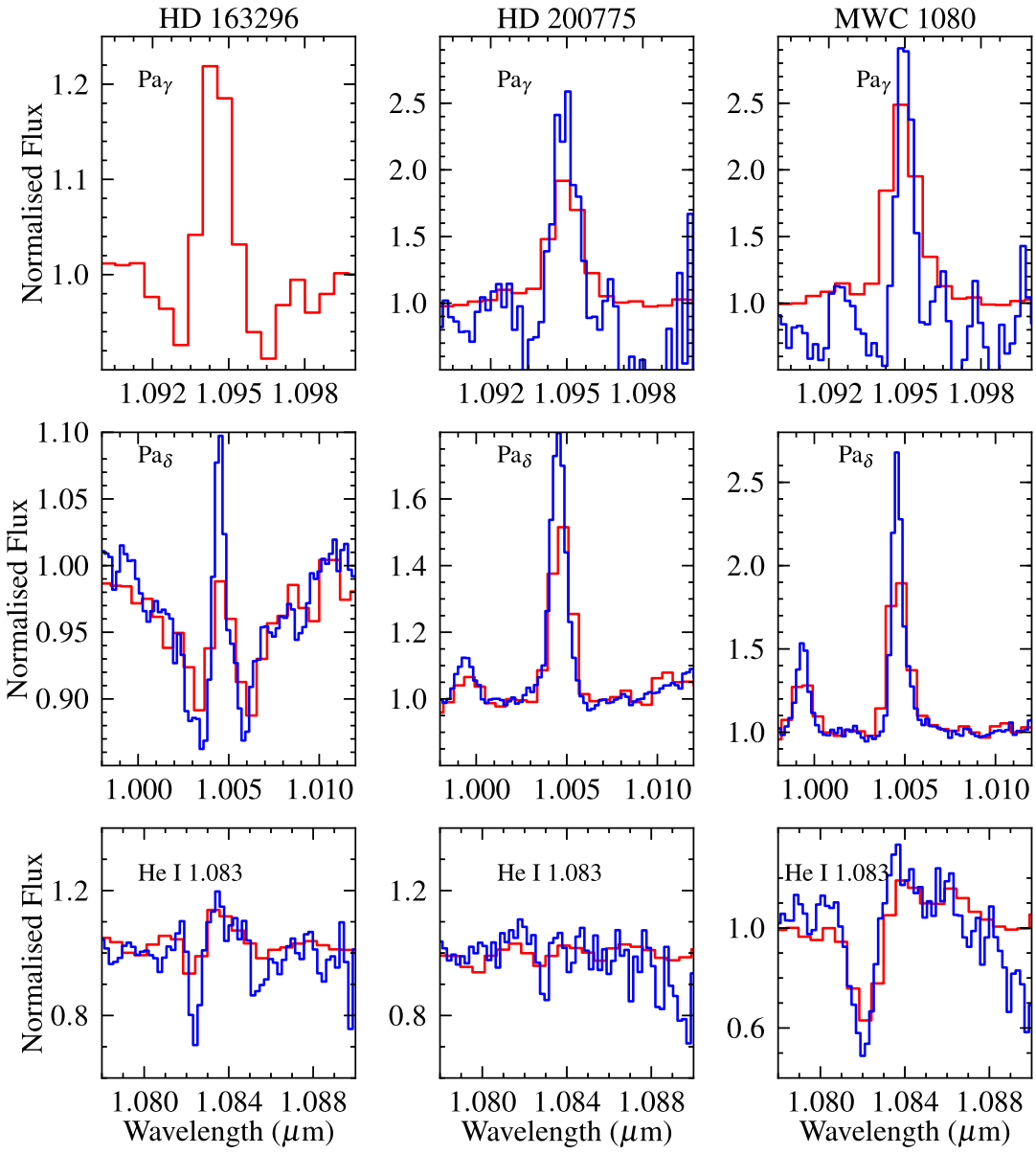

Figure 4.5: A selection of normalised observed spectral lines from the NICS low and medium resolutions for HD 163296, HD 200775 and MWC 1080. The red line denotes the low resolution spectropolarimetric data while the blue solid line is the the medium resolution spectroscopic data. The Paγ line is not observed in the medium resolution for HD 163296 due to low photon counts at the edge of the spectrum. The EW of the lines are similar in both resolutions.

Table 4.2: The log of the polarised and zero polarised standard stars (NICS/TNG), the data were observed on the night of 2015 July 11. HD 188512 is a zero polarised standard star while HD 187929 and HD 183143 are polarised standard stars. The continuum polarisation in Q and U Stokes parameters was measured in the range between 1.μm and 1.05μm and is listed in column 4 & 5. The errors in the Stokes Q and U are differential and are typically: 1 per cent in HD 188512 and HD 187929; 2 per cent in HD 183143. The accepted polarisation values for the polarised standard stars in Q and U was measured in J band from the degree of polarisation and polarisation angle provided by Bailey & Hough (1982).

Object	J	Exposure (s)	Derotator PA (°)	Observed Q(%)	Observed U(%)	Literature Q(%)	Literature U(%)
HD 188512	2.2	5	0	3.4	1.4		
		5	0	11.8	-1.3		
		5	30	4.6	-2.8		
		5	30	6.5	0.7		
		5	60	15.6	-4.7		
		5	60	5.7	1.8		
		5	90	4.6	1.8		
		5	90	11.6	-4.7		
		5	120	6.1	2.5		
		5	120	-50.0	28		
		5	150	7.1	3.2		
		5	150	-49.0	4.7		
		5	180	2.5	5.2		
		5	180	6.8	-3.3		
		5	210	3.8	2.3		
		5	210	-0.7	9.8		
		5	240	7.8	-1.1		
		5	240	5.2	-1.2		
		5	270	9.1	-1.8		
		5	270	6.8	3.2		
HD 187929	2.4	5	0	5.4	5.7	-0.80 ± 0.04	0.08 ± 0.04
		5	0	7.8	-2.9		
		5	0	7.1	3.3		
		5	0	4.8	6.6		
HD 183143	4.1	3	0	13.5	-7.4	2.71 ± 0.03	-0.38 ± 0.03
		3	0	15.4	-1.1		
		4	0	13	7.8		
		4	0	9.1	0.85		
		4	0	8.7	0.5		
		4	0	5.3	0.4		

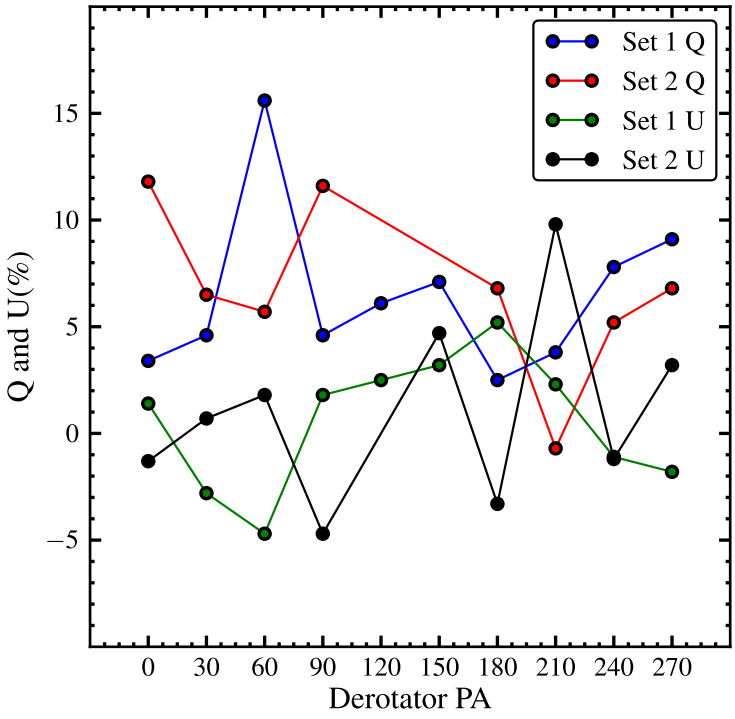

Figure 4.6: Zero polarised standard star HD 188512: The Q and U values are plotted against the derotater position angle. At each PA the Q and U are measured twice, note that Q and U vary by up to 10%. Two Q values in the second set at the angle of 120° and 150°; and a U value at the angle of 120° in the second set are not plotted because they lie out (see Table 4.2). The error in Q and U is ± 1.0 %.

Table 4.3: HAeBe Observations (NICS/TNG). The Vmagnitude and spectral type are taken from The *et al.* (1994); Fairlamb *et al.* (2015) and SIMBAD, and are listed in column 4 & 5. The integration times (column 7) denote the total exposures. The continuum polarisation in Q and U Stokes parameters was measured in the range between 1.μm and 1.05μm and are listed in column 8 & 9. The errors in the Stokes Q and U are differential.

Name	Mode	SNR	V	Spec. type	Date	Exposure (s)	Q(%)	U(%)
HD 163296	Polar.	200	6.9	A1	11-07-15	10×120	7.9 ± 0.4	2.2 ± 0.5
HD 163296	Spect.	80			11-07-15	2×120		
HD 200775	Polar.	250	7.4	B2	11-07-15	20×120	6.9 ± 0.5	1.4 ± 0.7
HD 200775	Spect.	70			11-07-15	2×120		
MWC 1080	Polar.	100	11.6	B0	12-07-15	6×300	6.4 ± 1.0	0.2 ± 0.6
MWC 1080	Spect.	50			11-07-15	1×150		

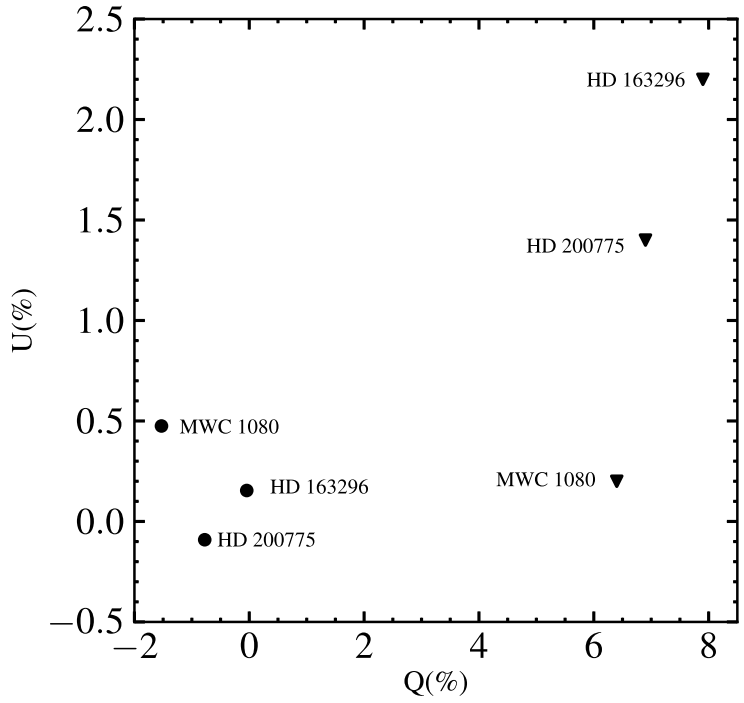

Figure 4.7: (*Q, U)* diagram. The solid triangles represent the Q and U value of NICS low resolution observations, the values were measured in the range between 1.0 μm and 1.05μm. The solid circles represent the Q and U value of ISIS observations, the values were measured in the range between 6900 and 7100 Å. The typical error in Q and U is ±0.005% in ISIS observations and ±0.5% in NICS observations.

and 1.0μm for the ISIS and NICS observations respectively, the values are not expected to vary significantly between 0.7 μm and 1.0μm (cf. Serkowski law of polarisation). The instrumental polarisation in the ISIS observations is as low as ∼0.1%, which can be neglected. The figure shows that the two observations have two different patterns. The difference in Q between the two observations for all the targets is constant at ∼8.0% while the difference in U is in the range between∼0.25% and ∼2.0%. It would be tempting to assume that the instrumental polarisation at Q is 8.0% but that would imply that the instrumental polarisation at U would vary by 2.0% among the observations. However, even if

this was the case, the offsets between the observed polarisation of our standard stars and the literature are not constant in Q and U. This could be a rough value of the instrumental polarisation, it is not possible to accurately measure it with such an unstable system.

In summary, the observed Q and U polarisation values for the standard stars are inconsistent. However, the values are less variable for the science objects. This might be due to the fact that the exposure time is longer on the science objects and the seeing is relatively better.

4.3.2 Line Spectropolarimetry

Despite the inconsistency in the observed continuum polarisation linear spectropolarimetry can still be attempted as that concerns a differential effect which is independent of the continuum values. The low resolution data around He I at 1.083 μm for HD 163296, MWC 1080 and HD 200775 are shown as a triplot in the upper half of Fig. 4.8. In this triplot, the Stokes I (normal intensity) is shown in the lower panel, the Stokes U in the middle, while the Stokes Q is shown in the upper panel. The results are also represented in a Stokes *(Q, U)* diagram (bottom) in Fig. 4.8 using the same wavelength range of the triplot spectra. The He I at 1.083 μm has a P Cygni profile in HD 163296 and MWC 1080, in MWC 1080 the line has a strong absorption and is accompanied by a very weak redshifted emission. The line is not observed in HD 200775. As is shown in Fig. 4.8 there is no clear change in the polarisation spectra and the *(Q, U)* diagram across the He I at 1.083 μm in these objects.

It can be argued that, detecting a line effect across 1.083 μm at this low

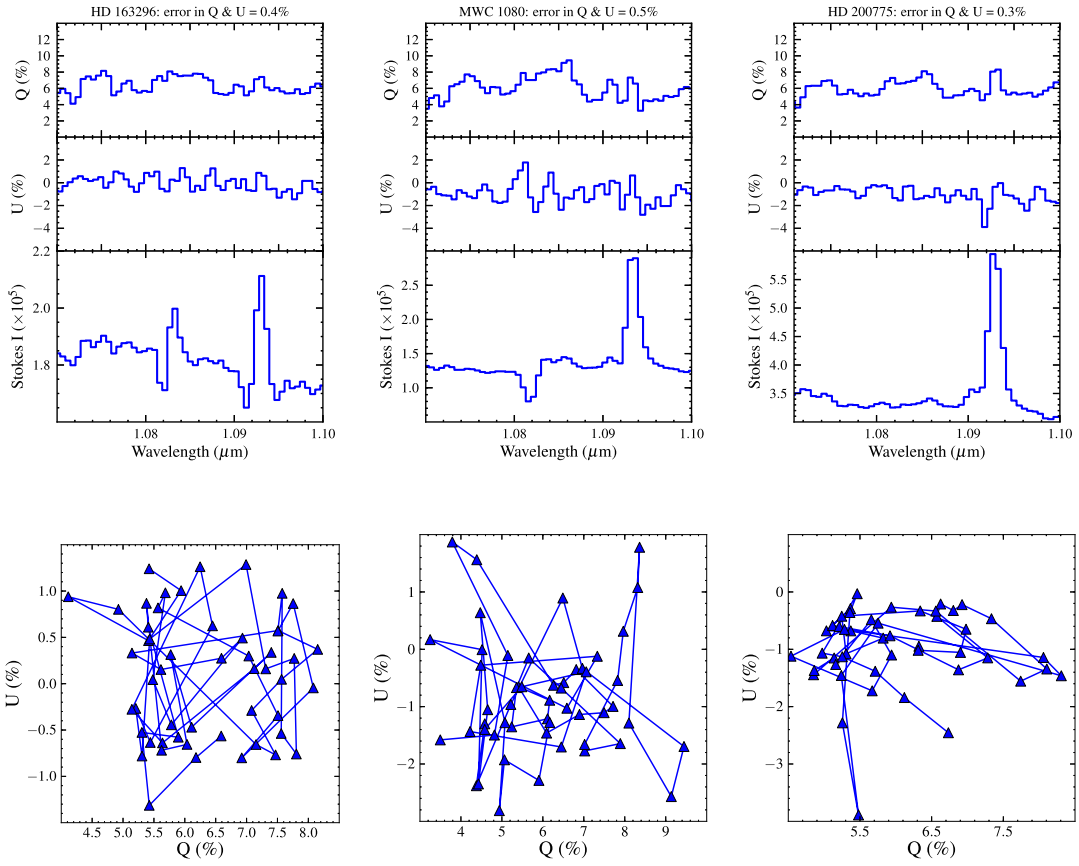

Figure 4.8: He I at 1.083 μm spectropolarimetry of the NICS sample. The data are presented as a combination of triplots (top) and (Q,U) diagrams (bottom). In the triplot polarisation spectra the Stokes intensity (I) is shown in the lowest panel, U (%) in the centre, while the Q (%) is shown in the upper panel. The Q and U Stokes parameters are plotted against each other below each triplot.

resolution and low SNR is unlikely. To check this, I reduced the spectral resolution of our FORS2 spectropolarimetric data from $\sim$ 4500 to $\sim$ 1000 in R band which is comparable to NICS's spectral resolution (see Fig. 4.9). The figure shows that the magnitude of the line effect, across Hα and [O I] at 6300 Å as an example, decreases by $\sim$ 50-60%. The magnitude of a typical line effect is around 0.5% and hence it is very difficult to be detected in the low resolution of IJ grism.

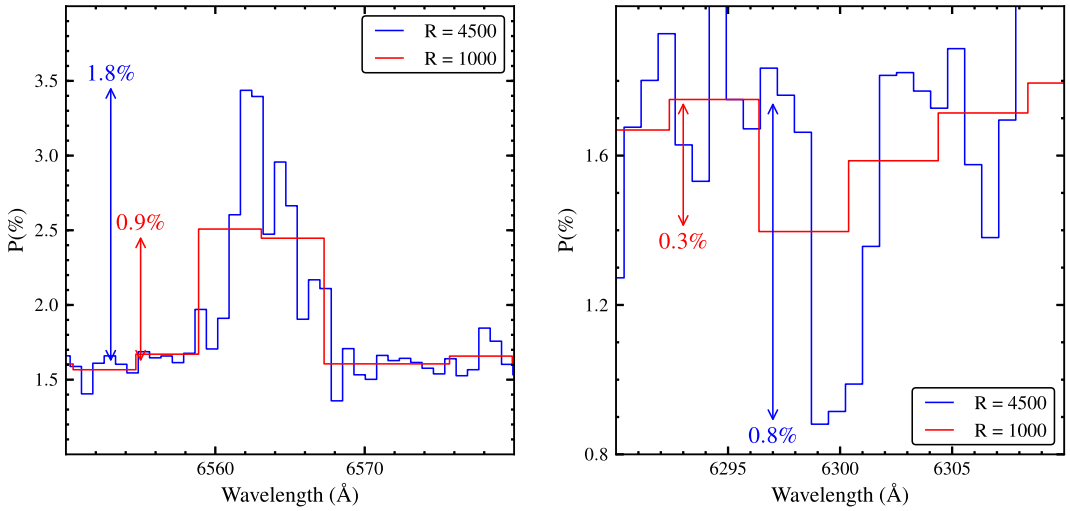

Figure 4.9: Polarisation Line effect in low and medium resolutions across: Hα line of GU CMa (left) and [O I] at 6300 Å of CPD-485215 (right). The blue solid line is the medium resolution (R = 4500) while the low resolution is plotted in red solid line. The line effect decreases by more than 50% in the low resolution, it is hardly visible across [O I] at 6300 Å at this low resolution.

It turns out that I was the first to use the NICS in spectropolarimetry mode. In summary, none of the objects show any signs of line effect across the He I at 1.083 μm or any other emission lines. It is hard however to draw any firm scientific conclusions from this finding. I will now continue with the optical data only.

4.4 Results on Hα

The results of the ISIS optical data around Hα are presented. I begin with a brief presentation of the continuum polarisation of the ISIS targets before focusing on Hα line polarimetry. In addition, a statistical study on Hα line polarimetry will be provided of all HAeBe stars that have observed thus far.

Table 4.4: Previous measured continuum polarisation. Column 2 gives the band at which the polarisation was measured. Columns 3 and 4 list the measured polarisation percentage and polarisation angle. The references are presented in the last column.

Object	Band	$P_{cont}(\%)$	θ°_{cont}	Ref.
HD 163296	R	0.70 ± 0.01	1.60 ± 0.20	1
	V	0.247 ± 0.026	29.3 ± 3.0	2
	R	0.322 ± 0.021	35.7 ± 1.9	2
	I	0.330 ± 0.027	37.0 ± 2.3	2
	V	0.417 ± 0.035	36.0 ± 2.5	3
MWC 342	U	1.24 ± 0.12	97.4 ± 2.9	4
	B	1.03 ± 0.11	99.6 ± 3.1	4
	V	1.02 ± 0.08	103.8 ± 2.1	4
	R	1.15 ± 0.08	101.5 ± 2.0	4
	I	0.67 ± 0.05	105.6 ± 2.3	4
HD 200775	V	1.0 ± 0.1	88.0 ± 3.0	5
	B	0.88 ± 0.01	96.4 ± 0.1	6
	R	0.82 ± 0.01	95.6 ± 0.1	6
	R	0.801 ± 0.003	93.6 ± 0.1	7
HD 141569	R	0.647 ± 0.005	85.2 ± 0.2	7
MWC 300	U	3.32 ± 0.27	58.8 ± 2.3	4
	B	4.22 ± 0.21	58.0 ± 1.4	4
	V	4.83 ± 0.11	59.3 ± 0.7	4
	R	4.81 ± 0.18	60.3 ± 1.1	4
	I	3.92 ± 0.14	58.8 ± 1.0	4
MWC 623	U	2.57 ± 0.14	53.0 ± 1.6	4
	B	2.89 ± 0.12	55.2 ± 1.2	4
	V	2.67 ± 0.08	54.4 ± 0.8	4
	R	2.77 ± 0.10	54.4 ± 1.0	4
	I	1.25 ± 0.08	52.7 ± 1.2	4
MWC 1080	B	1.71 ± 0.02	72.2 ± 0.3	6
	V	2.54 ± 0.30	68.2 ± 3.4	8
	R	1.73 ± 0.1	77.0 ± 1.0	9
HD 144432	V	0.25 ± 0.02		10

References. 1: Ababakr *et al.* (2016); 2:Yudin & Evans (1998); 3: Rodrigues *et al.* (2009); 4:Zickgraf & Schulte-Ladbeck (1989); 5:Hillenbrand *et al.* (1992); 6: Mottram *et al.* (2007); 7: Vink *et al.* (2005a); 8:Vrba *et al.* (1979); 9: Vink *et al.* (2002) ;10: Oudmaijer *et al.* (2001)

4.4.1 Continuum Polarisation

The continuum polarisation is measured in R band in the wavelength range from 6900 to 7100 Å and the results are summarised in Table 4.1. The degree of linear continuum polarisation ranges from ∼0.2 % in the very low polarised star HD 163296 to ∼5 % in the highly polarised star MWC 863. The literature polarisation values for the objects are summarised in Table. 4.4. The observed polarisation values are broadly consistent with the previous measurements.

4.4.2 Line Spectropolarimetry

Hα spectropolarimetry is performed for all the targets and the results are shown in Fig. 4.10, 11 objects out of 17 have never been observed with spectropolarimetry. This is an excellent opportunity to finish our Hα spectropolarimetry survey of HAeBe objects that had not been studied thus far (Oudmaijer & Drew 1999; Vink *et al.* 2002, 2005a; Mottram *et al.* 2007; Wheelwright *et al.* 2011b). In total, 11 objects show a possible line effect across Hα line. In this thesis, a sample of 28 HAeBe objects has been studied by combining these observations with the FORS2 data (Ababakr *et al.* 2016 and presented in Chapter 2). In this sample, 18 objects are HBe stars and the remaining 10 objects are HAe stars. R Mon is discarded from the sample, leaving us with a sample of 27 objects. (see the discussion in Chapter 2). 13 HBe objects out of 17 (∼76 %) show a possible line effect while 8 HAe objects out of 10 (∼80 %) show a possible line effect (see table 4.5). For HBe objects, the line effect is consistent with depolarisation for 7 objects and the remaining 6 objects display the McLean line effect. In contrast, 2 HAe stars show an intrinsic line polarisation, a McLean effect in one object and a depolarisation

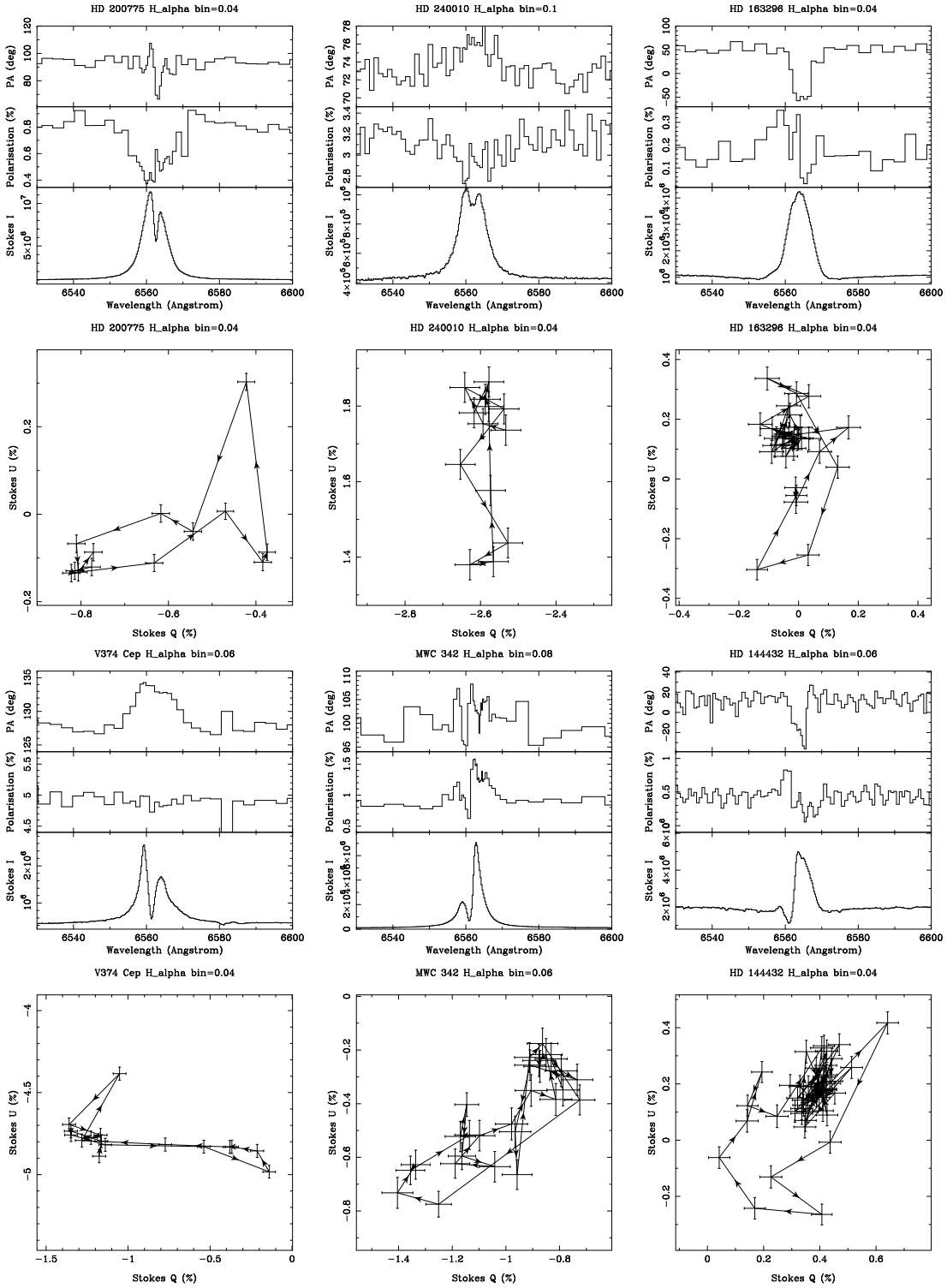

Figure 4.10: Hα spectropolarimetry of the ISIS sample. The data are presented as a combination of triplots (top) and (Q,U) diagrams (bottom). In the triplot polarisation spectra the Stokes intensity (I) is shown in the lowest panel, polarisation (%) in the centre, while the position angle (PA) is shown in the upper panel. The Q and U Stokes parameters are plotted against each other below each triplot. The data are rebinned to a constant value, as indicated at the top of each plot.

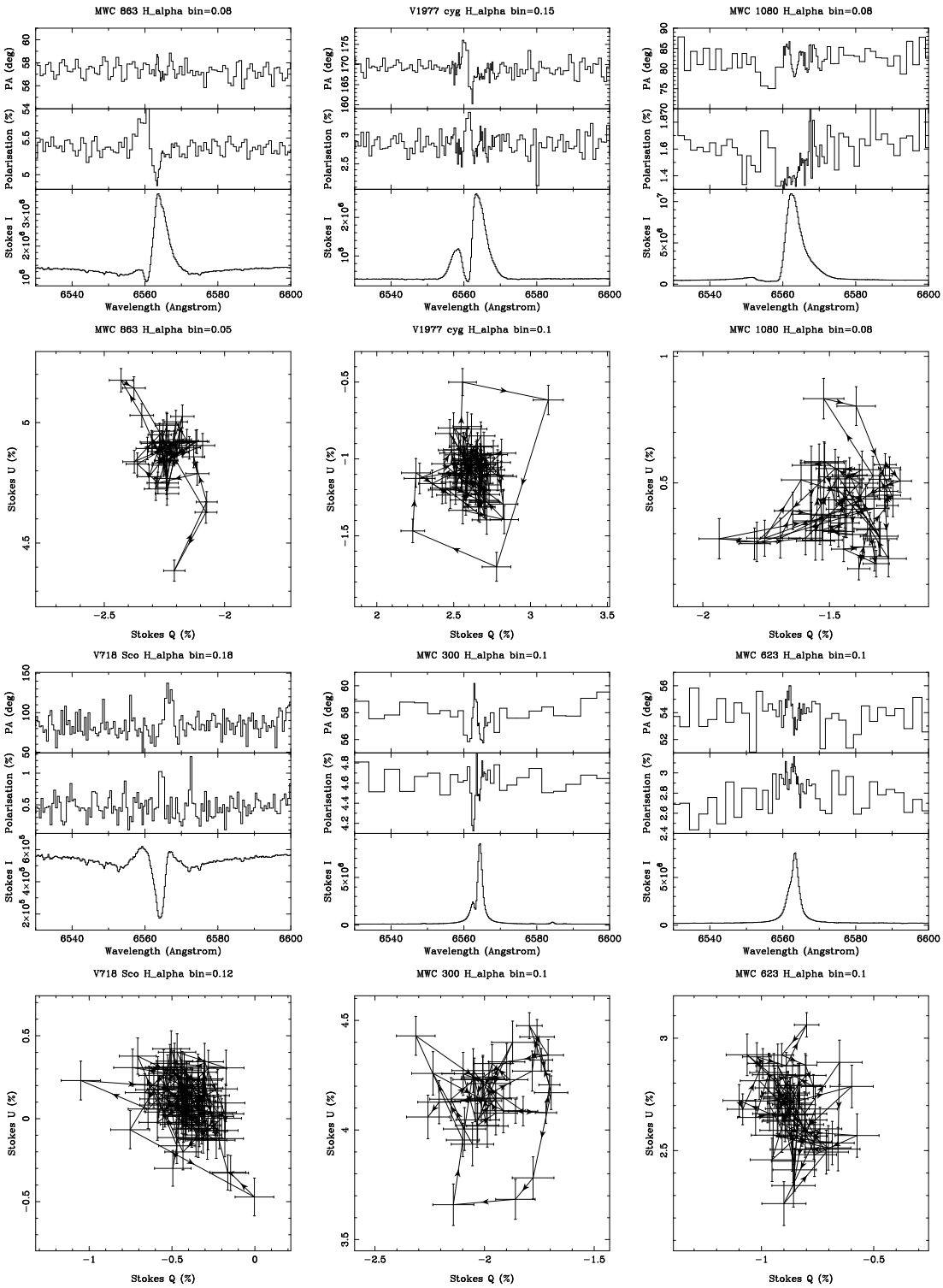

Figure 4.10: continued

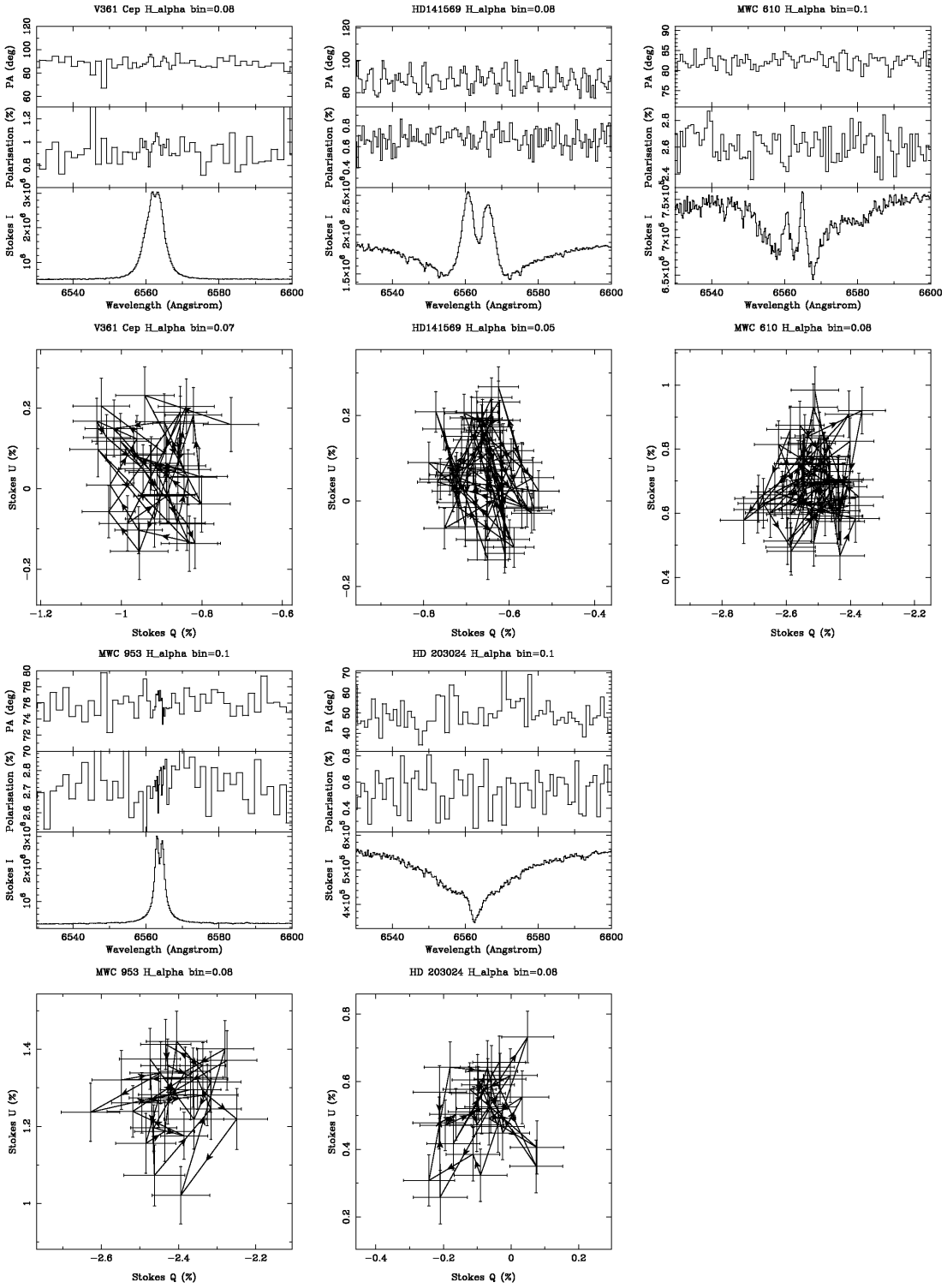

Figure 4.10: continued

in 2 objects. The line effect in 2 HAe objects is not strong enough,$\leq 3.0\sigma$, to categorise. MWC 863, HD 144432 and HD 98922 show two different line effect. It seems that HBe stars are mostly consistent with a depolarisation while HAe stars display intrinsic line polarisation. It is not clear exactly at what spectral type the line effect changes from line polarisation to depolarisation line effect. In order to do this a bigger sample is needed. The line effect signature ranges from depolarisation to intrinsic line polarisation through the McLean effect (see table 4.5).

4.4.3 Statistical Analysis on Hα

In order to perform a statistical study on the line polarimetry, a big sample of HAeBe stars is needed. The size of our sample (ISIS and FORS2) is increased by adding all the previous spectropolarimetric work across Hα line of HAeBe stars (Oudmaijer & Drew 1999; Vink *et al.* 2002, 2005a; Mottram *et al.* 2007; Wheelwright *et al.* 2011b). The final sample size is 56 HAeBe objects (31 HBe and 25 HAe). The vast majority, 51, objects were selected from the HAeBe catalogues of The *et al.* (1994), 9 of which are in the table of extreme emission lines and other early emission line stars that are not in the main table of HAeBe stars. The remaining 5 objects were selected from the candidates of Vieira *et al.* (2003). Thus, about half of the HAeBe catalogue has been observed spectropolarimetrically, the remaining targets of the catalogue are too faint which require very long exposure times as the spectropolarimetry needs high SNR. The results for the whole sample are shown in Fig.4.11. The figure shows that 42 objects (75 %), 21 HBe and 21 HAe, show a line effect. To see at what spectral type the line

Table 4.5: The Hα line results of the FORS2 and ISIS observations: $\Delta\lambda(pol)$ is given in column 4 and it is the width of the line effect. Column 5 gives the fractional width $\Delta\lambda(pol)/\Delta\lambda(I)$. Column 8 provides an estimation of the intrinsic polarisation PA derived from line excursions in the *(Q, U)* diagram. The uncertainty in intrinsic polarisation PA is approximately 10°.

Object	Spec. type	Line effect (σ level)	$\Delta\lambda(pol)$	$\frac{\Delta\lambda(pol)}{\Delta\lambda(I)}$	Flip in Pol or PA	Class.	θ°_{intr}
HD 163296	A1	12.0σ	15.0±2.0	0.86±0.11	Y	P	122
MWC 610	B3	No					
MWC 342	B(e)	12.0σ	17.5±2.5	0.71±0.10	N	D	112
HD 200775	B2	23.5σ	29.0±6.0	1.10±0.22	N	D	95
HD 203024	A	No					
V361 Cep	B4	No					
HD 240010	B1	11.0σ	27.0±4.0	0.87±0.13	N	D	45
V374 Cep	B0	27.5σ	27.5±3.5	0.81±0.10	N	D	178
MWC 863	A0	16.0σ	15.0±2.0	1.00±0.13	N	M/P	62
V718 Sco	A4	5.5σ	12.0±2.0	0.72±0.12	N	M	160
HD 141569	A0	No					
MWC 300	B(e)	5.5σ	3.5±0.5	0.29±0.04	N	M	135
MWC 953	B2	No					
MWC 623	K2/B4(e)	No					
V1977 Cyg	B8	11.0σ	5.8±0.8	0.34±0.04	N	M	37
MWC 1080	B0	4.5σ	7.8±1.3	0.29±0.05	N	M	50
HD 144432	A7/F0	12.0σ	12.5±1.5	1.00±0.12	N	D/M	28
PDS 27	B3	4.5σ	18.0±2.0	0.57±0.06	N	M	77
PDS 37	B3	6.0σ	15.5±2.0	0.55±0.07	N	M	56
PDS 133	B6	3.5σ	6.0±1.0	0.28±0.04	N	M	126
HD 98922	A0	4.0σ	9.8±1.3	0.72±0.09	N	D/M	22
R Mon(2011)	B8	15.0σ	30.5±2.5	1.00±0.08			
R Mon(2012)		32.5σ	26.5±2.5	0.82±0.07			
GU CMa	B1	15.5σ	12.8±2.8	0.70±0.15	N	D	127
CPD-485215	B6	4.5σ	17.0±2.0	1.00±0.11	N	D	62
HD 163296	A1	6.5σ	19.5±2.5	1.05±0.13	Y	P	112
HD 85567(2011)	B7	6.0σ	17.0±2.0	0.87±0.10	N	D	31
HD 85567(2012)		2.5σ					
V380 Ori(2011)	A0	No					
V380 Ori(2012)		4.5σ	7.0±1.0	0.54±0.07	N	P	10
HD 104237	A7	2.0σ					
BF Ori	A2	3.0σ					

D: Depolarisation, P: Polarisation, M: McLean

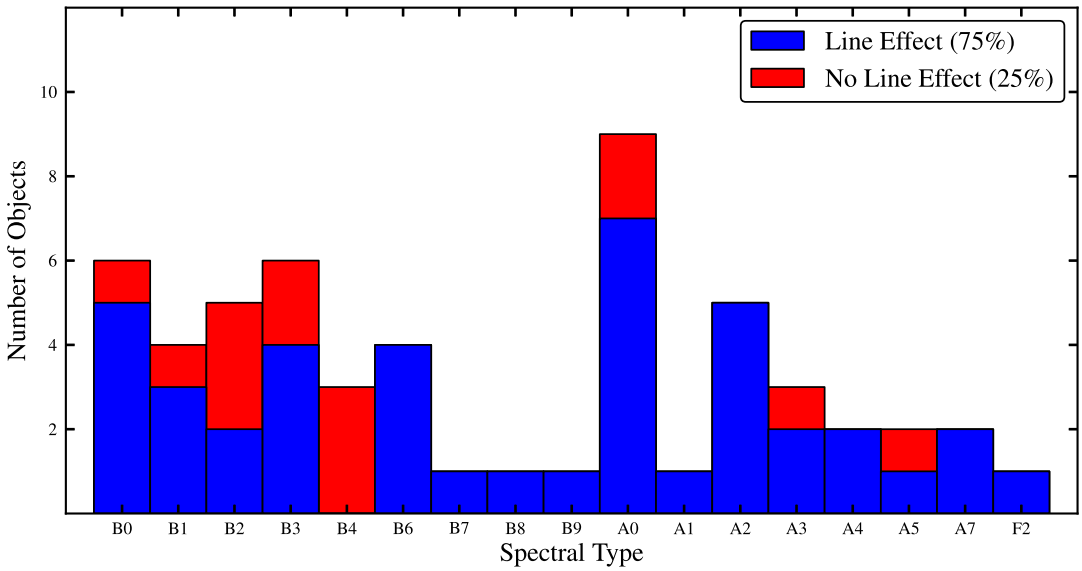

Figure 4.11: The figure shows the observed line effect across Hα line in each sub group of spectral type of the whole sample of HAeBe stars that have been observed spectropolarimetrically. The sample contains 56 objects and are collected from the current work and the previous spectropolarimetric work on HAeBe stars (Oudmaijer & Drew 1999; Vink *et al.* 2002, 2005a; Mottram *et al.* 2007; Wheelwright *et al.* 2011b).

effect switches from line polarisation to depolarisation, I increased the sample to include 9 T Tauri stars of Vink *et al.* (2005a) and the result is shown in Fig.4.12. The figure shows that the intrinsic line polarisation is dominated in T Tauri and late HAe stars while most early HBe stars show a depolarisation. There is also a number of HBe stars displaying a McLean line effect. It seems that the line effect changes from intrinsic line polarisation to depolarisation around A0-B9 spectral type.

The magnitude of the line effect is measured from the (*Q, U)* diagram for all the objects that show a clear line effect. It ranges from ∼0.3% to ∼2.0% and the average is ∼0.9 %. Only R Mon shows a magnitude of ∼7% which is not expected from electron scattering close to the star and due to a different mechanism (see

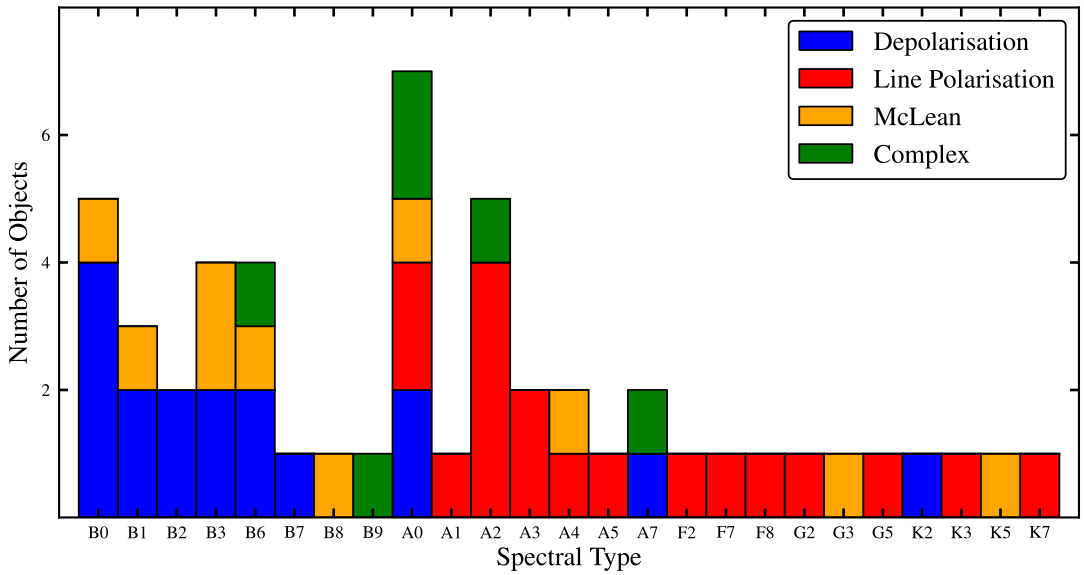

Figure 4.12: The figure represents the type of the observed line effect across Hα line as a function of spectral type of a sample of 51 HAeBe and T Tauri objects. The data are taken from the current work and the previous spectropolarimetric work on HAeBe and T Tauri stars (Oudmaijer & Drew 1999; Vink *et al.* 2002, 2005a; Mottram *et al.* 2007; Wheelwright *et al.* 2011b).

Chapter 2). To see whether there is any correlation between this magnitude and the spectral type, I plot them against each other and the result is shown in Fig. 4.13. The figure shows that there is no correlation (correlation coefficient (r) $\sim$ 0) between the magnitude of the line effect and the spectral type.

To see whether the strength of the emission lines is correlated with the magnitude of the line effect, I measured the line peak to continuum of the Hα line of all objects that display a line effect. Fig.4.14 shows the magnitude of the line effect as function of the emission line strength. As is shown in the figure there is a very weak correlation between them(r = 0.18) which means that only 3% of the variation in the magnitude can be explained by the line strength.

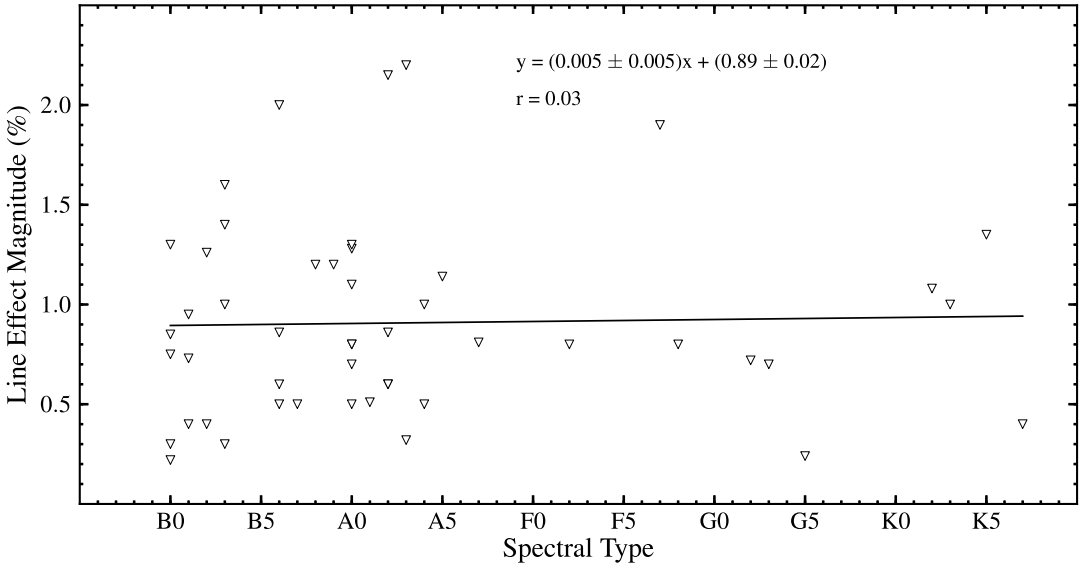

Figure 4.13: The figure shows the relation between the magnitude of the observed line effect in (%) of the sample of HAeBe stars and the spectral type. The data are taken from the current work and the previous spectropolarimetric work on HAeBe and T Tauri stars (Oudmaijer & Drew 1999; Vink *et al.* 2002, 2005a; Mottram *et al.* 2007; Wheelwright *et al.* 2011b).

4.4.4 Hα Line Effect Width

To differentiate between the depolarisation and the line polarisation effect, the width of the line effect is used (see Table 4.5). The method was first used by Vink *et al.* (2002, 2005a) to classify the line effects. Vink *et al.* (2002, 2005a) statistically classified stars according to the fractional width $[\Delta\lambda(pol)/\Delta\lambda(I)]$ at which the polarisation changes across the line. Generally a wide fractional width is associated with depolarisation line effect, whereas, the fractional width of line polarisation effect is often narrower than the depolarisation. Here, $\Delta\lambda(I)$, which is the Full Width at Zero Intensity (FWZI), is measured at 2% above the continuum level. This is because it is difficult to distinguish the line from the continuum, especially for broad line profiles. $\Delta\lambda(pol)$ is the width over which the

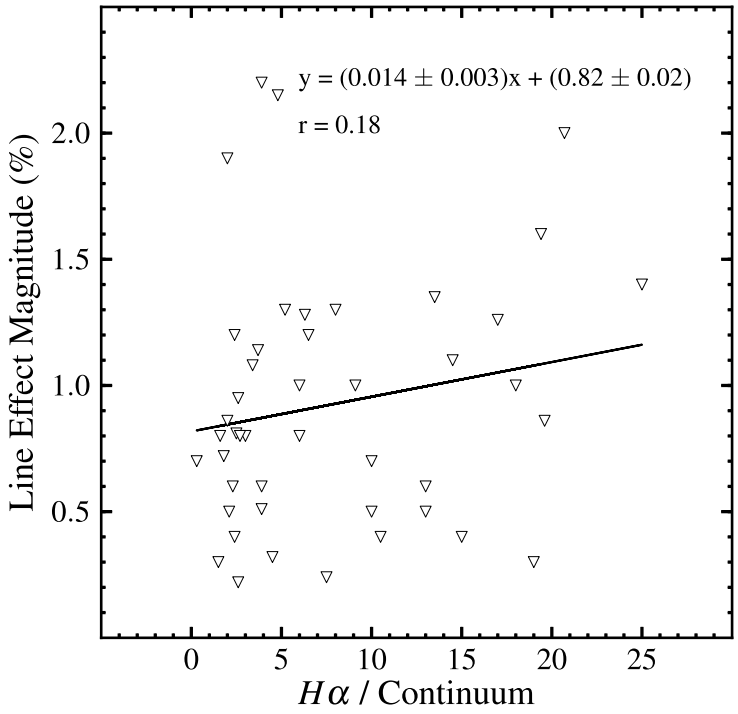

Figure 4.14: The figure shows the relation between the magnitude of the observed line effect in (%) of the sample of HAeBe stars and the strength of Hα line. The data are taken from the current work and the previous spectropolarimetric work on HAeBe and T Tauri stars (Oudmaijer & Drew 1999; Vink *et al.* 2002, 2005a; Mottram *et al.* 2007; Wheelwright *et al.* 2011b).

polarisation changes across the line in the polarisation spectra.

If the line effect is detected across the absorption component of the emission line then it is considered as a McLean line effect. The line effect across the emission line is classified based on two criteria which are fractional width and whether there is a flip in the polarisation and PA spectra or not. If the fractional width is equal to or larger than 0.7 and there is no flip in the polarisation and PA spectra across the emission line then the line effect is consistent with depolarisation. On the other hand, if the fractional width is equal to or larger than 0.7 and a flip is observed in either the polarisation or PA spectra then the line effect is considered

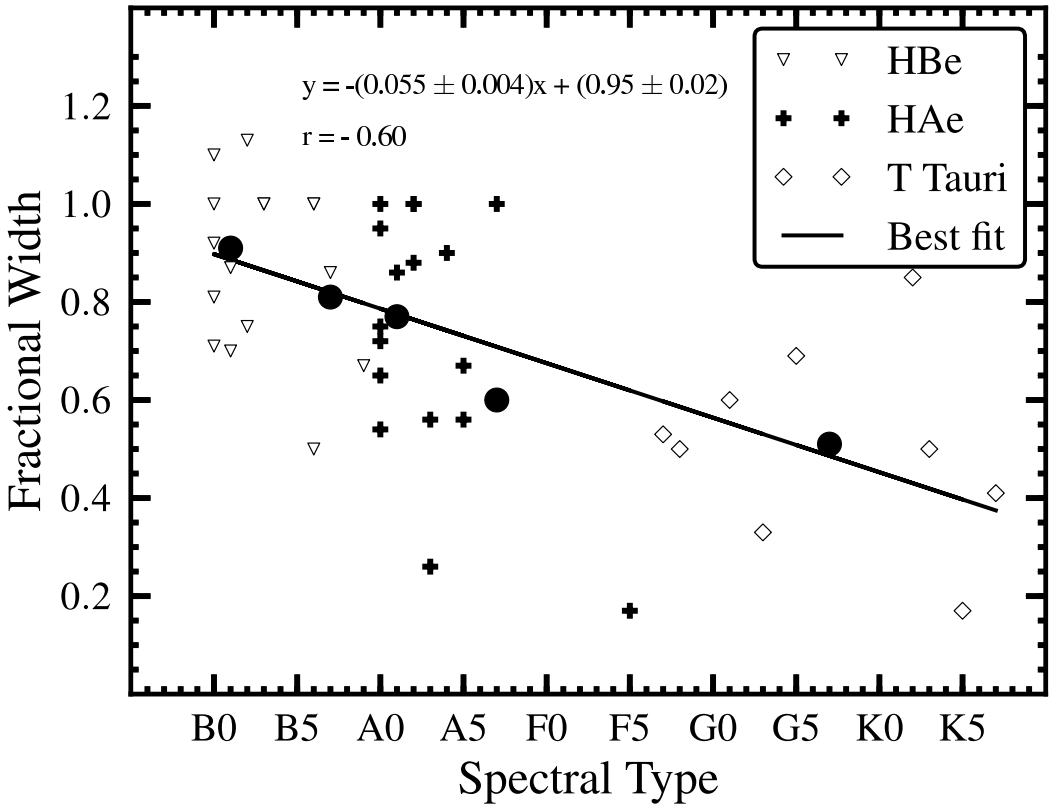

Figure 4.15: The fractional width of the line effect ($\Delta\lambda(pol)/\Delta\lambda(I)$) is plotted against spectral type of a sample of HAeBe and T Tauri stars. The black solid line represents the best fit of the data, the errors of the best fit are the standard deviation. The black solid circles with error bars represent the averages of early HBe, late HBe, early HAe, late HAe and T Tauri from early to late spectral type respectively.

as polarisation. In addition, if the fractional width is smaller than 0.7 then the line effect is also consistent with polarisation. In some cases two different line effects, a McLean line effect across the absorption and either depolarisation or intrinsic polarisation across the emission line, can be observed for the same object. The flowchart in Fig. 4.16 shows the decision tree used for the classification of different line effects.

Vink *et al.* (2002, 2005a) found a fractional width of 1.0±0.2, 0.7±0.3 and

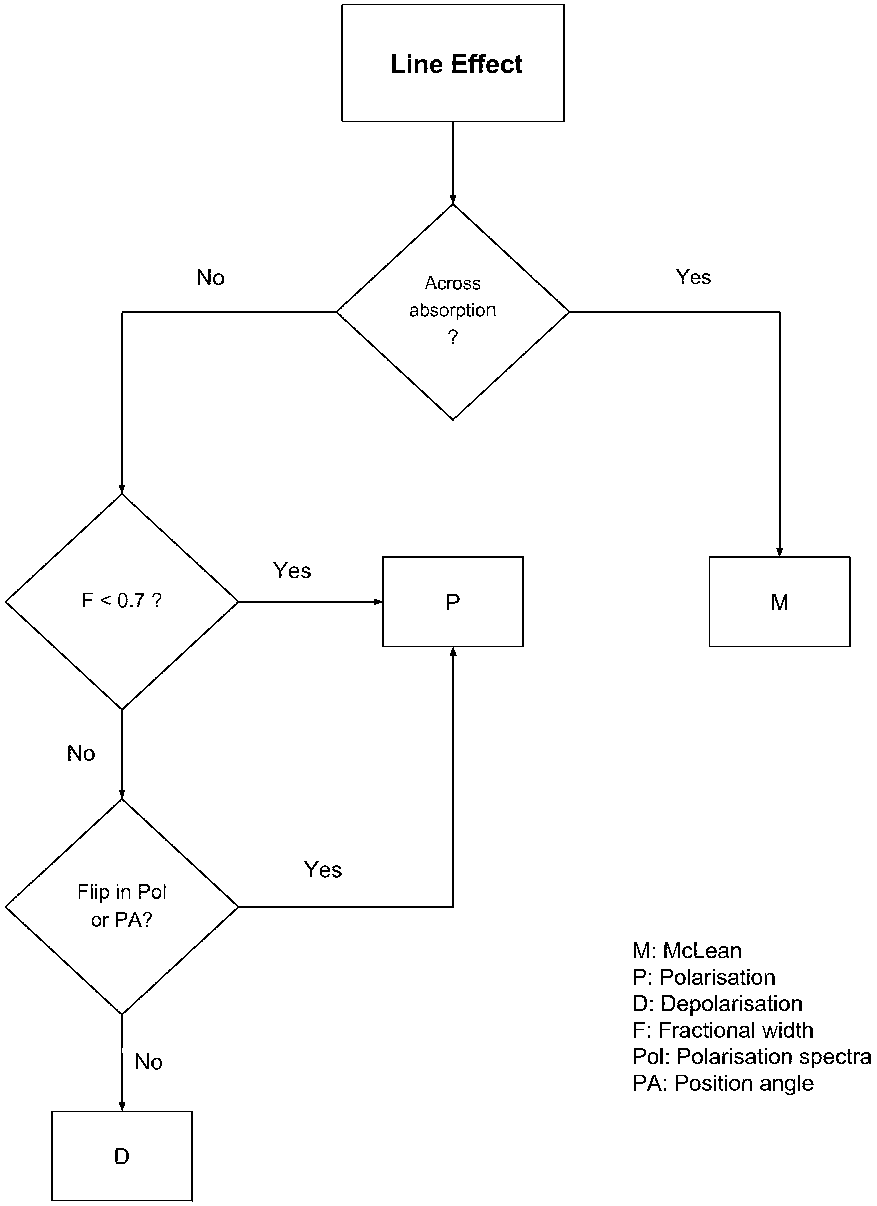

Figure 4.16: The flowchart shows the classification of the line effect.

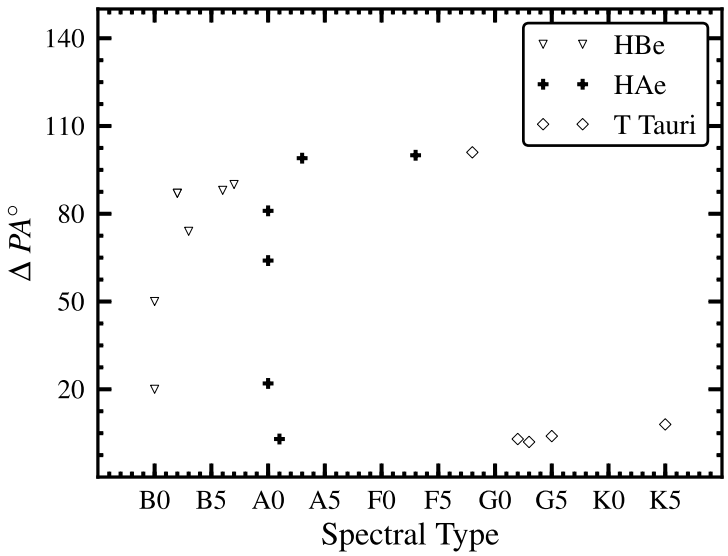

Figure 4.17: The difference between disk position angle and the polarisation angle is plotted against spectral type.

0.5±0.2 for early HBe stars, HAe stars and T Tauri stars respectively. It tends to decrease towards late spectral type, as expected from Fig. 4.12. I can now revise the relation by increasing the sample from 25 to 42 objects. The result is plotted in Fig. 4.15, the figure shows that there is a correlation, r = -0.60, between the fractional width and the spectral type. The updated values are found to be 0.88±0.17, 0.73±0.26 and 0.50±0.2 for HBe, HAe and T Tauri stars. Distinctively, the values of 0.91±0.15, 0.81±0.2, 0.77±0.22, 0.60±0.34 are found for early HBe, late HBe, early HAe and late HAe stars. This sub classification reveals that the fractional width of late HBe stars and early HAe stars are very close. This suggests that late HBe stars and early HAe stars share similar spectropolarimetric behaviour.

4.4.5 Polarisation and Disk PA

Spectropolarimetry also provides an unique opportunity to deduce the geometry of the circumstellar environments. It enables us to directly measure the intrinsic polarisation angle from the loop of the line effect across the lines in the *(Q, U)* diagram. The observed loops in the *(Q, U)* diagram (see Fig. 4.10) represent the change in polarisation across the line profiles and hence the asymmetry in the ionised region. I was able to measure the intrinsic polarisation angle for the objects whose Hα line show a polarisation line effect and the results are summarised the last column in Table 4.5. Once the intrinsic polarisation angle is known, the orientation of the disk can be estimated. If the circumstellar disk is optically thin, the intrinsic polarisation angle is perpendicular to the position angle of the disk. However, for an optically thick circumstellar disk, multiple scattering will take place, in this case the intrinsic polarisation would be parallel to the disk position angle (Vink *et al.* 2005a). I have compared our intrinsic polarisation angle (PA) with disk PAs and the result is summarised in Table 4.6 and Fig. 4.17. In the table the sample of Wheelwright *et al.* (2011b) has been increased by adding five more objects to draw better statistical results. The results reinforce the finding of (Wheelwright *et al.* 2011b) that the polarisation position angle is related to the disk position angle. Therefore, spectropolarimetry can be used to estimate the disk position angle even for unresolved objects.

4.5 Discussion

It is clearly seen in the Fig.4.12 that T Tauri stars and HAe stars, especially late HAe, stars share the same Hα intrinsic polarisation line effect. This effect arises

Table 4.6: Comparison between disk PA and intrinsic polarisation PA. The intrinsic polarisation PA data in column 2 are from the current work, disk PA in column 3 are taken from literature and the differences between them is listed in column 4.

Object	S.Type	Pol. PA°	Disk PA°	Δ PA°	Rela.
HAe					
AB Aur	A0	160[1]	79[2]	81	$\perp$
MWC 480	A3	55[1]	154[3]	99	$\perp$
HD 179218	A0	45[4]	23[5]	22	$\parallel$
CQ Tau	F3	20[1]	120[6]	100	$\perp$
HD 163296	A1	122[7]	128[8],126[2],120[6]	3	$\parallel$
MWC 863	A0	62[7]	358[17]	64	$\perp$
HBe					
HD 200775	B2	95[7],93[9]	7[10]	87	$\perp$
MWC 147	B6	168[9]	80[11]	88	$\perp$
HD 45677	B2	164[12]	77[13]	87	$\perp$
V1685 Cyg	B3	36[9]	110[3]	74	$\perp$
MWC 1080	B0	75[9]	55[3]	20	$\parallel$
HD 85567	B7	31[14]	121[15]	90	$\perp$
MWC 137	B0	25[1]	75[16]	50	$\perp$
T Tauri					
RY Tau	F8	62[18]	163[1]	101	$\perp$
SU Aur	G2	127[19]	130[1]	3	$\parallel$
FU Ori	G3	47[20]	45[1]	2	$\parallel$
GW Ori	G5	56[21]	(60)[1]	4	$\parallel$
DR Tau	K5	128[22]	120[1]	8	$\parallel$

References. 1: Vink *et al.* (2005a); 2: Mannings & Sargent (1997); 3: Eisner *et al.* (2004); 4: Wheelwright *et al.* (2011b); 5: Fedele *et al.* (2008); 6: Doucet *et al.* (2006); 7: This work; 8: Isella *et al.* (2007); 9: Mottram *et al.* (2007); 10: Okamoto *et al.* (2009); 11: Kraus *et al.* (2008); 12: Patel *et al.* (2006); 13: Monnier *et al.* (2006); 14: Ababakr *et al.* (2016); 15: Vural *et al.* (2014); 16: Fuente *et al.* (2003); 17: Fukagawa *et al.* (2003); 18: Akeson *et al.* (2003); 19: Akeson *et al.* (2002); 20: Malbet *et al.* (2005); 21: Mathieu *et al.* (1995); 22: Kitamura *et al.* (2002)

from scattering photons originating from a compact source, where the accretion take place on to the star, off the circumstellar disk. In contrast, HBe stars, in particular the early HBe stars, show a depolarisation line effect, explained by the presence of an extended circumstellar disk. Thus, the presence of the intrinsic line effect could be related to the magnetospheric accretion model which has been proposed for the accretion of low mass stars.

The complication is whether HAe stars have sufficient magnetic fields to facilitate MA or not. Wade *et al.* (2005, 2007); Alecian *et al.* (2013); Hubrig *et al.* (2009, 2013) detected magnetic fields ($\sim$ a few hundred G) in a few HAeBe stars, mostly HAe and late HBe stars. Grady *et al.* (2010) in a study of a HAe object MWC 480, conclude that the star goes through the same MA accretion as T Tauri stars. Vink *et al.* (2002) found an intrinsic line polarisation across Hα line of MWC 480. Fairlamb *et al.* (2015), in a study of a large sample of HAeBe stars, found that the detection of large UV excess can not be modelled with MA in seven HBe stars. These could suggest that T Tauri and HAe stars accrete via MA. In contrast, the spectropolarimetric results and the lack of magnetic field detection of early HBe stars could imply that MA is no longer valid at these spectral ranges. One of the possible models is the Boundary Layer (BL) where the circumstellar disk extended to the surface of the central star. Blondel & Djie (2006) found that HAeBe stars can be accreting via BL, through modelling the UV spectra of a sample of HAeBe stars.

4.6 Conclusions

This chapter presents the spectropolarimetric results for seventeen HAeBe stars, eleven of them had never been observed spectropolarimetrically. In addition, I draw useful statistical conclusions from a large sample of almost 60 HAeBe stars from this work and the previous linear spectropolarimetric work on HAeBe stars. The main findings in this work are as follows:

- He I at 1.083 μm is a very powerful line to trace the very inner region of circumstellar disk. However, the line did not show any sign of a legitimate

and physical line effect at this low resolution and SNR.

- Eleven objects out of seventeen in the ISIS observations show a clear detection of a line effect across Hα line. This indicates the presence of a flattened structure, such as a disk around them.

- The detection rate of the line effect is 75 % (42/56) in the sample of 56 objects that have been observed spectropolarimetrically.

- Most of the HBe stars' signatures are consistent with a depolarisation line effect. In contrast, intrinsic line polarisation is more common in HAe and T Tauri stars. It seems late HBe and early HAe stars are at the interface between the two line effects. The similarity between T Tauri and HAe stars might mean that both are forming via magneto-spheric accretion. The interface between HBe and HAe is possibly where the accretion mechanism switches from magnetospheric accretion to another, unknown, process.

- The magnitude of the line effect is of order of 0.3-2 %. There is no correlation between this magnitude and spectral type. A very weak correlation is seen between the magnitude of the line effect and the strength of Hα line.

- The intrinsic polarisation angle is related to the disk position angle. Therefore, the orientation of disk can be established even if it is not resolved

Chapter 5

Conclusions

5.1 Summary

The work presented in this thesis has focused on the circumstellar disks around pre-main sequence HAeBe stars using various observational techniques including spectropolarimetry, spectroscopy and interferometry.

The main findings in the thesis are summarised briefly below:

- **Chapter 2** presented linear spectropolarimetric observations of a sample of 12 HAeBe stars. The medium resolution spectra cover the entire optical range and comprise the largest spectropolarimetric wavelength coverage, 4560 Å to 9480 Å, published to date. A change in linear polarisation across the Hα line, either from the emission or absorption component is detected in all objects. This indicates that the circumstellar geometry of the material at size scales of order stellar radii around HAeBe objects is not circular on the sky but it has a flattened structure, such as a disk. Most HBe stars display a depolarisation or McLean line effect, while intrinsic line polarisation is

more common in HAe stars. The large wavelength coverage results show that Hα is the spectral line in the optical wavelength range that is most sensitive to revealing deviations from spherical symmetry. In addition, Hα is the only line that shows an effect across the absorptive component of the line, the line effect is stronger for a weaker absorption. A scenario was presented to explain this finding and demonstrate that the detection of the line effect strongly relies on the number of scattered photons into our line of sight. Apart from Hα, few other spectral lines, including forbidden lines, display a change in polarisation across the line. The line effect is consistent with a broad depolarisation in all the forbidden lines. This implies further support for a disk structure around these stars. R Mon is a special case in the sample, it is the only object in the sample in which many lines have a polarisation effect. This effect is much stronger than in all other objects. The direction of polarisation is different for various over emission lines. This suggests that the observed polarisation in R Mon is caused by different emitting volumes within the circumstellar environment. Finally, the first spectropolarimetry of HAeBe stars is presented across the calcium triplet and it is found that all the three lines behave similarly. Therefore, the possibility of resonant line scattering being responsible for the line effects can be ruled out, as this predicts different polarisation signatures across the three triplet lines.

- **Chapter 3** presented the results of spectroscopic, spectropolarimetric and interferometric observations of two previously poorly studied HAeBe candidate stars. The spectra of both objects are remarkably similar, strongly

suggesting that both are in the same evolutionary phase. The spectra are dominated by strong emission lines, and do not reveal any photospheric absorption lines. Indeed, the only lines that are fully in absorption are the interstellar DIB lines. The observed spectral lines indicate that both objects undergo strong winds as supported by the clear, and numerous, P Cygni profiles observed and line variations. The P Cygni absorption extends in both stars to hundreds of kms^{-1}. Through analysis of spectral lines and photometry, an effective temperature of the order of 20000 K is found for both objects. The results also show that the objects are massive $\sim$ 20 $M_{\odot}$ and have large radii $\sim$20 $R_{\odot}$. This suggests that these two objects are very early in their evolution and may become O-type stars. The results of spectropolarimetric and near infrared interferometric observations strongly support the presence of a circumstellar disk around these two objects. The observed variability in V_{LSR} and the results of interferometric data, suggest that both objects might have a companion, in particular PDS 27 could be a triple system.

- **Chapter 4** presented the first spectropolarimetry of HAeBe stars across He I line at 1.083 μm, obtained with the NICS instrument on the TNG. The line is very powerful in tracing the inner accretion regions of the circumstellar disk. However, it was not possible to obtain the data at the required medium spectral resolution. Instead, the data could only be obtained at low spectral resolution, R = 1000, and only for three objects. Although the lines did not show any sign of a line effect at this low resolution and low SNR, the FORS2 data suggest that a polarisation effect which is typically

of order 0.5% would be hard to detect at this low resolution. Therefore, the absence of line effect is not compelling and it requires a higher spectral resolution to confirm whether there is a line effect or not. Hα spectropolarimetric data are also presented for a sample of 17 HAeBe objects, to complete the spectropolarimetric survey of HAeBe stars. This chapter also provides a large statistical investigation of the spectropolarimetric properties of HAeBe stars. The sample size of the ISIS and FORS2 observations was increased by adding all the previous spectropolarimetric work across Hα line of HAeBe stars. The final sample size is 56 HAeBe objects, half of the HAeBe catalogue, where 31 are HBe objects and 25 are HAe objects. The spectropolarimetric results of the sample show that the detection rate of the line effect is very high (75 %). This implies that most HAeBe stars have a circumstellar disk around them. The statistics also show that the intrinsic polarisation line effect in T Tauri and HAe stars switches to a depolarisation line effect in HBe stars around the spectral type of early A and late B. This might suggest that at these spectral types, the accretion mechanism changes from MA to an as yet unknown mechanism. The magnitude of the line effect, which is found to be 0.3-2 %, is not correlated with the spectral type and the strength of Hα line.

5.2 Future Work

The results of this thesis has improved our understanding of properties in the circumstellar environments of HAeBe stars. In particular, the results show indications that T Tauri stars and HAe stars possibly accrete in similar manner while

HBe stars might have a different accretion mechanism. More work is needed, especially on how HBe stars accrete and their relation with massive stars. This section presents ideas for future extensions of this work.

5.2.1 High Angular Resolution - Hα Interferometry

Spectropolarimetry is a very powerful technique to reveal small spatial scale around HAeBe stars. It is shown in chapter 4 that the analysis of the polarisation line effect across Hα provides information about the line emitting region. The majority of HAe and T Tauri stars show an intrinsic line polarisation which is associated with the line originating from a compact source where the accretion occurs onto the star. The luminosity of the Hα line is found to be correlated with the accretion luminosity (Fairlamb *et al.* 2015). For the more massive HBe stars, a depolarisation line effect is more common. This is interpreted by the line emerging from an extended circumstellar disk. In addition, a few objects, mostly HBe stars, display a McLean line across the absorption component of Hα. Therefore, the spatial origin of Hα ranges from accretion spots to extended disks through stellar winds. The results also suggest that the interface between HBe and HAe ($\sim$ B9 to A1) is where the accretion mechanism changes. In this spectral range, distinguishing between intrinsic polarisation and depolarisation line effect becomes more difficult.

The Hα line originates from the very inner parts, a few au, of the circumstellar environment where most stellar activities take place. Therefore, high angular resolution Hα spectro-interferometry is extremely powerful to spatially resolve Hα line components. Through analysis of the observed visibility and phase of

the line and nearby stellar continuum, it can be determined whether the line is compact or extended. Essentially, the origin of the line is revealed, whether it is accretion region or extended region. Currently, Hα spectro-interferometry can be obtained with VEGA/CHARA spectro-interferometer. Rousselet-Perraut *et al.* (2010) performed Hα spectro-interferometry on the HAeBe star AB Aur, and found that the origin of the Hα line is disk wind. This is consistent with the polarisation line effect seen across the absorptive component of Hα (Vink *et al.* 2002).

5.2.2 Circumstellar Geometry - Line Profiles

Chapter 3 is dedicated to the observational studies of two optically visible and recently recognised massive young stellar objects PDS 27 and PDS 37. Their young nature is supported by the observed UV excess and high accretion rates which are often observed in young objects that are still accreting (Fairlamb *et al.* 2015). In addition, they have an active circumstellar environment evidenced by strong wind, high accretion rates, strong polarisation and a large IR excess. Both stars were also classified as young in the Red MSX Source (RMS) survey for MYSOs (Lumsden *et al.* 2013). They are massive $\sim$20 $M_{\odot}$ and hot $\sim$20000 K and their location on the H-R diagram indicate that they are evolving to become O-type stars. The near infrared interferometric results also show that both objects are extended and have possible companions. Despite the valuable information that was gathered about their circumstellar environment, I could not strongly confirm their nature nor map much of the extended nebula in our 1-dimensional spectra. As they are massive, young and have a dusty active circumstellar environment,

they are a very important test-bed to study the formation of the most massive stars. Specifically, the study of their circumstellar environment gives a wealth of information to better understand the process of massive star formation. Line profiles can also be used as a useful tool to probe the circumstellar geometry but their interpretation in 1-dimensional spectra can be challenging. To confirm our findings and have a better understanding on the nature of the stellar activity such as accretion and outflows, the objects need to be observed from different viewing angles and distances from the star.

This can be achieved with Integral Field Spectroscopy which is an ideal tool for exploring spatially extended objects and studying the complex process such revealing disk, accretion mass and outflows in the circumstellar environment. With this technique a spectrum can be produced for all parts of the extended objects simultaneously over a full 2-dimensional field of view. The circumstellar dust acts like a mirror by reflecting light from the central star. When the emission line photons are scattered by the circumstellar dust, we are able to see the star from different directions. The dust above the star views the disk face-on resulting in single peaked emission lines. However, the dust in the midplane views the disk edge-on, resulting in double peaked emission lines. Therefore, the variation of line profiles can be studied as a function of viewing angle. The technique has been successfully used by Davies *et al.* (2007) to study the geometry of mass-loss through investigating the reflected light from the dusty nebula around the evolved objects IRC+10420.

5.2.3 McLean Line Effect

As presented in this thesis, a number of HAeBe stars, mostly HBe stars, show a change in polarisation only across the absorption component of Hα line, commonly referred to as the McLean effect. The concept of this type of line effect is based on the fact that wind material, in case of aspherical geometry, blocks the unscattered light and scatters some of the photons into our line of sight. The non detection of this line effect across Hβ in some sources is explained by the fact the detection of the line effect strongly relies on the number of scattered photons into our line of sight. However, Kuhn *et al.* (2007) propose optical pumping model to explain the McLean effect, where the absorbing materials cause polarisation without scattering. The difference with the former scenario is that scattering in a flattened geometry is not responsible for the observed polarisation. There is a lack of explanation about the optical pumping model proposed by Kuhn *et al.* (2007) and it only expects a change in polarisation across the absorptive component of Hα line. However, a change in polarisation is detected across the absorption as well as the emission at the same time (e.g. HD 98922). In order to thoroughly investigate this a sophisticated model is necessary to reproduce the line profile and its line effect.

5.2.4 Extreme Polarisation Objects

A few objects display line effects across more lines than Hα alone, in particular R Mon shows the line effect across almost all the observed emission lines. It has a very strong continuum polarisation with values of order 12% and 8%, in the R band in 2012 and 2011 data respectively. The continuum polarisation

increased by 4% over timespan of only 4 months, while the continuum polarisation angle stayed the same in both epochs. However, the continuum polarisation angle shows a gradual decrease of $\sim 10^{\circ}$ from V to I band. In addition, R Mon also shows an extremely rare line effect up to 7% across Hα line. This magnitude of line effect has never been observed, the analysis of a large sample of HAeBe stars in chapter 4 shows that a typical line effect due to electron scattering is of order 2%. In addition, the results show that the angle of intrinsic polarisation varies, from $\sim 60^{\circ}$ to $\sim 130^{\circ}$ among the observed emission lines. In fact Hα and forbidden lines display a similar angle, which might suggests that the lines emerge in large and perhaps similar volumes, while other lines, emerging from smaller volumes and perhaps different geometries, show a different angle. All these complex polarisation behaviours could be due to clumpy structure within the circumstellar environment or different optical depths and geometries being responsible for the observed polarisations. To fully investigate this and understand the complex nature of the circumstellar environment of R Mon, multi epoch polarisation observations are needed at different wavelengths, to see how the polarisation, both intrinsic and continuum polarisation, behaviour is changing in strength and angle. This can then be compared with different analytical models to retrieve the circumstellar morphology of the star.

5.3 Final Remarks

The work in this thesis presents the spectropolarimetric study of a large sample of HAeBe stars. The observed line effects across Hα line suggests that HAeBe stars are surrounded by circumstellar disks. It appears that HAe and T Tauri stars

share similar polarisation properties while HBe stars behave differently than the former two. This might suggest that HAe stars form in the same manner as T Tauri stars via magnetospheric accretion while HBe stars could have a different accretion mechanism.

References

Ababakr, K.M., Fairlamb, J.R., Oudmaijer, R.D. & van den Ancker, M.E. (2015). Spectroscopy and linear spectropolarimetry of the early Herbig Be stars PDS 27 and PDS 37. MNRAS, **452**, 2566–2578. 34, 35, 56, 66, 106, 107, 108

Ababakr, K.M., Oudmaijer, R.D. & Vink, J.S. (2016). Linear spectropolarimetry across the optical spectrum of Herbig Ae/Be stars. MNRAS, **461**, 3089–3110. 146, 147, 161

Acke, B., van den Ancker, M.E. & Dullemond, C.P. (2005). [O I] 6300 Å emission in Herbig Ae/Be systems: Signature of Keplerian rotation. A&A, **436**, 209–230. 40

Akeson, R.L., Ciardi, D.R., van Belle, G.T. & Creech-Eakman, M.J. (2002). Constraints on Circumstellar Disk Parameters from Multiwavelength Observations: T Tauri and SU Aurigae. ApJ, **566**, 1124–1131. 161

Akeson, R.L., Ciardi, D. & van Belle, G.T. (2003). Infrared interferometric observations of T Tauri stars. In W.A. Traub, ed., *Interferometry for Optical Astronomy II*, vol. 4838 of *Society of Photo-Optical Instrumentation Engineers (SPIE) Conference Series*, 1037–1042. 161

Alecian, E., Wade, G.A., Catala, C., Grunhut, J.H., Landstreet, J.D., Bagnulo, S., Böhm, T., Folsom, C.P., Marsden, S. & Waite, I. (2013). A high-resolution spectropolarimetric survey of Herbig Ae/Be stars - I. Observations and measurements. MNRAS, **429**, 1001–1026. 162

Andre, P., Ward-Thompson, D. & Barsony, M. (1993). Submillimeter continuum observations of Rho Ophiuchi A - The candidate protostar VLA 1623 and prestellar clumps. ApJ, **406**, 122–141. 6

André, P., Men'shchikov, A., Bontemps, S., Könyves, V., Motte, F., Schneider, N., Didelon, P., Minier, V., Saraceno, P., Ward-Thompson, D., di Francesco, J., White, G., Molinari, S., Testi, L., Abergel, A., Griffin, M., Henning, T., Royer, P., Merín, B., Vavrek, R., Attard, M., Arzoumanian, D., Wilson, C.D., Ade, P., Aussel, H., Baluteau, J.P., Benedettini, M., Bernard, J.P., Blommaert, J.A.D.L., Cambrésy, L., Cox, P., di Giorgio, A., Hargrave, P., Hennemann, M., Huang, M., Kirk, J., Krause, O., Launhardt, R., Leeks, S., Le Pennec, J., Li, J.Z., Martin, P.G., Maury, A., Olofsson, G., Omont, A., Peretto, N., Pezzuto, S., Prusti, T., Roussel, H., Russeil, D., Sauvage, M., Sibthorpe, B., Sicilia-Aguilar, A., Spinoglio, L., Waelkens, C., Woodcraft, A. & Zavagno, A. (2010). From filamentary clouds to prestellar cores to the stellar IMF: Initial highlights from the Herschel Gould Belt Survey. A&A, **518**, L102. 4

Bailey, J. (1997). TSP – A Time Series/Polarimetry Package. *Starlink User Note*, **66**. 131

Bailey, J. & Hough, J.H. (1982). A Simultaneous Infrared / Optical Polarimeter. PASP, **94**, 618. 140

Beltrán, M.T. & de Wit, W.J. (2016). Accretion disks in luminous young stellar objects. AA Rev., **24**, 6. 32

Bergin, E.A. & Tafalla, M. (2007). Cold Dark Clouds: The Initial Conditions for Star Formation. ARA&A, **45**, 339–396. 2, 3

Beristain, G., Edwards, S. & Kwan, J. (2001). Helium Emission from Classical T Tauri Stars: Dual Origin in Magnetospheric Infall and Hot Wind. ApJ, **551**, 1037–1064. 105

Bernasconi, P.A. & Maeder, A. (1996). About the absence of a proper zero age main sequence for massive stars. A&A, **307**, 829–839. 107, 108

Bertout, C. (1989). T Tauri stars - Wild as dust. ARA&A, **27**, 351–395. 1

Blitz, L. (1993). Giant molecular clouds. In E.H. Levy & J.I. Lunine, eds., *Protostars and Planets III*, 125–161. 2

Blitz, L. & Williams, J.P. (1999). Molecular Clouds (a review). *ArXiv Astrophysics e-prints*. 3

Blondel, P.F.C. & Djie, H.R.E.T.A. (2006). Modeling of PMS Ae/Fe stars using UV spectra. A&A, **456**, 1045–1068. 162

Bonnell, I.A., Bate, M.R., Clarke, C.J. & Pringle, J.E. (1997). Accretion and the stellar mass spectrum in small clusters. MNRAS, **285**, 201–208. 10

Castelli, F. & Kurucz, R.L. (2004). New Grids of ATLAS9 Model Atmospheres. *ArXiv Astrophysics e-prints, astro-ph/0405087*. 90

Cauley, P.W. & Johns-Krull, C.M. (2015). Optical Mass Flow Diagnostics in Herbig Ae/Be Stars. ApJ, **810**, 5. 130

Chini, R., Hoffmeister, V.H., Nasseri, A., Stahl, O. & Zinnecker, H. (2012). A spectroscopic survey on the multiplicity of high-mass stars. MNRAS, **424**, 1925–1929. 123

Chlewicki, G., van der Zwet, G.P., van Ijzendoorn, L.J., Greenberg, J.M. & Alvarez, P.P. (1986). Shapes and correlations as observational discriminants for the origin of diffuse bands. ApJ, **305**, 455–466. 94

Clarke, D. & McLean, I.S. (1974). Observations of the linear polarization in the Hbeta emission feature of gamma Cas. MNRAS, **167**, 27P–30P. 26, 32, 60

Crowther, P.A., Caballero-Nieves, S.M., Bostroem, K.A., Maíz Apellániz, J., Schneider, F.R.N., Walborn, N.R., Angus, C.R., Brott, I., Bonanos, A., de Koter, A., de Mink, S.E., Evans, C.J., Gräfener, G., Herrero, A., Howarth, I.D., Langer, N., Lennon, D.J., Puls, J., Sana, H. & Vink, J.S. (2016). The R136 star cluster dissected with Hubble Space Telescope/STIS. I. Far-ultraviolet spectroscopic census and the origin of He II λ1640 in young star clusters. MNRAS, **458**, 624–659. 9

Davies, B., Oudmaijer, R.D. & Sahu, K.C. (2007). Integral-Field Spectroscopy of the Post-Red Supergiant IRC +10420: Evidence for an Axisymmetric Wind. ApJ, **671**, 2059–2067. 171

Davies, B., Lumsden, S.L., Hoare, M.G., Oudmaijer, R.D. & de Wit, W.J. (2010). The circumstellar disc, envelope and bipolar outflow of the massive young stellar object W33A. MNRAS, **402**, 1504–1515. 125

de Wit, W.J., Testi, L., Palla, F., Vanzi, L. & Zinnecker, H. (2004). The origin of massive O-type field stars. I. A search for clusters. A&A, **425**, 937–948. 10

de Wit, W.J., Testi, L., Palla, F. & Zinnecker, H. (2005). The origin of massive O-type field stars: II. Field O stars as runaways. A&A, **437**, 247–255. 10

del Toro Iniesta, J.C. (2007). *Introduction to Spectropolarimetry*. 16

Delbouille, L., Roland, G. & Neven, L. (1973). *Atlas photometrique du spectre solaire de λ 3000 a λ 10000. Institut d'Astrophysique, Universite de Liege, Liege*. 88

Doucet, C., Pantin, E., Lagage, P.O. & Dullemond, C.P. (2006). Mid-infrared imaging of the circumstellar dust around three Herbig Ae stars: HD 135344, CQ Tau, and HD 163296. A&A, **460**, 117–124. 161

Edwards, S., Fischer, W., Hillenbrand, L. & Kwan, J. (2006). Probing T Tauri Accretion and Outflow with 1 Micron Spectroscopy. ApJ, **646**, 319–341. 128

Eisner, J.A., Lane, B.F., Hillenbrand, L.A., Akeson, R.L. & Sargent, A.I. (2004). Resolved Inner Disks around Herbig Ae/Be Stars. ApJ, **613**, 1049–1071. 161

Fairlamb, J.R. (2015). *Ph.D. Thesis: A Spectroscopic Study Into Accretion In Herbig Ae/Be Stars*. Ph.D. thesis, University of Leeds, School of Physics and Astronomy. 106

Fairlamb, J.R., Oudmaijer, R.D., Mendigutía, I., Ilee, J.D. & van den Ancker, M.E. (2015). A spectroscopic survey of Herbig Ae/Be stars with X-shooter - I. Stellar parameters and accretion rates. MNRAS, **453**, 976–1001. 34, 35, 64, 87, 130, 141, 162, 169, 170

Fedele, D., van den Ancker, M.E., Acke, B., van der Plas, G., van Boekel, R., Wittkowski, M., Henning, T., Bouwman, J., Meeus, G. & Rafanelli, P. (2008). The structure of the protoplanetary disk surrounding three young intermediate mass stars. II. Spatially resolved dust and gas distribution. A&A, **491**, 809–820. 161

Finkenzeller, U. & Mundt, R. (1984). The Herbig Ae/Be stars associated with nebulosity. A&AS, **55**, 109–141. 10

Fischer, W., Kwan, J., Edwards, S. & Hillenbrand, L. (2008). Redshifted Absorption at He I λ10830 as a Probe of the Accretion Geometry of T Tauri Stars. ApJ, **687**, 1117–1144. 128

Fossati, L., Bagnulo, S., Mason, E. & Landi Degl'Innocenti, E. (2007). Standard Stars for Linear Polarization Observed with FORS1. In C. Sterken, ed., *The Future of Photometric, Spectrophotometric and Polarimetric Standardization*, vol. 364 of *Astronomical Society of the Pacific Conference Series*, 503. 38, 44

Fuente, A., Rodríguez-Franco, A., Testi, L., Natta, A., Bachiller, R. & Neri, R. (2003). First Evidence of Dusty Disks around Herbig Be Stars. ApJL, **598**, L39–L42. 161

Fukagawa, M., Tamura, M., Itoh, Y., Hayashi, S.S. & Oasa, Y. (2003). Near-Infrared Imaging of the Circumstellar Disk around Herbig Ae Star HD 150193A. ApJL, **590**, L49–L52. 161

Goldstein, D. (2003). *Polarized light*. 16

Grady, C., Fukagawa, M., Maruta, Y., Ohta, Y., Wisniewski, J., Hashimoto, J., Okamoto, Y., Momose *et al.* (2015). The outer disks of Herbig stars from the UV to NIR. Ap&SS, **355**, 253–266. 32

Grady, C.A., Hamaguchi, K., Schneider, G., Stecklum, B., Woodgate, B.E., McCleary, J.E., Williger, G.M., Sitko, M.L., Ménard, F., Henning, T., Brittain, S., Troutmann, M., Donehew, B., Hines, D., Wisniewski, J.P., Lynch, D.K., Russell, R.W., Rudy, R.J., Day, A.N., Shenoy, A., Wilner, D., Silverstone, M., Bouret, J.C., Meusinger, H., Clampin, M., Kim, S., Petre, R., Sahu, M., Endres, M. & Collins, K.A. (2010). Locating the Accretion Footprint on a Herbig Ae Star: MWC 480. ApJ, **719**, 1565–1581. 162

Grinin, V.P. (1994). Polarimetric activity of Herbig Ae/Be stars. In P.S. The, M.R. Perez & E.P.J. van den Heuvel, eds., *The Nature and Evolutionary Status of Herbig Ae/Be Stars*, vol. 62 of *Astronomical Society of the Pacific Conference Series*, 63. 47

Hamann, F. & Persson, S.E. (1992). Emission-Line Studies of Young Stars. II. The Herbig Ae/Be Stars. ApJS, **82**, 285. 11, 105

Harries, T.J. (1996). POLMAP – An interactive data analysis package for linear spectropolarimetry. *Starlink User Note*, **204**. 38, 132

Herbig, G.H. (1960). The Spectra of Be- and Ae-TYPE Stars Associated with Nebulosity. ApJS, **4**, 337. 10

Hillenbrand, L.A., Strom, S.E., Vrba, F.J. & Keene, J. (1992). Herbig Ae/Be stars - Intermediate-mass stars surrounded by massive circumstellar accretion disks. ApJ, **397**, 613–643. 11, 48, 146

Hubrig, S., Stelzer, B., Schöller, M., Grady, C., Schütz, O., Pogodin, M.A., Curé, M., Hamaguchi, K. & Yudin, R.V. (2009). Searching for a link between the magnetic nature and other observed properties of Herbig Ae/Be stars and stars with debris disks. A&A, **502**, 283–301. 162

Hubrig, S., Ilyin, I., Schöller, M. & Lo Curto, G. (2013). HARPS spectropolarimetry of Herbig Ae/Be stars. *Astronomische Nachrichten*, **334**, 1093. 162

Ignace, R. & Brimeyer, A. (2006). Models of forbidden line emission profiles from axisymmetric stellar winds. MNRAS, **371**, 343–355. 40

Ilee, J.D., Wheelwright, H.E., Oudmaijer, R.D., de Wit, W.J., Maud, L.T., Hoare, M.G., Lumsden, S.L., Moore, T.J.T.,

Urquhart, J.S. & Mottram, J.C. (2013). CO bandhead emission of massive young stellar objects: determining disc properties. MNRAS, **429**, 2960–2973. 86, 120

Ilee, J.D., Fairlamb, J., Oudmaijer, R.D., Mendigutía, I., van den Ancker, M.E., Kraus, S. & Wheelwright, H.E. (2014). Investigating the inner discs of Herbig Ae/Be stars with CO bandhead and Brγ emission. MNRAS, **445**, 3723–3736. 32

Isella, A. (2006). *Interferometric observations of pre-main sequence disks*. Ph.D. thesis, Universitá degli Studi di Milano, Facoltaà di Scienze Matematiche, Fisiche e Naturali. 8

Isella, A., Testi, L., Natta, A., Neri, R., Wilner, D. & Qi, C. (2007). Millimeter imaging of HD 163296: probing the disk structure and kinematics. A&A, **469**, 213–222. 161

Jain, S.K. & Bhatt, H.C. (1995). Study of variability of the polarization in Herbig Ae/Be stars. A&AS, **111**, 399. 47

Jenniskens, P. & Desert, F.X. (1994). A survey of diffuse interstellar bands (3800-8680 A). A&AS, **106**, 39–78. 94

Jolin, M.A., Bastien, P., Denni, F., Lafrenière, D., Doyon, R. & Voyer, P. (2010). Toward Understanding the Environment of R Monocerotis from High-Resolution Near-Infrared Polarimetric Observations. ApJ, **721**, 1748–1754. 67, 69, 70

Kitamura, Y., Momose, M., Yokogawa, S., Kawabe, R., Tamura, M. & Ida, S. (2002). Investigation of the Physical Properties of Protoplanetary Disks around T Tauri Stars by a 1 Arcsecond Imaging Survey: Evolution and Diversity of the Disks in Their Accretion Stage. ApJ, **581**, 357–380. 161

Kraus, S. (2015). The interferometric view of Herbig Ae/Be stars. Ap&SS, **357**, 97. 32

Kraus, S., Preibisch, T. & Ohnaka, K. (2008). Detection of an Inner Gaseous Component in a Herbig Be Star Accretion Disk: Near- and Mid-Infrared Spectrointerferometry and Radiative Transfer modeling of MWC 147. ApJ, **676**, 490–508. 161

Kuhn, J.R., Berdyugina, S.V., Fluri, D.M., Harrington, D.M. & Stenflo, J.O. (2007). A New Mechanism for Polarizing Light from Obscured Stars. ApJL, **668**, L63–L66. 33, 74, 76, 172

Kuhn, J.R., Geiss, B. & Harrington, D.M. (2011). Using Absorptive Linear Polarization Spectroscopy to Understand Imbedded Stars. In J.R. Kuhn, D.M. Harrington, H. Lin, S.V. Berdyugina, J. Trujillo-Bueno, S.L. Keil & T. Rimmele, eds., *Solar Polarization 6*, vol. 437 of *Astronomical Society of the Pacific Conference Series*, 245. 33, 74, 76

Kuiper, R., Klahr, H., Beuther, H. & Henning, T. (2010). Circumventing the Radiation Pressure Barrier in the Formation of Massive Stars via Disk Accretion. ApJ, **722**, 1556–1576. 9

Kurosawa, R., Romanova, M.M. & Harries, T.J. (2011). Multidimensional models of hydrogen and helium emission line profiles for classical T Tauri stars: method, tests and examples. MNRAS, **416**, 2623–2639. 105

Kurucz, R.L. (1993). *SYNTHE spectrum synthesis programs and line data*. 90

Kučerová, B., Korčáková, D., Polster, J., Wolf, M., Votruba, V., Kubát, J., Škoda, P., Šlechta, M. & Křížek, M. (2013). Time-dependent spectral-feature variations of stars displaying the B[e] phenomenon. II. MWC 342. A&A, **554**, A143. 122

Lada, C.J. (1987). Star formation - From OB associations to protostars. In M. Peimbert & J. Jugaku, eds., *Star Forming Regions*, vol. 115 of *IAU Symposium*, 1–17. 6

Lada, C.J., Depoy, D.L., Merrill, K.M. & Gatley, I. (1991). Infrared images of M17. ApJ, **374**, 533–539. 10

Larson, R.B. (1969). Numerical calculations of the dynamics of collapsing proto-star. MNRAS, **145**, 271. 5

Larson, R.B. (2003). The physics of star formation. *Reports on Progress in Physics*, **66**, 1651–1697. 3

Le Bouquin, J.B., Berger, J.P., Lazareff, B., Zins, G., Haguenauer, P., Jocou, L., Kern, P., Millan-Gabet, R., Traub, W., Absil, O., Augereau, J.C., Benisty, M., Blind, N., Bonfils, X., Bourget, P., Delboulbe, A., Feautrier, P., Germain, M., Gitton, P., Gillier, D., Kiekebusch, M., Kluska, J., Knudstrup, J., Labeye, P., Lizon,

J.L., Monin, J.L., Magnard, Y., Malbet, F., Maurel, D., Ménard, F., Micallef, M., Michaud, L., Montagnier, G., Morel, S., Moulin, T., Perraut, K., Popovic, D., Rabou, P., Rochat, S., Rojas, C., Roussel, F., Roux, A., Stadler, E., Stefl, S., Tatulli, E. & Ventura, N. (2011). PIONIER: a 4-telescope visitor instrument at VLTI. A&A, **535**, A67. 89

Lumsden, S.L., Hoare, M.G., Urquhart, J.S., Oudmaijer, R.D., Davies, B., Mottram, J.C., Cooper, H.D.B. & Moore, T.J.T. (2013). The Red MSX Source Survey: The Massive Young Stellar Population of Our Galaxy. ApJS, **208**, 11. 86, 170

Malbet, F., Lachaume, R., Berger, J.P., Colavita, M.M., di Folco, E., Eisner, J.A., Lane, B.F., Millan-Gabet, R., Ségransan, D. & Traub, W.A. (2005). New insights on the AU-scale circumstellar structure of FU Orionis. A&A, **437**, 627–636. 161

Malfait, K., Waelkens, C., Waters, L.B.F.M., Vandenbussche, B., Huygen, E. & de Graauw, M.S. (1998). The spectrum of the young star HD 100546 observed with the Infrared Space Observatory. A&A, **332**, L25–L28. 11

Mannings, V. & Sargent, A.I. (1997). A High-Resolution Study of Gas and Dust around Young Intermediate-Mass Stars: Evidence for Circumstellar Disks in Herbig Ae Systems. ApJ, **490**, 792–802. 161

Masunaga, H. & Inutsuka, S.i. (2000). A Radiation Hydrodynamic Model for Protostellar Collapse. II. The Second Collapse and the Birth of a Protostar. ApJ, **531**, 350–365. 5

Masunaga, H., Miyama, S.M. & Inutsuka, S.i. (1998). A Radiation Hydrodynamic Model for Protostellar Collapse. I. The First Collapse. ApJ, **495**, 346–369. 5

Mathieu, R.D., Adams, F.C., Fuller, G.A., Jensen, E.L.N., Koerner, D.W. & Sargent, A.I. (1995). Submillimeter Continuum Observations of the T Tauri Spectroscopic Binary GW Orionis. ApJ, **109**, 2655. 161

McLean, I.S. (1979). Interpretation of the intrinsic polarizations of early-type emission-line stars. MNRAS, **186**, 265–285. 33, 60

Modigliani, A., Goldoni, P., Royer, F., Haigron, R., Guglielmi, L., François, P., Horrobin, M., Bristow, P., Vernet, J., Moehler, S., Kerber, F., Ballester, P., Mason, E. & Christensen, L. (2010). The X-shooter pipeline. In *Society of Photo-Optical Instrumentation Engineers (SPIE) Conference Series*, vol. 7737 of *Society of Photo-Optical Instrumentation Engineers (SPIE) Conference Series*. 88

Monnier, J.D., Berger, J.P., Millan-Gabet, R., Traub, W.A., Schloerb, F.P., Pedretti, E., Benisty, M., Carleton, N.P., Haguenauer, P., Kern, P., Labeye, P., Lacasse, M.G., Malbet, F., Perraut, K., Pearlman, M. & Zhao, M. (2006). Few Skewed Disks Found in First Closure-Phase Survey of Herbig Ae/Be Stars. ApJ, **647**, 444–463. 161

Mottram, J.C., Vink, J.S., Oudmaijer, R.D. & Patel, M. (2007). On the difference between Herbig Ae and Herbig Be stars. MNRAS, **377**, 1363–1374. 33, 146, 147, 151, 153, 154, 155, 156, 161

Muzerolle, J., Calvet, N. & Hartmann, L. (1998). Magnetospheric Accretion Models for the Hydrogen Emission Lines of T Tauri Stars. ApJ, **492**, 743–753. 1, 31

Ochsendorf, B.B., Ellerbroek, L.E., Chini, R., Hartoog, O.E., Hoffmeister, V., Waters, L.B.F.M. & Kaper, L. (2011). First firm spectral classification of an early-B pre-main-sequence star: B275 in ¡ASTROBJ¿M 17¡/ASTROBJ¿. A&A, **536**, L1. 85

Okamoto, Y.K., Kataza, H., Honda, M., Fujiwara, H., Momose, M., Ohashi, N., Fujiyoshi, T., Sakon, I., Sako, S., Yamashita, T., Miyata, T. & Onaka, T. (2009). Direct Detection of a Flared Disk Around a Young Massive Star HD200775 and its 10 to 1000 AU Scale Properties. ApJ, **706**, 665–675. 161

Oudmaijer, R.D. (2007). Spectropolarimetry and the Study of Circumstellar Disks. In Hartquist T. W., Falle S. A. E. G., Pittard J. M., eds, Diffuse Matter From Star Forming Regions to Active Galaxies. Springer-Verlag, Berlin, p. 83 . 59, 66

Oudmaijer, R.D. & Drew, J.E. (1999). Hα spectropolarimetry of B[e] and Herbig Be stars. MNRAS, **305**, 166–180. 26, 32, 48, 86, 147, 151, 153, 154, 155, 156

Oudmaijer, R.D., Busfield, G. & Drew, J.E. (1997). Diffuse interstellar bands in the spectra of massive young stellar objects. MNRAS, **291**, 797. 94, 96

Oudmaijer, R.D., Proga, D., Drew, J.E. & de Winter, D. (1998). The evolved B[e] star HD 87643: observations and a radiation-driven disc wind model for B[e] stars. MNRAS, **300**, 170–182. 39

Oudmaijer, R.D., Palacios, J., Eiroa, C., Davies, J.K., de Winter, D. *et al.* (2001). EXPORT: Optical photometry and polarimetry of Vega-type and pre-main sequence stars. A&A, **379**, 564–578. 48, 146

Oudmaijer, R.D., van den Ancker, M.E., Baines, D., Caselli, P., Drew, J.E., Hoare, M.G., Lumsden, S.L., Montesinos, B., Sim, S., Vink, J.S., Wheelwright, H.E. & de Wit, W.J. (2011). X-shooting Herbig Ae/Be stars: Accretion probed by near-infrared He I emission. *Astronomische Nachrichten*, **332**, 238–241. 34, 64, 87, 128, 129

Patel, M., Oudmaijer, R.D., Vink, J.S., Mottram, J.C. & Davies, B. (2006). A polarimetric study of the B[e] star HD 45677. MNRAS, **373**, 1641–1647. 161

Poeckert, R. & Marlborough, J.M. (1976). Intrinsic linear polarization of Be stars as a function of V sini. ApJ, **206**, 182–195. 26, 32, 60

Quirrenbach, A., Buscher, D.F., Mozurkewich, D., Hummel, C.A. & Armstrong, J.T. (1994). Maximum-entropy maps of the Be shell star zeta Tauri from optical long-baseline interferometry. A&A, **283**, L13–L16. 26, 32

Reid, M.J., Menten, K.M., Brunthaler, A., Zheng, X.W., Moscadelli, L. & Xu, Y. (2009). Trigonometric Parallaxes of Massive Star-Forming Regions. I. S 252 G232.6+1.0. ApJ, **693**, 397–405. 102

Rodrigues, C.V., Sartori, M.J., Gregorio-Hetem, J. & Magalhães, A.M. (2009). The Alignment of the Polarization of Herbig Ae/Be Stars with the Interstellar Magnetic Field. ApJ, **698**, 2031–2035. 48, 86, 146

Rousselet-Perraut, K., Benisty, M., Mourard, D., Rajabi, S., Bacciotti, F., Bério, P., Bonneau, D., Chesneau, O., Clausse, J.M., Delaa, O., Marcotto, A., Roussel, A., Spang, A., Stee, P., Tallon-Bosc, I., McAlister, H., ten Brummelaar, T., Sturmann, J., Sturmann, L., Turner, N., Farrington, C. & Goldfinger, P.J. (2010). The Hα line forming region of AB Aurigae spatially resolved at sub-AU with the VEGA/CHARA spectro-interferometer. A&A, **516**, L1. 170

Salpeter, E.E. (1955). The Luminosity Function and Stellar Evolution. ApJ, **121**, 161. 9

Sana, H., de Mink, S.E., de Koter, A., Langer, N., Evans, C.J., Gieles, M., Gosset, E., Izzard, R.G., Le Bouquin, J.B. & Schneider, F.R.N. (2012). Binary Interaction Dominates the Evolution of Massive Stars. *Science*, **337**, 444. 123

Serkowski, K., Mathewson, D.S. & Ford, V.L. (1975). Wavelength dependence of interstellar polarization and ratio of total to selective extinction. ApJ, **196**, 261–290. 44

Shu, F.H. (1977). Self-similar collapse of isothermal spheres and star formation. ApJ, **214**, 488–497. 5

Shu, F.H., Adams, F.C. & Lizano, S. (1987). Star formation in molecular clouds - Observation and theory. ARA&A, **25**, 23–81. 3

Siess, L., Dufour, E. & Forestini, M. (2000). An internet server for pre-main sequence tracks of low- and intermediate-mass stars. A&A, **358**, 593–599. 107, 108

Suárez, O., García-Lario, P., Manchado, A., Manteiga, M., Ulla, A. & Pottasch, S.R. (2006). A spectroscopic atlas of post-AGB stars and planetary nebulae selected from the IRAS point source catalogue. A&A, **458**, 173–180. 86

Testi, L., Palla, F. & Natta, A. (1999). The onset of cluster formation around Herbig Ae/Be stars. A&A, **342**, 515–523. 11

The, P.S., de Winter, D. & Perez, M.R. (1994). A new catalogue of members and candidate members of the Herbig Ae/Be (HAEBE) stellar group. A&AS, **104**, 315–339. 10, 34, 85, 130, 141, 151

Tinbergen, J. (1996). *Astronomical Polarimetry*. 16

Tody, D. (1993). IRAF in the Nineties. In R.J. Hanisch, R.J.V. Brissenden & J. Barnes, eds., *Astronomical Data Analysis Software and Systems II*, vol. 52 of *Astronomical Society of the Pacific Conference Series*, 173. 38, 131

Trammell, S.R., Dinerstein, H.L. & Goodrich, R.W. (1994). Evidence for the early onset of aspherical structure in the planetary nebula formation process: Spectropolarimetry of post-AGB stars. ApJ, **108**, 984–997. 71

Urquhart, J.S., Busfield, A.L., Hoare, M.G., Lumsden, S.L., Oudmaijer, R.D., Moore, T.J.T., Gibb, A.G., Purcell, C.R., Burton, M.G. & Marechal, L.J.L. (2007). The RMS survey. ^{13}CO observations of candidate massive YSOs in the southern Galactic plane. A&A, **474**, 891–901. 102

Urquhart, J.S., Morgan, L.K., Figura, C.C., Moore, T.J.T., Lumsden, S.L., Hoare, M.G., Oudmaijer, R.D., Mottram, J.C., Davies, B. & Dunham, M.K. (2011). The Red MSX Source survey: ammonia and water maser analysis of massive star-forming regions. MNRAS, **418**, 1689–1706. 103

Vernet, J., Dekker, H., D'Odorico, S., Kaper *et al.* (2011). X-shooter, the new wide band intermediate resolution spectrograph at the ESO Very Large Telescope. A&A, **536**, A105. 87

Vieira, R.G., Gregorio-Hetem, J., Hetem, A., Stasińska, G. & Szczerba, R. (2011). Distinguishing post-AGB impostors in a sample of pre-main sequence stars. A&A, **526**, A24. 86, 93

Vieira, S.L.A., Corradi, W.J.B., Alencar, S.H.P., Mendes, L.T.S., Torres, C.A.O., Quast, G.R., Guimarães, M.M. & da Silva, L. (2003). Investigation of 131 Herbig Ae/Be Candidate Stars. ApJ, **126**, 2971–2987. 34, 35, 86, 103, 104, 130, 151

Vink, J.S. (2015). Linear line spectropolarimetry of Herbig Ae/Be stars. Ap&SS, **357**, 98. 33

Vink, J.S., Drew, J.E., Harries, T.J. & Oudmaijer, R.D. (2002). Probing the circumstellar structure of Herbig Ae/Be stars. MNRAS, **337**, 356–368. 23, 26, 27, 33, 60, 86, 146, 147, 151, 153, 154, 155, 156, 157, 162, 170

Vink, J.S., Drew, J.E., Harries, T.J., Oudmaijer, R.D. & Unruh, Y.C. (2003). Resolved polarization changes across Hα in the classical T Tauri star RY Tauri. A&A, **406**, 703–707. 60

Vink, J.S., Drew, J.E., Harries, T.J., Oudmaijer, R.D. & Unruh, Y. (2005a). Probing the circumstellar structures of T Tauri stars and their relationship to those of Herbig stars. MNRAS, **359**, 1049–1064. 11, 24, 27, 33, 48, 60, 86, 127, 128, 146, 147, 151, 153, 154, 155, 156, 157, 160, 161

Vink, J.S., Harries, T.J. & Drew, J.E. (2005b). Polarimetric line profiles for scattering off rotating disks. A&A, **430**, 213–222. 24, 61, 127

Vrba, F.J., Schmidt, G.D. & Hintzen, P.M. (1979). Observations and evaluation of the polarization in Herbig Ae/Be stars. ApJ, **227**, 185–196. 48, 146

Vural, J., Kraus, S., Kreplin, A., Weigelt, G., Fossat, E., Massi, F., Perraut, K. & Vakili, F. (2014). Study of the sub-AU disk of the Herbig B[e] star HD 85567 with near-infrared interferometry. A&A, **569**, A25. 161

Wade, G.A., Drouin, D., Bagnulo, S., Landstreet, J.D., Mason, E., Silvester, J., Alecian, E., Böhm, T., Bouret, J.C., Catala, C. &

Donati, J.F. (2005). Discovery of the pre-main sequence progenitors of the magnetic Ap/Bp stars? A&A, **442**, L31–L34. 162

Wade, G.A., Bagnulo, S., Drouin, D., Landstreet, J.D. & Monin, D. (2007). A search for strong, ordered magnetic fields in Herbig Ae/Be stars. MNRAS, **376**, 1145–1161. 162

Waters, L.B.F.M. & Waelkens, C. (1998). Herbig Ae/Be Stars. ARA&A, **36**, 233–266. 10

Wheelwright, H.E., Vink, J.S., Oudmaijer, R.D. & Drew, J.E. (2011a). On the alignment between the circumstellar disks and orbital planes of Herbig Ae/Be binary systems. A&A, **532**, A28. 48, 50

Wheelwright, H.E., Vink, J.S., Oudmaijer, R.D. & Drew, J.E. (2011b). On the alignment between the circumstellar disks and orbital planes of Herbig Ae/Be binary systems. A&A, **532**, A28. 121, 147, 151, 153, 154, 155, 156, 160, 161

Wheelwright, H.E., Bjorkman, J.E., Oudmaijer, R.D., Carciofi, A.C., Bjorkman, K.S. & Porter, J.M. (2012). Probing the properties of Be star discs with spectroastrometry and NLTE radiative transfer modelling: β CMi. MNRAS, **423**, L11–L15. 32

Whittet, D.C.B., Martin, P.G., Hough, J.H., Rouse, M.F., Bailey, J.A. & Axon, D.J. (1992). Systematic variations in the wavelength dependence of interstellar linear polarization. ApJ, **386**, 562–577. 46

Williams, J.P. & McKee, C.F. (1997). The Galactic Distribution of OB Associations in Molecular Clouds. ApJ, **476**, 166–183. 2

Williams, J.P., Blitz, L. & McKee, C.F. (2000). The Structure and Evolution of Molecular Clouds: from Clumps to Cores to the IMF. *Protostars and Planets IV*, 97. 3

Yorke, H.W. & Sonnhalter, C. (2002). On the Formation of Massive Stars. ApJ, **569**, 846–862. 9

Yudin, R.V. & Evans, A. (1998). Polarimetry of southern peculiar early-type stars. A&AS, **131**, 401–429. 48, 146

Zickgraf, F.J. & Schulte-Ladbeck, R.E. (1989). Polarization characteristics of galactic B(e) stars. A&A, **214**, 274–284. 146

Zinnecker, H. & Yorke, H.W. (2007). Toward Understanding Massive Star Formation. ARA&A, **45**, 481–563. 1